TECHNISCHE UNIVERSITÄT MÜNCHEN

Max-Planck-Institut für Biochemie
Abteilung für Molekulare Strukturbiologie

Structure of Human Tripeptidyl Peptidase II determined by a Hybrid Approach

Anne-Marie Schönegge

Vollständiger Abdruck der von der Fakultät für Chemie der Technischen Universität München zur Erlangung des akademischen Grades eines Doktors der Naturwissenschaften genehmigten Dissertation.

Vorsitzender: Univ.-Prof. Dr. J. Buchner

Prüfer der Dissertation:

1. Hon.-Prof. Dr. W. Baumeister
2. Univ.-Prof. Dr. S. Weinkauf

Die Dissertation wurde am 12.01.2012 bei der Technischen Universität München eingereicht und durch die Fakultät für Chemie am 28.03.2012 angenommen.

Zusammenfassung

Tripeptidyl peptidase II (TPPII) ist eine Serinprotease der Subtilisin-Familie. Sie bildet den größten eukaryotischen Proteasekomplex, und seine Aktivität steigt während der Assemblierung. Es wurde postuliert, dass während dieser Aktivierung ein Segment von ‚Loop L2‘ aus der Substratbindestelle herausbewegt wird und damit das Serin des aktiven Zentrums in eine katalytisch-aktive Konformation gebracht wird. TPPII spielt eine bedeutende Rolle in verschiedenen physiologischen Prozessen, unter anderem beim zytosolischen Proteinabbau, bei der Antigen-Prozessierung, bei der Kontrolle des Sättigungsgefühls, bei der Fettspeicherung, bei Apoptose, beim Zellwachstum, und bei der Reparatur von DNA-Schäden. Zudem ist TPPII an einigen Krankheiten, wie beispielsweise Muskelschwund, Fettleibigkeit und Krebs, beteiligt. Jedoch ist bis jetzt noch nicht bekannt, welche Rolle TPPII in diesen Prozessen spielt.

In der vorliegenden Arbeit wurde die Struktur von humanem TPPII (*Hs*TPPII) mittels Elektronenmikroskopie und Einzelpartikelanalyse zu Subnanometer-Auflösung bestimmt. TPPII besteht aus zwei Strängen, die eine spindelförmige Struktur bilden, welche ein komplexes System innerer Höhlen umschließt. *Hs*TPPII-Partikel zeigen einen gewissen Polymorphismus; es treten Komplexe mit neun und mit acht Dimeren pro Strang auf. Um die Architektur und Funktionsweise von TPPII genauer zu verstehen, wurde ein pseudo-atomares Modell der Spindel durch molekular-dynamisches flexibles Einpassen eines Homologie-Modells der *Hs*TPPII-Dimere erstellt. Die Analyse dieses Hybrid-Modells zeigte Konformationsunterschiede zwischen den Dimeren, die innerhalb eines Stranges liegen, und den Dimeren, die am Ende eines Stranges liegen. Die dabei gefundenen Positionsveränderungen einiger α-Helices könnten einerseits die Feinjustierung der Konformation des Eingangsbereiches zum Kavitätensystem einleiten, und andererseits als Sensor des Assemblierungszustandes der Dimere dienen und damit deren Aktivierung auslösen.

Die systematische Mutationsanalyse von ‚Loop L2‘ (ein Segment an dessen C-terminalem Ende das Serin des aktiven Zentrums liegt), ‚Loop L1‘ (ein Segment in der Nähe von ‚Loop L2‘) und von deren postulierte Interaktionsbereiche wies die Bedeutung dieser Bereiche für die Assemblierung und Aktivierung von TPPII nach. Die Ergebnisse zeigten, dass ‚Loop L1‘ eine größere Rolle bei der Assemblierung des Komplexes spielt, während ‚Loop L2‘ von größerer Bedeutung für die Aktivierung von TPPII ist.

Diese Arbeit unterstreicht die Bedeutung der Dimer-Dimer Grenzfläche für Struktur und Funktionsweise von TPPII: Kontakte zwischen den Dimeren bestimmen die Morphologie des Spindelkomplexes und lösen vermutlich Konformationsänderungen im katalytischen Zentrum und im Eingangsbereich des Kavitätensystems aus. Die hier präsentierte Hybridstruktur von *Hs*TPPII-Spindeln könnte als Basis für Untersuchungen der zellulären Funktion von TPPII dienen.

Summary

Tripeptidyl peptidase II (TPPII) is a serine protease of the subtilisin family. It forms the largest known eukaryotic protease complex, the activity of which increases upon assembly. It has been proposed that during TPPII activation a segment of loop L2 is removed from the active-site cleft and concomitantly the active-site serine is positioned in a catalytically active conformation. TPPII plays a critical role in various biological processes such as cytosolic protein degradation, antigen processing, satiety control, fat storage, apoptosis, cell replication, or DNA damage repair, and it is involved in diseases like muscle wasting, obesity, and in cancer. However, the exact function of TPPII in these processes awaits further clarification.

In the present study, the structure of human TPPII (*Hs*TPPII) has been determined to subnanometer resolution by cryo electron microscopy and single-particle analysis. TPPII is built of two strands forming a spindle-shaped structure harboring a complex system of inner cavities. *Hs*TPPII particles exhibit some polymorphism resulting in complexes consisting of nine or of eight dimers per strand. To obtain deeper insights into the architecture and function of TPPII, a pseudo-atomic model of the spindle was created by using a comparative model of *Hs*TPPII dimers and molecular dynamics flexible fitting. The analysis of the resulting hybrid structure pointed at conformational differences between in-strand and end-of-strand dimers. The change in position detected for several α-helices might on the one hand induce conformational fine-tuning of the entrance region to the cavity system and on the other hand serves as sensor for the assembly state of dimers and trigger their activation.

A systematic mutational analysis of loop L2 (which is connected to the active-site serine), loop L1 (which is proximal to loop L2), and their proposed interaction sites demonstrated the importance of these regions for the assembly and activation of the TPPII complex. The data suggest that loop L1 plays a major role in the assembly of the complex, whereas loop L2 is of greater significance for the activation of TPPII.

The work presented here highlights the importance of the dimer-dimer interface for structure and functionality of TPPII: Contacts between dimers determine the morphology of the spindle complex and supposedly trigger conformational changes involving the catalytic center and the entrance to the cavity system. The hybrid structure of *Hs*TPPII spindles could be the basis for studies that shed light on the cellular functions of TPPII.

Table of Content

Figure Index

Table Index

1 Introduction

1.1 Peptidases

Peptidases catalyze the hydrolysis of peptide bonds. Exopeptidases release a defined number of amino acids from the N- or C-terminus, whereas endopeptidases cleave proteins and peptides internally. Depending on whether an aspartate-, cysteine, serine-, threonine-residue or a metallo-group takes part in the catalysis, peptidases are classified into different groups. In the case of serine-, cysteine- and threonine-peptidases, the nucleophile is part of an amino acid. In the other cases an activated water molecule performs the nucleophilic attack (Barrett et al., 2004).

Serine peptidases use a charge-relay system consisting of two or three amino acids to create a nucleophile attacking the scissile bond. The two main clans of serine peptidases (trypsin (EC 3.4.21.4) clan and subtilisin (EC 3.4.21.62) clan) use the catalytic triad Asp-His-Ser (see Figure 1). The serine performs a nucleophilic attack on the carbonyl carbon of the scissile bond, which leads to the formation of a tetrahedral intermediate (step 1). Cleavage of the scissile bond results in the acyl-enzyme intermediate and the formation of the new N-terminus (step 2). The N-terminus is replaced by a water molecule (step 3), which subsequently attacks the carbonyl carbon of the substrate (step 4). The tetrahedral intermediate decays to create the new C-terminus while regenerating the active-site of the enzyme (step 5). In this mechanism the histidine assists by accepting and donating protons and the aspartate stabilizes and orients the histidine (Hedstrom, 2002). The proper geometry of the catalytic triad is crucial for the reaction cycle.

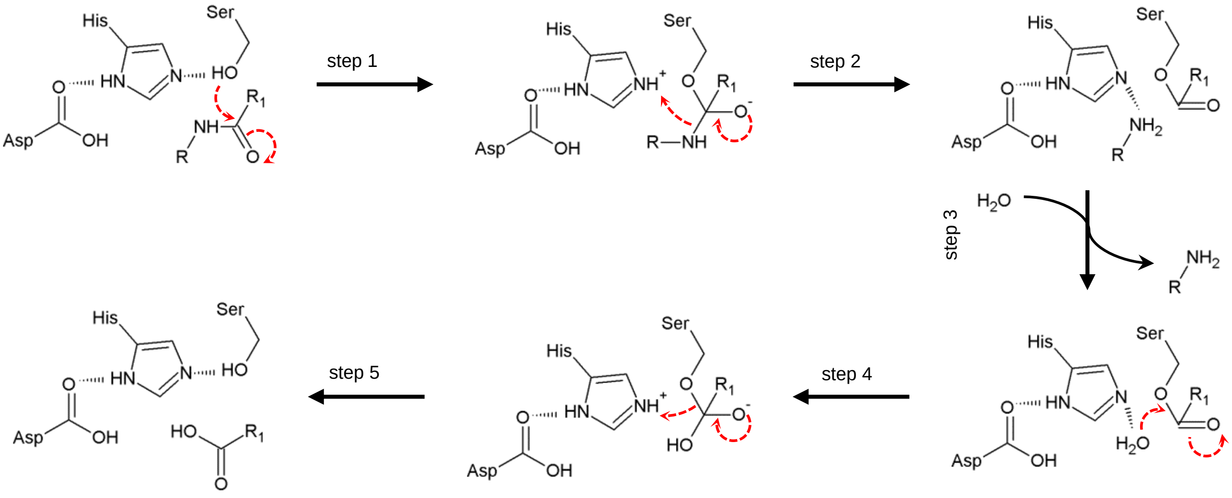

Figure 1: Catalytic mechanism of serine peptidases.

The subtilisin clan of serine peptidases is based on an extracellular endopeptidase from *Bacillus subtilis* – called subtilisin. Subtilisin is synthesized as a zymogen that remains inactive in the cytoplasm. After translocation of the zymogen across a membrane an autocatalytic cleavage of its pro-peptide occurs, which leads to a subsequent rearrangement of the N-terminal region stabilizing the enzyme. A second cleavage in the pro-peptide is followed by its total degradation and the activation of subtilisin (see Figure 2; Lazure, 2002). Over the years it has emerged that a large number of homologous proteins (subtilases) exist, which have diverse functions and are expressed in many organisms (Siezen et al., 1991). For a long time it was thought that subtilases are restricted to microorganisms, but more recently several eukaryotic members of the family have become known (Barrett et al., 2004; Siezen and Leunissen, 1997). One eukaryotic member is Tripeptidyl Peptidase II (TPPII; EC 3.4.14.10; Balow et al., 1986; Tomkinson et al., 1987). Among the subtilases TPPII is quite unique. It is a member of the highly diverse pyrolysin subfamily characterized by large insertions and/or long C-terminal extensions (Siezen and Leunissen, 1997).

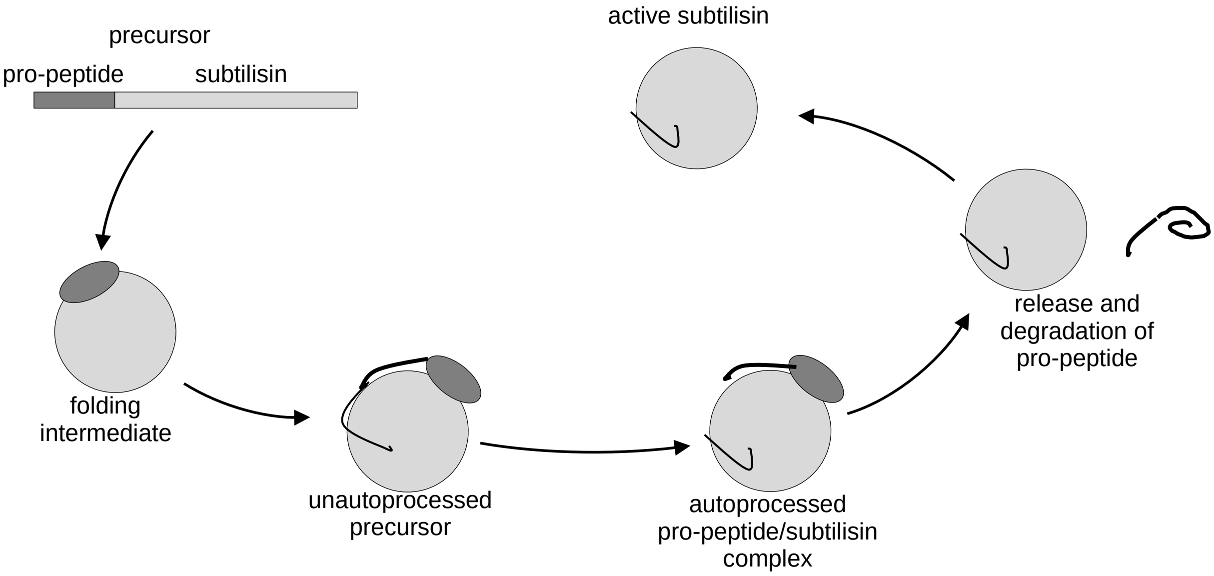

Figure 2: Activation Mechanism of Subtilisin.

Subtilisin is synthesized as zymogen with a pro-sequence. During activation the pro-peptide is autocatalytically cleaved and subsequently released.

1.2 Principle of Self-compartmentalization

Temporal and spatial control of cellular proteolysis is vital for every cell. Temporal control can be achieved by expressing peptidases as inactive zymogens and tightly controlling their activation or by regulating the interaction of peptidases with inhibitory proteins. Spatial control can occur in two ways: either the active enzyme is segregated in special compartments, e.g. lysosomes, or the enzyme is localized in the cytosol but its active-sites are sequestered. The principle of active-site sequestration within a complex is called self-compartmentalization and has evolved several times independently (Baumeister et al., 1998; Lupas et al., 1997).

The prime example for self-compartmentalization is the 26S proteasome. This 2.5 MDa complex is composed of the 20S core particle and one or two regulatory 19S particles. The 19S particles consist of 18 different subunits and they are responsible for the recognition, deubiquitination and unfolding of substrates. Moreover, their interactions with the α-subunits of the core complex regulate the entry to the proteolytic chamber (Glickman and Ciechanover, 2002; Glickman et al., 1998; Yu et al., 2010). The 20S particle is composed of four stacked heptameric rings. Two catalytic active β-rings enclose the catalytic chamber and are sandwiched by two α-rings. At the α-β-interfaces two antechambers reside (see Figure 3A; Baumeister et al., 1998; Lupas et al., 1997; Walz et al., 1998; Yoshimura et al., 1993). The assembly of the proteasome triggers its activation: After assembly of two half-proteasomes an inhibitory pro-peptide is autocatalytically removed from the β-subunit (Chen and Hochstrasser, 1996; Witt et al., 2006).

A similar architecture is found for the bacterial protease ClpP. ClpP forms a barrel-shaped complex of two heptameric rings that enclose the catalytic chamber, which can be assessed through the central pores of the rings (see Figure 3B; Kessel et al., 1995; Wang et al., 1997). Entry to the catalytic chamber is regulated via the ATPase ClpA, which is also responsible for substrate unfolding (Kessel et al., 1995; Yao and Cohen, 2002). Despite the structural similarity between ClpAP and the 26S proteasome, they are neither related at the level of sequence nor structure (Baumeister et al., 1998).

Several archaeal proteases are self-compartmentalized. Examples are the peptidases tricorn (TRI) and tetrahedral protease (TET), which degrade peptides downstream of the proteasome (Borissenko and Groll, 2005). Both have been observed in different high oligomeric states (Schoehn et al., 2006; Walz et al., 1997). TRI from *Thermoplasma acidophilum* is a hexamer consisting of three dimers when expressed in *E. coli*. In *Thermoplasma*, TRI forms a higher oligomer of twenty hexamers assembled into an icosahedral capsid (see Figure 3C; Brandstetter et al., 2001; Tamura et al., 1996; Walz et al., 1997). TET from *Pyrococcus horikoshii* exists either as a tetrahedron built of twelve subunits or as an octahedron consisting of 24 subunits. Both complexes enclose a catalytic chamber the entry of which is provided by several channels (see Figure 3D; Borissenko and Groll, 2005; Schoehn et al., 2006). For these archaeal proteases a relationship between assembly and activity has been described: in the case of TRI, D936 of one subunit reaches into the P1 pocket of the next subunit, and there it acts as a switch between P1 specificity for basic and for hydrophobic residues (Brandstetter et al., 2002). Disassembled dimers of TET cleave fluorogenic substrates with approximately 40-50% lower activity than its oligomeric form (Borissenko and Groll, 2005).

In Eukarya, the function of TRI and TET is presumably performed by TPPII. TPPII exhibits a unique architecture that leads to self-compartmentalization. It forms a spindle-shaped complex consisting of two twisted strands. Each strand harbors a cavity system consisting of a longitudinal channel from which, at every dimer-dimer interface, catalytic chambers branch off. This network of channels and chambers leads to the sequestration of multiple active-sites along a strand (Chuang et al., 2010; Rockel et al., 2005).

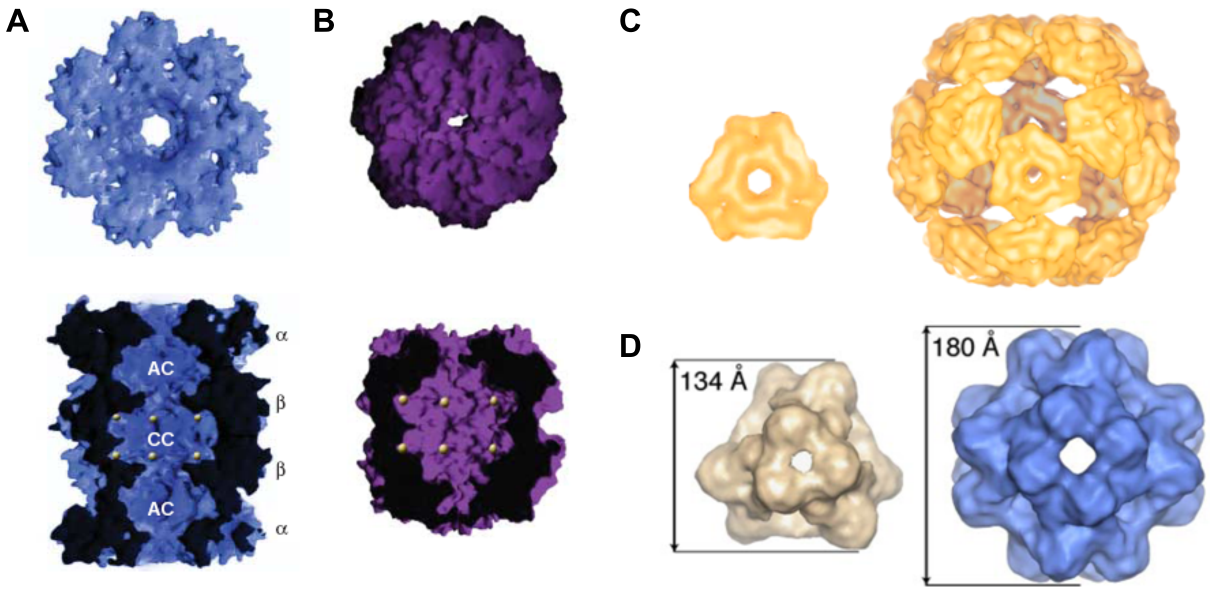

Figure 3: Structures of self-compartmentalizing proteases.

Structures of **(A)** the 20S proteasome from T. acidophilum. **(B)** the ClpP protease from *E. coli*, **(C)** the TRI protease from T. acidophilum, **(D)** and the TET protease from P. horikoshii are shown (adapted from Pickart and Cohen, 2004 (A+B); Baumeister et al., 1998 (C); Schoehn et al., 2006 (D)).

1.3 Tripeptidyl Peptidase II

1.3.1 Biological Functions

TPPII has been described as a ‘multipurpose peptidase’, whose biological role still remains enigmatic (Preta et al., 2010b; Tomkinson and Lindas, 2005). A schematic overview of several functions proposed for TPPII is given in Figure 4.

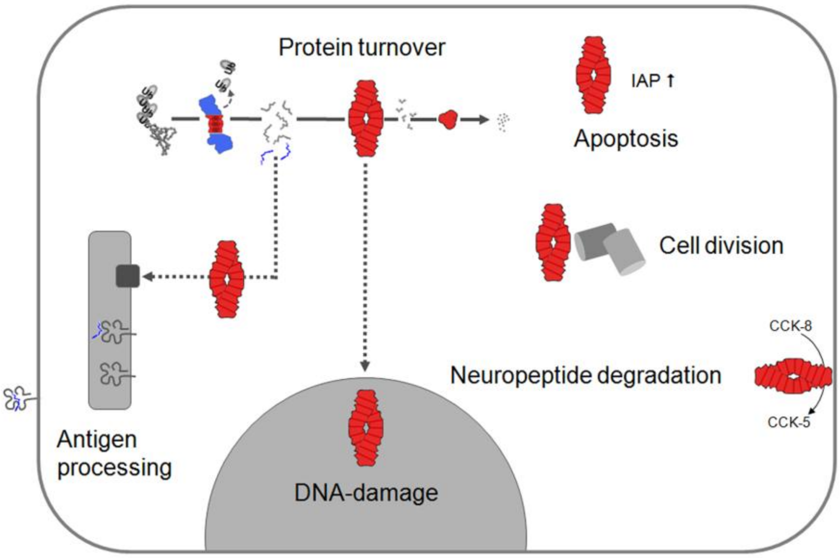

Figure 4: Schematic overview of TPPII functions.

1.3.1.1 Protein Turnover

Strict regulation of protein homeostasis is essential for every cell. In addition to a regulated protein synthesis, controlled protein degradation is also necessary and a variety of diseases are related to dysregulation of proteolysis e.g. Alzheimer disease, Parkinson disease, Huntington disease, cancer (Chen et al., 2011; Hegde and Upadhya, 2011). The main pathway for cytosolic protein degradation in eukaryotic cells is the ubiquitin-proteasome pathway, which consists of several steps: i) target proteins are labeled for degradation by polyubiquitination. For this process three enzymes are needed: E1, a ubiquitin activating enzyme, E2, a ubiquitin conjugating enzyme, and E3, a ubiquitin ligase (Glickman and Ciechanover, 2002). ii) The polyubiquitin chain is recognized by the 19S cap, where the ubiquitin is recycled by deubiquitination enzymes and the target protein is unfolded in an ATP-dependent manner. iii) Subsequently the target is translocated into the 20S core particle, where its breakdown takes place (Pickart and Cohen, 2004; Yao and Cohen, 2002; Zwickl et al., 2000). The peptides released by the proteasome vary between 3 and 23 amino acids in length and are on average 7 to 9 amino acids long (Kisselev et al., 1999; Nussbaum et al., 1998). Further degradation of the peptides is performed by Leucin-Aminopeptidase (LAP; Beninga et al., 1998), Thimet-Oligopeptidase (TOP; York et al., 2003), Bleomycin-Hydrolase (BH; Stoltze et al., 2000) and Tripeptidyl Peptidase II (TPPII; Tomkinson, 1999). However, the processing of peptides longer than 15 amino acids appears to depend entirely on TPPII (Reits et al., 2004). Subsequently, the resulting peptides are broken up into amino acids by aminopeptidases e.g. dipeptidylpeptidases (Baumeister et al., 1998; Tomkinson, 1999).

Inhibition of the proteasome is lethal for most cells. Since elevated levels of TPPII have been found in cells adapted to proteasome inhibition (Duensing et al., 2010; Geier et al., 1999; Glas et al., 1998; Wang et al., 2000), it was proposed that TPPII could take over some tasks of the proteasome (Geier et al., 1999; Wang et al., 2000). However, most inhibitors of the proteasome do not inhibit the proteasome completely, but merely reduce its activity (Gavioli et al., 2001; Princiotta et al., 2001; Wang et al., 2000). In addition, cells are thought to exhibit feedback loops to cope with reduced proteasome activity. These feedback loops include the upregulation of the expression and assembly of proteasome subunits (Meiners et al., 2003; Mitsiades et al., 2002). Moreover, the accumulation of polyubiquitinated proteins caused by proteasome inhibition might be avoided by residual proteasome activity and/or other proteases. For instance, an AAF-CMK-sensitive activity, which could not be attributed to TPPII, was demonstrated to take part in the removal of polyubiquitinated proteins (Villasevil et al., 2010). Hence, it is under debate, whether high levels of TPPII suffice to ensure cell survival in the absence of proteasome activity (Princiotta et al., 2001; Villasevil et al., 2010).

1.3.1.2 Antigen Processing

In addition to perceiving and clearing pathogen invasions, the immune system keeps the body under surveillance for malignant, damaged, infected, or dead cells. To protect an organism, the immune system needs to distinguish ‘self’ from ‘non-self’. In vertebrates, the constant display of intracellular epitopes on the cell surface by the major histocompatibility complex (MHC) class I is the basis for the recognition of ‘self’ and ‘non-self’. Detection of a “non-self” epitope by CD8$^+$ cytotoxic T-cell results in the induction of apoptosis in the respective cell.

In general, MHC class I epitopes are produced during regular cytosolic protein degradation. Approximately 10% of the peptides produced by the proteasome are 8 to 10 amino acids long and can be loaded on the MHC class I directly. An additional 10% of the peptides are too long for direct loading (Kisselev et al., 1999; van Endert, 2008). Most of these peptides already possess the correct C-terminus, and N-terminal trimming adjusts their length for

MHC class I binding. This N-terminal trimming either occurs in the endoplasmic reticulum (ER) by the ER aminopeptidase associated with antigen processing (ERAP; Saric et al., 2002; Shastri et al., 2005; York et al., 2002) or in the cytosol by various aminopeptidases. Several cytosolic aminopeptidases have been reported to be involved in antigen processing, such as Leucin-Aminopeptidase (LAP; Beninga et al., 1998), Bleomycin-Hydrolase (BH; Stoltze et al., 2000), Puromycin-sensitive Aminopeptidase (PSA; Stoltze et al., 2000; York et al., 2003), Thimet-Oligipeptidase (TOP; Saric et al., 2002; York et al., 2003) and also TPPII (Geier et al., 1999; Reits et al., 2004; Seifert et al., 2003).

However, the role of TPPII in antigen processing is discussed controversially. Despite several reports about the ability of TPPII to generate epitopes ($RU1_{34-42}$-epitop, Levy et al., 2002; SIINFEKL, York et al., 2006; gp100, Burri et al., 2002), the majority of reports suggest a destructive effect of TPPII on epitopes (see van Endert, 2011 for review).

1.3.1.3 Cellular Pathways

Functional studies of mammalian TPPII hint at roles of the peptidase in a variety of metabolic, cancer-related and pathology-related pathways. Over-expression of TPPII is thought to have several consequences for cells: i) increased proliferation rate and enhanced growth under starvation conditions (Hong et al., 2003; Stavropoulou et al., 2006); ii) chromosomal instability due to multipolar mitosis with spindle abnormalities (Stavropoulou et al., 2006; Stavropoulou et al., 2005); iii) evasion of apoptosis as a result of overexpression and slow degradation of anti-apoptotic proteins (c-IAP1, c-IAP2, Bl-2, Bcl-XL, and XIAP; Hong et al., 2003; Stavropoulou et al., 2006). In combination, these effects allude to a possible association of TPPII to cancer promotion. An involvement of TPPII in tumor progression has already been proposed in the case of Burkitt's lymphoma (BL). These B-cell tumors are characterized by the overexpression of *c-myc*, reduced adherence of the cells and low amounts of B-cell markers and MHC class I molecules on the cell surface (Klein, 1983; Masucci, 2004; Rowe et al., 1987). Protein degradation in these cells seems to be independent of the proteasome and is sustained by the overexpression of both deubiquitinating enzymes and TPPII (Gavioli et al., 2001). Consequently, it has been suggested that a combination of γ-irradiation and selective inhibition of TPPII might be a promising tumor therapy for Burkitt's lymphoma (Duensing et al., 2010).

A differential, tissue-specific regulation of cytosolic protein degradation has also been reported to occur during sepsis – a systemic inflammatory state that is associated with muscle wasting (Hasselgren and Fischer, 2001; Tiao et al., 1994): an increase of TPPII expression level was observed in white muscle, whereas in liver a decrease of TPPII expression level was found. Thus, the increased protein degradation in white muscle cells is possibly linked to TPPII upregulation (Wray et al., 2002).

TPPII activity has also been shown to modulate the infectivity of pathogens. Cytosolic protein degradation by the ubiquitin-proteasome pathway is supposedly essential for the intracellular replication of coxsackiviruses, which can cause a variety of illnesses ranging from mild gastrointestinal distress to myocarditis. Inhibition of the proteasome leads to a severe decrease in viral infectivity (Gao et al., 2008). Infectivity is further reduced when a combination of proteasome- and TPPII-inhibitors is applied (Zhang et al., 2011). Apparently, the virus not only employs the proteasome for its replication but also requires downstream components of the proteasome-ubiquitin pathway.

TPPII might also influence apoptosis as shown during *Shigella* infection. *Shigella flexneri* infections of humans can cause tissue destruction in the colon resulting in dysentery. Clearance of the infection is predominantly mediated by macrophages. As a survival strategy *Shigella* evolved an escape mechanism from the phagolysosome that involves caspase-1-dependent apoptosis of macrophages. TPPII-dependency of this essential mechanism of pathogen survival was suggested in *in vitro* experiments (Hilbi et al., 1998; Hilbi et al., 2000).

Further indications for the involvement of TPPII in apoptotic processes were obtained through the analysis of TPPII KO-mice. These mice displayed a $CD8^+$ T cell- and fibroblast-specific induction of cell death, which led to an immunosenescene-like phenotype and decreased life span (Huai et al., 2008). However, mice with a gene-trap disrupting the *tpp2* gene, which resulted in a 90%-reduced TPPII level, showed no phenotype (Kawahara et al., 2009).

Studies using γ-radiation and DNA-damaging agents in a murine cell culture model provided additional evidence for a role of TPPII in cell death- and DNA-damage-related processes. Initial studies proposed a translocation of TPPII into the nucleus and a TPPII-dependent stabilization of p53 (Preta et al., 2010a; Preta et al., 2009). However, this is controversially discussed as only the general participation of TPPII in DNA-damage response and cell death but not the translocation into the nucleus and the p53-stabilization could be confirmed (Firat et al., 2009).

Rose et al. identified a membrane-bound version of TPPII, which degrads the satiety hormone CCK8. Inhibition of TPPII reduced the food intake of both rats and mice (Rose et al., 1996). Additionally, it was reported that TPPII not only influences food intake but can also regulate fat storage in both *C. elegans* and mice. Fat storage regulation by TPPII seems to be independent of its proteolytic activity (McKay et al., 2007). The potential connection with satiety makes TPPII an interesting target for the treatment of obesity.

1.3.2 Localization and Biochemical Characterization

Most eukarya express TPPII and it has been isolated from *Schizosaccharomyces pombe* (Osmulski and Gaczynska, 1998), *Rattus norvegicus* (Balow et al., 1983; Balow et al., 1986; Rose et al., 1996), *Mus musculus* (Bermingham et al., 1996), *Drosophila melanogaster* (Renn et al., 1998), *Arabidopsis thaliana* (Book et al., 2005) and *Homo sapiens* (Balow et al., 1986; Lees et al., 1990; Wilson et al., 1993). TPPII is a cytosolic protease expressed in most organs such as testis, brain, spleen, kidney, liver, or heart (Rose et al., 1996). By immunofluorescence staining in COS7 (Firat et al., 2007) and EL4 cells (Firat et al., 2009; Preta et al., 2010a; Preta et al., 2009) TPPII was shown to be mainly cytosolic. In addition, a membrane-bound variant, which is thought to be attached to the lipid-bilayer by a glycosyl-phosphatidly-inositol (GPI) anchor, was identified (Rose et al., 1996). The relative amount of this membrane-bound TPPII is tissue-dependent and varies between 31% (brain) and 4% (liver) of total TPPII content. This distribution might reflect different biological functions of TPPII in these tissues (cytosolic: general protein degradation; membrane-bound: degradation of neurotransmitters; (Rose et al., 1996).

The catalytic triad of TPPII was identified for both mouse TPPII (N44, H264, S449) and fly TPPII (N44, H272, S462). The oxyanion formed during catalysis is stabilized by N362 in mouse or N374 in fly (Chuang et al., 2010; Hilbi et al., 2002). Optimal conditions for the exopeptidase activity of *Hs*TPPII are neutral pH (Balow et al., 1983; Balow et al., 1986) and a temperature of ~44°C (Schönegge, 2007). Furthermore, sensitivity of the activity towards chloride was described (Schönegge, 2007; Tomkinson, 2004).

TPPII cleaves tripeptides from the free N-terminus of peptides (Balow et al., 1983; Balow et al., 1986) and a so-called “double- glu” motif in the active-site binding cleft is thought to act as molecular ruler (Chuang et al., 2010; Lindas et al., 2008). This type of motif is known to convey cleavage fidelity to N-terminal exopeptidases after one, two or three residues, respectively. The negatively charged glutamates form charge bridges with the positively charged N-terminus of the substrate (Addlagatta et al., 2006; Engel et al., 2003; Goettig et al., 2002; Xu et al., 2008). For TPPII from *Drosophila melanogaster* (*Dm*TPPII), the existence of a double-glu motif consisting of E312 and E343 was verified by enzymological studies. The main determinant of exopeptidase selectivity is E312, whereas E343 has an auxiliary function (Peters et al., 2011). Cleavage rates are sequence-dependant; proline in the P1 or P1’ position reduces the cleavage rate drastically (Balow et al., 1986). In addition to the exopeptidase activity, a weak endopeptidase activity was reported for TPPII (Geier et al., 1999; Seifert et al., 2003). However, owing to the dominant role of the double-glu motif in substrate alignment the endopeptidolytic cleavage rates are extremely low (Peters et al., 2011).

1.3.3 Domain Structure

Sequence comparison led to the classification of TPPII as a subtilase and the identification of the corresponding domain (see Figure 5A; Chuang et al., 2010; Tomkinson, 1991; Tomkinson and Jonsson, 1991). The subtilisin-like domain is located at the N-terminus and contains a 190-residue insertion between the catalytic active His and Asp (DH-insert). In the DH-insert another domain is inserted, which is called domain C (Rockel et al., 2012). The rest of the TPPII sequence is divided into the central and the C-terminal domain (Chuang et al., 2010). The N-terminal, subtilisin-like domain shows an alpha-beta fold and nearly all secondary structure elements of subtilisin are conserved. The central domain contains a group of subdomains consisting of beta-sheets, whereas the C-terminal domain is α-helical. In *Dm*TPPII monomers, N-terminal and central domain form a ring-like structure with the C-terminal domain as a curved protrusion (see Figure 5B). In the dimer, the monomers are arranged head-to-head, the ring-like structures of the monomers are capped reciprocally and the protrusions form a handle-like structure (see Figure 5C; Chuang et al., 2010).

Bioinformatic analyses of subtilase sequences suggest that the earliest form of a TPPII-like protease was extracellular and contained only the subtilase domain (without the DH-insert) plus the N-terminal part of the central domain. The relocalization of the eukaryotic form of TPPII to the cytosol might have provided the evolutionary pressure for its oligomerisation and self-compartmentalization, which required the acquisition of additional domains like the DH-insert, the central domain and especially the C-terminal domain (Rockel et al., 2012).

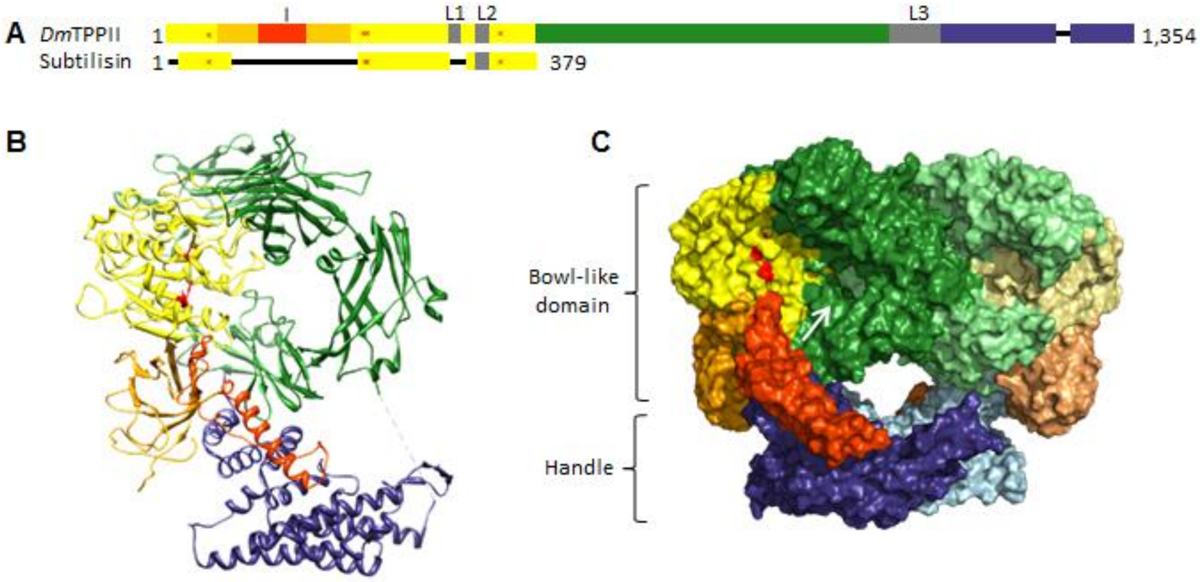

Figure 5: Crystal structure of the *Dm*TPPII dimer

(A) Schematic representation of the primary structure of Drosophila TPP II (DmTPPII) depicting the domains found in the crystal structure. The subtilisin-like domain is colored in yellow (residues 1–522) contains the active-site residues (red stars), loop L2 (residues 441–460), loop L1 (residues 408–417) and the DH-insert (I) with domain C, which are colored in orange (residues 75–266) or red orange (residues 137-201), respectively; the central domain (residues 523–1098) in green containing L3 loop (residues 1027–1098), C-terminal domain in blue (residues 1099–1354, blue). **(B)** Ribbon diagram of a monomer (color scheme as in A). The active-site residues are shown in stick format (red). **(C)** Surface representation of a TPP II dimer (color scheme as in A); red, active-site. The two monomers are oriented head-to-head; the ring-like structure of one monomer is closed off by the adjoining monomer (white arrow). The protrusions of the two bowls meet to form a handle (adapted from Chuang et al., 2010).

1.3.4 The Spindle Complex

The quaternary structure of TPPII has been studied for years. In 1987 Macpherson (Macpherson et al., 1987) published the first electron micrographs of negatively stained native *Hs*TPPII particles depicting arrangements of ‘limiting units’ in single and double bows (see Figure 6A). Upon dialysis these complexes dissociated into oligomers of various sizes (see Figure 6B; Harris and Tomkinson, 1990; Macpherson et al., 1987). Attempts of structure determination by image analysis of 2D-crystals (see Figure 6C) were unsuccessful, probably because the 2D-crystals were not sufficient in size and regularity (Harris and Tomkinson, 1990). The image analysis of negatively stained murine TPPII particles showed views with constrictions at different positions in the complex (see Figure 6D; Geier et al., 1999). In negative stain, TPPII particles adopt only a limited number of orientations, which impairs structure analysis. Under cryo-conditions, when the particles are embedded in vitreous ice, the ‘navette’-view is still the dominant view, but also various ‘dumbbell’-, ‘fish’- and end-on-views are observed (see Figure 6E). This preparation method allowed the first 3D-reconstruction of the *Dm*TPPII complex, which confirmed the previously reported spindle-shaped architecture with two strands twisted around each other (Rockel et al., 2002). In *Dm*TPPII, both strands consist of 10 stacked dimers (see Figure 7A; Chuang et al., 2010; Rockel et al., 2005) and the molecular weight of the complex is ~5-6 MDa (Rockel et al., 2002).

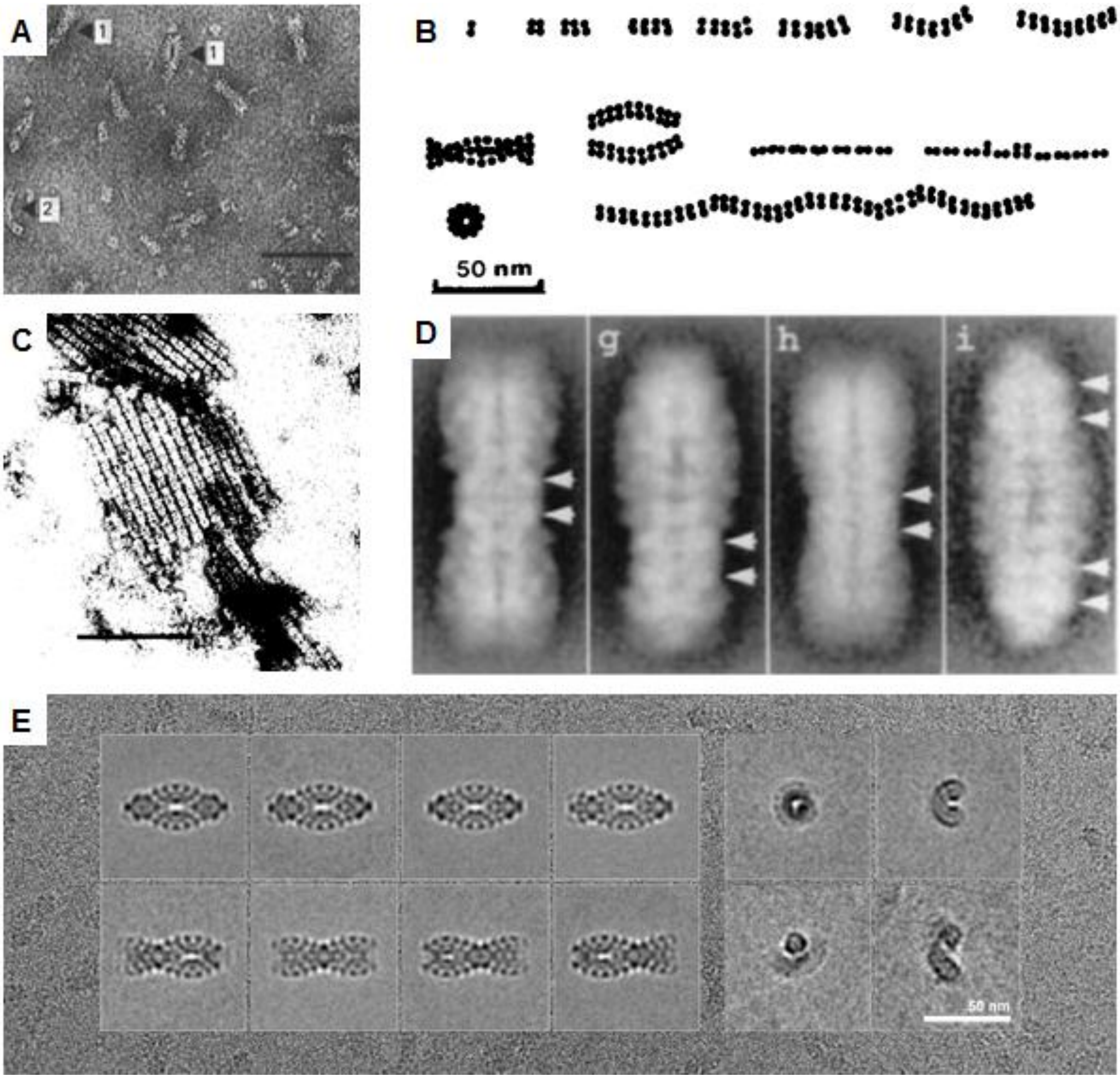

Figure 6: Studies of the quaternary structure of TPPII

(A) Electron micrograph of negatively stained native *Hs*TPPII with 1, double-bow structure of two different kinds, and 2, single-bow structure. Bar indicates 100 nm. **(B)** Schematic representation of varying oligomeric states of native *Hs*TPPII in curved higher oligomers or a single-bow complex (upper row) and in the double bow structure together or the linear arrangements of the dimers (lower row). **(C)** Electron micrograph of native *Hs*TPPII 2D-crystals. Bar indicates 100 nm. **(D)** Class averages of 1365 negatively stained murine TPPII particles **(E)** Class averages of *Dm*TPPII particles in vitreous ice. Background: electron micrograph of *Dm*TPPII particles in vitreous ice (adapted from Macpherson et al., 1987 (A); Harris and Tomkinson, 1990 (B+C); Geier et al., 1999 (D); Rockel et al., 2002 (E)).

Recently the hybrid structure of *Dm*TPPII was obtained and the positions of the domains within the TPPII spindle could be determined: N-terminal domains plus central domains form the corpus of the strands and C-terminal domains build the handles at the convex side (see Figure 7B; Chuang et al., 2010; Rockel et al., 2012). The active-sites are sequestered within a cavity system. The system consists of a longitudinal channel traversing the strands, an antechamber and two catalytic chambers at each dimer-dimer interface (see Figure 7C/D/E). To reach any of the sequestered active-site, a substrate has to cover a distance of ~ 120 Å (Chuang et al., 2010).

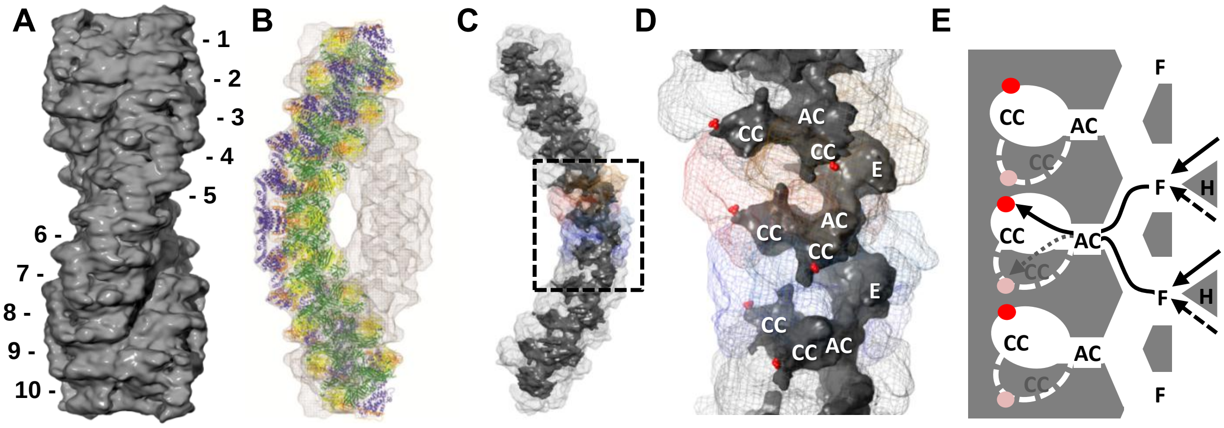

Figure 7: The spindle complex of *Dm*TPPII

(A) 3D-map of *Dm*TPPII spindle with a resolution of ~14Å ($FSC_{0.5}$). **(B)** The X-ray structure of *Dm*TPPII dimers fitted in the 3D map. The N-terminal domain is colored in yellow, the DH-insert in orange, the central domain in green, the C-terminal domain in blue; the EM map is shown in mesh. **(C)** Surface model of a single strand low-pass filtered to 12-Å resolution showing both the external surface (in transparent mesh and internal surface (solid gray) to aid visualization of the chamber system. **(D)** Zoom into box in C. Red spheres, Ser462 residues. **(E)** Schematic layout of TPP II chambers. H, handle; F, foyer; AC, antechamber; CC, catalytic chamber. Active-sites are represented as red dots within catalytic chambers in the plane of the figure and as pale red dots for the catalytic chambers closest to the viewer (outlined by white dashed lines). Black arrows, multiple pathways to reach the active-sites; black dashed line, route to the catalytic chamber closest to the viewer (adapted from Rockel et al., 2012 (A+B); Chuang et al., 2010 (C-E)).

1.3.5 Activation Mechanism

The proteolytic activity of TPPII is assembly-dependent and correlated to the number of dimer-dimer interfaces (see Figure 8A; Seyit et al., 2006; Tomkinson, 2000). TPPII dimers exhibit approximately 10% of the activity of fully assembled spindles (Seyit et al., 2006; Tomkinson, 2000). This low activity of TPPII dimers was attributed to i) three loop residues of loop L2 that are bound in the active-site cleft and to ii) the displacement of the active-site serine by ~5 Å from the catalytically active position. The displacement of the active-site serine is accompanied by a difference in secondary structure between TPPII and subtilisin in the active-site region: in TPPII, the helix harboring the active-site serine is shorter by one turn (see Figure 8B-D). It was speculated that binding of loop L2 into the active-site cleft not only precludes binding of substrate but also prevents the catalytic active conformation of the active-site serine (Chuang et al., 2010).

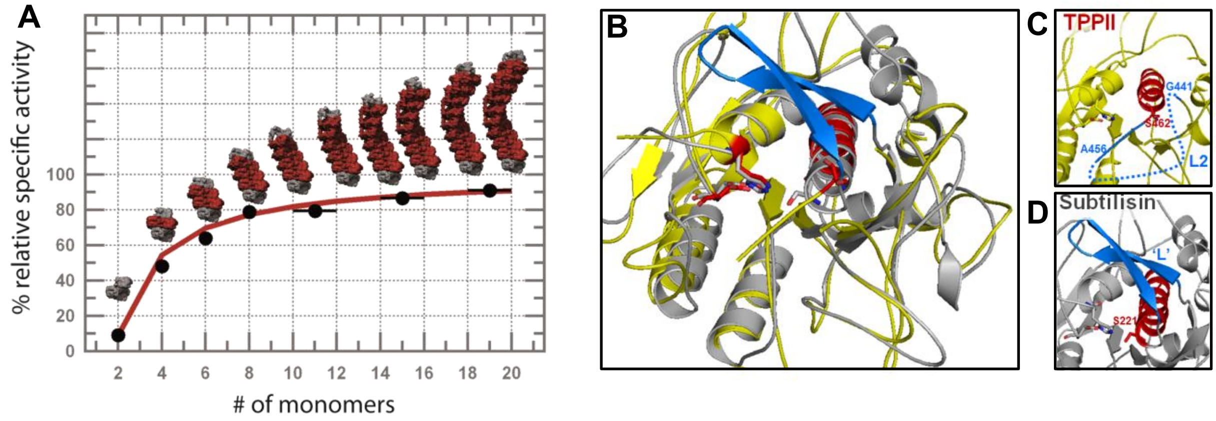

Figure 8: Specific activity and active-site conformation of TPPII

(A) Dependency of the specific activity on the assembly status of TPPII. **(B)** Superimposition of the active-site region of TPPII (PDB:3LXU; yellow/red) and subtilisin BPN'(PDB:1CSE; grey/blue). **(C-D)** Conformation of the helix harboring the active-site serine and the connected loop L2 or loop 'L' of TPPII (C) and subtilisin (D; adapted from Seyit et al., 2006 (A); Chuang et al., 2010 (B-D)).

In order to activate TPPII, the three-residue segment of loop L2 must be removed from the active-site cleft and the active-site serine must be repositioned into an active conformation. As the peptidase domain of TPPII shows a high sequence and structure similarity to subtilisin, it is likely that the active-site region of activated TPPII resembles that of subtilisin (see Figure 8D). Long loops of both TPPII and subtilisin, designated loop L2 and loop 'L', respectively, are directly linked to the respective active-site serines. In subtilisin, loop 'L' forms a stable antiparallel β-sheet that is tethered down by hydrogen bonds established with several residues from other regions of the protein (see Figure 8B/D; Bode et al., 1987). Residues G442 to Q456 of loop L2 are not resolved in the crystal structure of *Dm*TPPII dimers, which suggests that loop L2 is flexible (see Figure 8B-C; Chuang et al., 2010). It was proposed that, to activate a TPPII dimer, loop L2 undergoes a conformational change, which allows the establishment of a hydrogen bond network similar to the one of subtilisin.

In the hybrid structure of *Dm*TPPII a strong density that is not accounted for by the atomic model is visible at the dimer-dimer interface close to the active-site serine (see Figure 9A-C). Superimposition of subtilisin and docked *Dm*TPPII models showed that the loop 'L' of subtilisin could be accommodated by this density. It was suggested that in the assembled complex loop L2 takes up a similar position as loop 'L' in subtilisin and that this new position is stabilized by interactions of loop L2 with residues of the neighboring dimer (Chuang et al., 2010).

Based on these assumptions a model for assembly-dependent activation was proposed: TPPII dimers show a low activity because the active-site serine is displaced and a three-residue segment of loop L2 is bound to the active-site cleft. As dimers stack to form strands, loop L2 leaves the active-site cleft and establishes new interactions with residues from the neighboring dimer at the roof of the catalytic chamber. Concomitantly, a hydrogen bond network similar to that in subtilisin is established at the active-site region, which positions the active-site serine in an active conformation (see Figure 9D; Chuang et al., 2010).

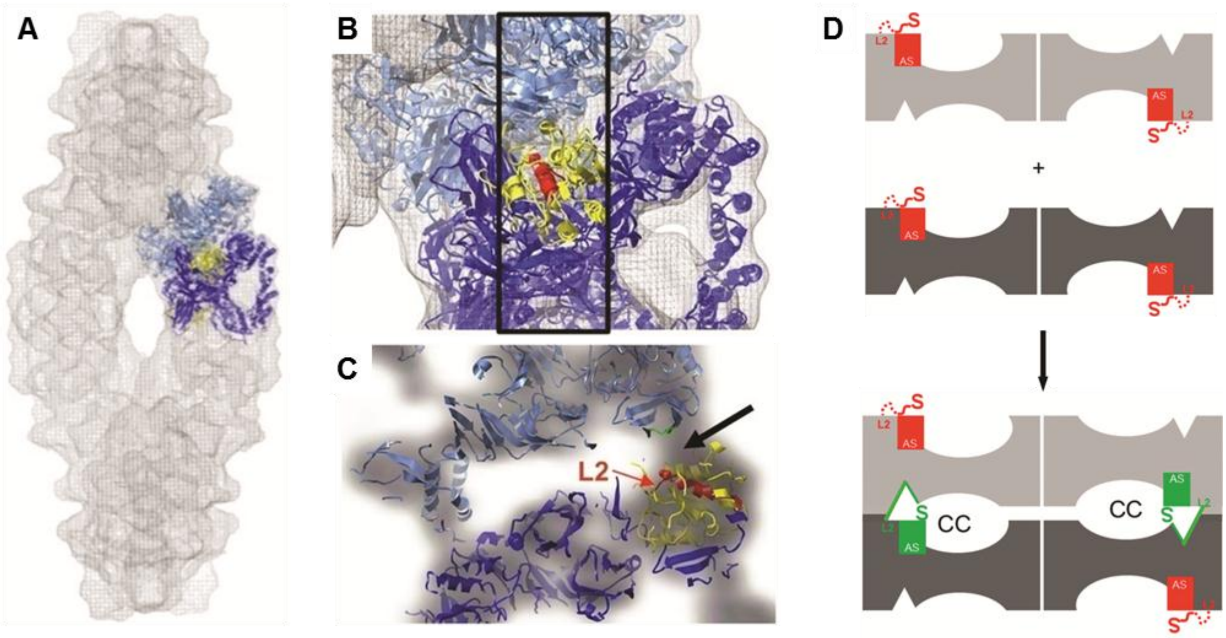

Figure 9: Proposed activation mechanism of TPPII

(A) Two docked dimers are shown in light and dark blue. In the lower dimer, the subtilisin-like domain is shown in yellow. **(B)** Enlarged region of A; region 441–480 (helix-Ser462-L2) is shown in red. The box marks the slab containing the helix connected to the active-site Ser462 and L2. **(C)** Orthogonal view of boxed region in B. The black arrow shows the density unaccounted for by the model at the proposed relocation site of L2 (red) in the spindle. The proposed interaction area of loop L2 is highlighted in green. **(D)** In low-active TPP II dimers (top), the L2 loops (red) are flexible, but a three-residue segment of these loops occupies the substrate-binding clefts. The active-site (AS) serines, Ser462 (red S), are coupled to the L2 loops and are displaced away from the other members of the catalytic triads. Upon association of the dimers (bottom), the catalytic chambers (CC), which enclose the active-sites, are formed at the dimer-dimer interface. At the same time, the L2 loops (green) interact with the chamber-roof residues of an adjacent dimer, leading to accessible substrate-binding clefts and the relocation of the active-site serines (green S) to a catalytically active position (adapted from Chuang et al., 2010).

1.4 Aim of this work

Up to now, all high resolution structural data has been obtained with *Dm*TPPII, whereas the biological functions of TPPII have mainly been studied in mammalian systems. *Dm*TPPII and human TPPII (*Hs*TPPII) differ in several properties such as specific activity, complex stability, sequence length, and sequence identity. To enable results of functional studies of mammalian TPPII to be correlated with its structure, one goal of this work was to obtain the high-resolution structure of *Hs*TPPII spindles.

Since the activation model proposed earlier had postulated conformational changes at the dimer-dimer interface (Chuang et al., 2010), another goal was to analyze these interfaces in the structures of *Hs*TPPII and *Dm*TPPII spindles and to probe regions potentially critical for activation by a profound mutational analysis.

2 Results

2.1 Structure Determination of *Hs*TPPII

2.1.1 Purification and Electron Microscopy of *Hs*TPPII Spindles

So far, all published purification protocols of native mammalian TPPII have yielded rather small amounts of protein, which was not suitable for detailed structural analysis (Harris and Tomkinson, 1990; Macpherson et al., 1987). In order to overcome the obstacle of limited access to *Hs*TPPII, a recombinant expression system was established in *E. coli*. An initial attempt to adapt the purification procedure of recombinant *Dm*TPPII to *Hs*TPPII yielded pure *Hs*TPPII spindles, which was, however, not suitable for cryo electron microscopy (cryo-EM) in quality and concentration (Schönegge, 2007).

The main problem in the purification of *Hs*TPPII was that the first step in the purification procedure of *Dm*TPPII – Polyethyleneimine (PEI)-precipitation under conditions causing disassembly of the TPPII complex into smaller oligomers (pH 8.9; Seyit et al., 2006) – could not be applied to *Hs*TPPII. Without a prior PEI-precipitation step, the losses occurring in all following purification steps were much higher than for *Dm*TPPII. Hence, a different enrichement step had to be introduced as the first step of the purification procedure. An N-terminal His_6-tag had shown not to interfere with folding and assembly of murine TPPII during expression in HEK-293 cells and *Pichia pastoris* (Lindas et al., 2008) and of *Dm*TPPII during expression in *E. coli* (Seyit, 2006). Therefore, to improve the yield of recombinant *Hs*TPPII from *E. coli*, a His_6-tag was added to the N-terminus of *Hs*TPPII (see Figure 10A) and a modified purification procedure was developed (see Figure 10B). After lysis of the *E. coli* cells, the lysate was filtered and subjected to immobilized metal ion affinity chromatography (IMAC). The majority of the His_6-tagged protein was bound to the nickel-ions of the HisTrap-column (see Figure 10C). To reduce non-specific binding, all buffers contained 300 mM NaCl and a wash step with 50 mM imidazole was introduced. The target protein was eluted by a step gradient; *Hs*TPPII eluted at 200 mM imidazole. As TPPII activity is sensitive to imidazole (J. Peters; personal communication), the imidazole was removed by buffer exchange via a PD10 column. Further purification was achieved by an ion exchange chromatography (IEX) step using an ANX-column. The activity of the fractions was monitored by measuring Amc-release from the fluorogenic substrate AAF-Amc. Fractions showing high activity were combined and concentrated by ammonium sulfate (AS) precipitation. The final purification step, which yielded homogeneous, high molecular weight complexes of TPPII, was size exclusion chromatography (SEC) on a Superose 6. This procedure reproducibly yielded pure *Hs*TPPII in large amounts (~2.5 - 3.5 g *Hs*TPPII from ~45 - 75 g *E. coli* lysate; see Figure 10C). Integrity and homogeneity of the purified protein were monitored by electron microscopy (EM). Negative stain images showed that purified recombinant *Hs*TPPII complex formed intact spindles and that the spindle complexes of recombinant and native *Hs*TPPII have identical morphology (see Figure 10D/E). The established purification of recombinant *Hs*TPPII enabled a detailed structural analysis of *Hs*TPPII.

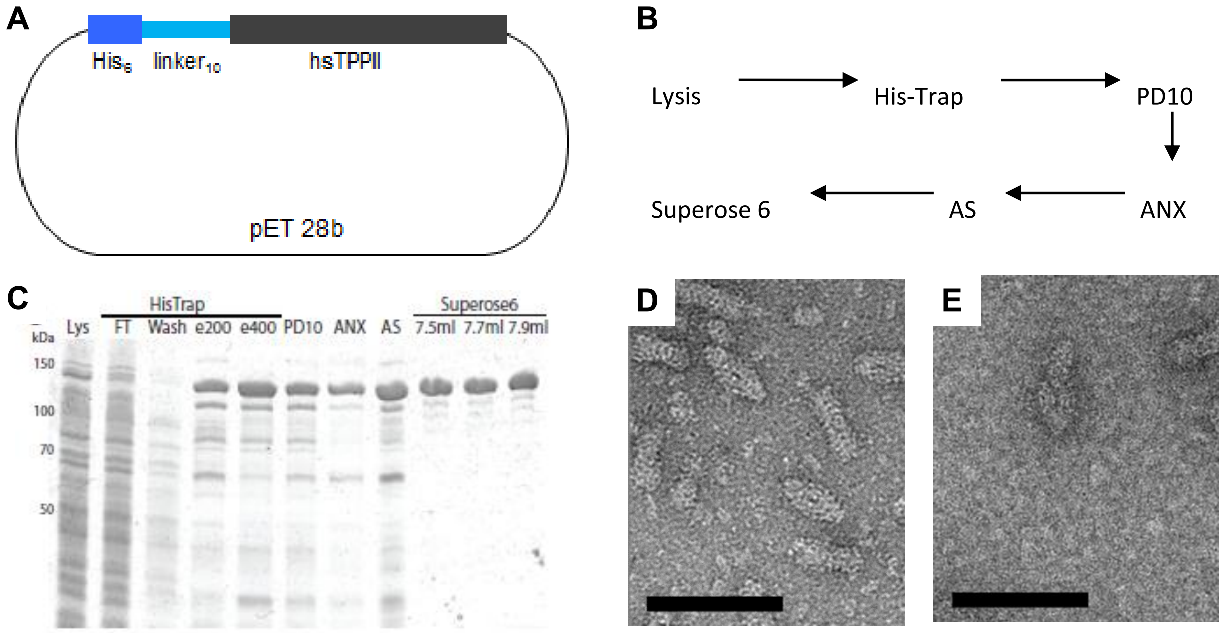

Figure 10: Purification of recombinant *Hs*TPPII spindles

(A) Schematic drawing of the plasmid containing the gene for N-terminally His$_6$-tagged *Hs*TPPII. **(B)** Sequence of the purification steps for *Hs*TPPII spindles. **(C)** SDS-PAGE analysis of purification steps of recombinant *Hs*TPPII from *E. coli*. **(D-E)** Electron micrograph of negatively stained recombinant (D) and native (E) *Hs*TPPII particles contained in the peak fraction of the Superose 6 purification step. Scale bars: 100 nm (adapted from Schönegge et al., 2012 (C-E)).

For data collection in cryo-EM, the sample was prepared freshly and grids were loaded and plunge-frozen directly after the elution of the protein from the size exclusion column. As a rule a concentration of 0.2 - 0.3 mg/ml of *Hs*TPPII was used. Focal pairs were recorded (see Figure 11A) and in 2248 images 96116 particles were picked manually. The x-y positions of the particles determined in the far-from-focus images were transferred to the close-to-focus images and the particle images were extracted in 384 x 384 boxes. For the reconstruction, the projection direction of each projection was determined by projection matching. The initial reference - a featureless double bow (see Figure 11B) - was projected in different directions and the resulting projections were compared one by one with the experimental data. This comparison gave a first, rough estimate of the Euler angles of the experimental images of the particles. To obtain a 3D-reconstruction, the images were added up in Fourier space corresponding to their orientation. The resolution of this 3D-map depended on the accuracy of the Euler angle determination. Therefore, the resolution of the first 3D-reconstruction with only roughly determined Euler angles was low. The procedure was repeated and each round of the 3D-reconstruction of the previous iteration was used as starting model. The process was performed until the Euler angles stabilized. The 3D-reconstruction of the last iteration (see Figure 12A) had a resolution between 9.9 Å and 6.9 Å ($FSC_{0.5}$ or $FSC_{0.3}$, respectively; see Figure 11C).

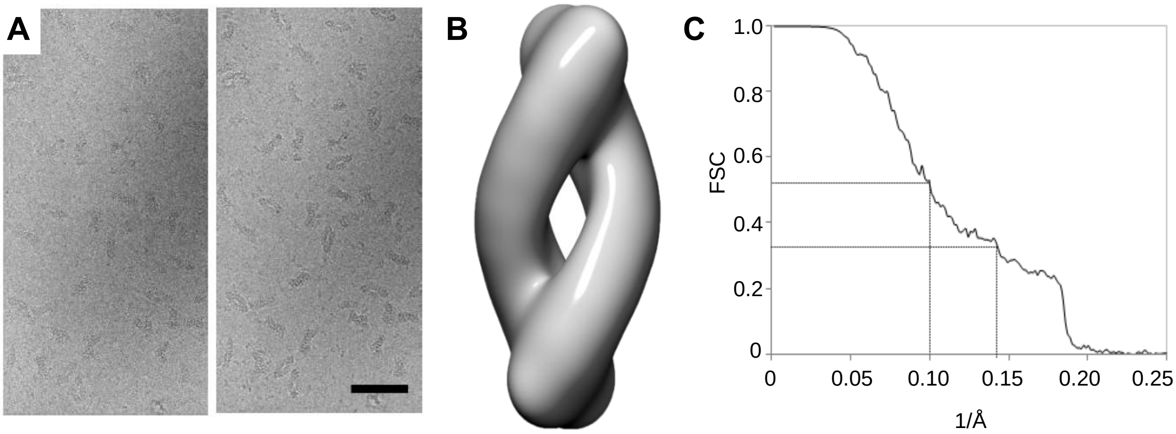

Figure 11: Cryo-EM and 3D-reconstruction of *Hs*TPPII spindles

(A) Focal pair of ice-embedded particles with defocus-settings: –1.0 µm (left), –3.0 µm (right). Scale bar: 100 nm. **(B)** Featureless double-bow used as initial reference **(C)** Fourier shell correlation (FSC) of the 3D-reconstruction (adapted from Schönegge et al., 2012 (A-B)).

2.1.2 3D-Structure of *Hs*TPPII

*Hs*TPPII forms a large complex with dimensions of 55 x 28 nm and the strands are built of nine stacked dimers (see Figure 12A). Similar to *Dm*TPPII, each strand enclose a cavity system consisting of a longitudinal channel and a suite of chambers at each dimer-dimer interface (see Figure 12B-D). This suite of chambers is created by the architecture of TPPII dimers: Each dimer consists of a ‘handle’ and a globular part composed of the stacked tori of the monomers. From the crystal structure of *Dm*TPPII it is known that that the subtilase-domain constitutes one segment of the torus and that the active-site of one monomer faces up while the other one faces down (see Figure 12E). Through stacking of dimers the hollows in the tori get capped, which leads to the formation of the catalytic chambers. In the spindle, the interspaces between the handle and the torus form the longitudinal channel and the entrance to the cavity system (see Figure 12E).

In *Dm*TPPII, densities connecting the handle and the globular part were observed in the terminal dimers only and were ascribed to loop L3 (Chuang et al., 2010). Similar densities are visible in all dimers of *Hs*TPPII and they subdivide the large entrance (27 Å x 40 Å) into two smaller openings (27 Å x 23 Å; 27 Å x 27 Å, see Figure 12F). Loop L3 is more easily discernible in *Hs*TPPII than in *Dm*TPPII, which might be either due to the superior resolution of the 3D-model of *Hs*TPPII or a less flexible conformation of loop L3 in human TPPII.

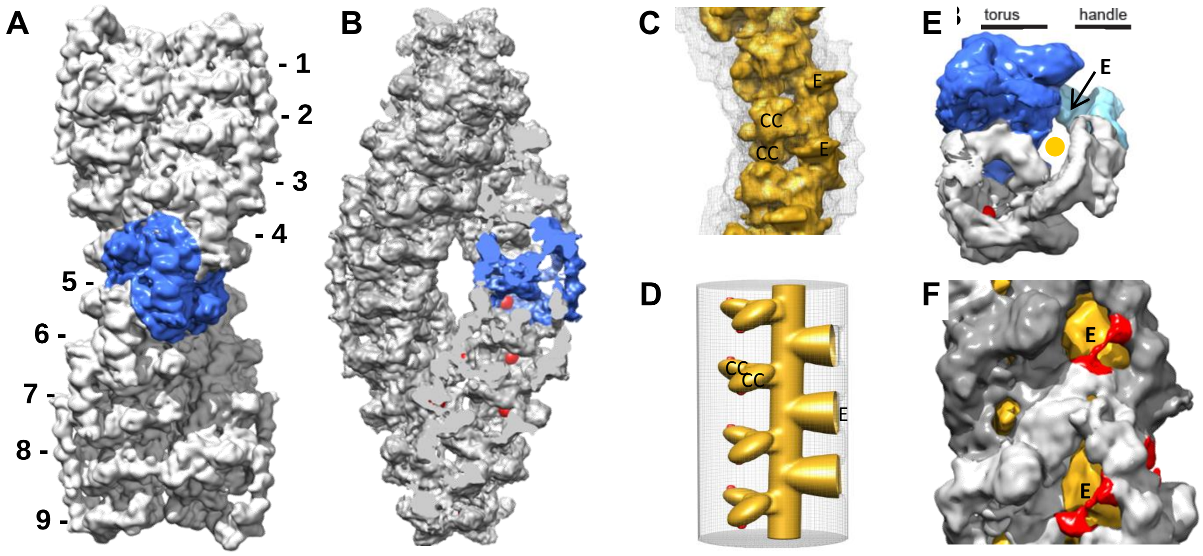

Figure 12: 3D-reconstruction of *Hs*TPPII

(A) Surface representation of the *Hs*TPPII model with a resolution between 9.9 Å ($FSC_{0.5}$) and 6.9 Å ($FSC_{0.3}$) in 'dumbbell' view. Dimers of one strand are numbered. Dimer five is highlighted in blue. **(B)** Same as A rotate about 90° around the longitudinal axis. The strand on the right is cut open in order to show the cavity system. Active-sites are shown in red **(C)** Surface model of a segment of a single strand showing the external surface in gray mesh and the cavity system in yellow; CC: catalytic chamber, E: Entrance**.** **(D)** Schematic representation of the cavity system external surface in gray mesh; cavity system in yellow; active-sites in red; CC: catalytic chamber, E: Entrance. **(E)** Segmented dimer: one monomer is colored in gray; the other in dark and pale blue. Dark blue represents the torus and pale blue the handle**.** The yellow circle indicates the interspace forming the channel and the arrow shows the entrance to the cavity system. The active-site is shown in red. **(F)** Entrances to the cavity system: Dimers are colored in dark and light gray; density corresponding to loop L3 is shown in red, the cavity system is shown in yellow; E: Entrance (adapted from Schönegge et al., 2012).

2.1.3 Hybrid Structure of *Hs*TPPII

With the aim of interpreting the 3D-reconstruction of *Hs*TPPII beyond its nominal resolution, initially the atomic model of *Dm*TPPII was docked into the 3D-map of *Hs*TPPII. The fit was good (ccc = 0.81), but some regions of this crystal structure were not accounted for by the 3D-map. This had to be expected, since the analysis of the sequences of *Dm*TPPII and *Hs*TPPII revealed an overall similarity of only 54% and an identity of 35%. In addition, the sequence of *Hs*TPPII is 105 aa shorter. The most prominent differences are located in loop L3 and the C-terminal domain (see Figure 13A). In order to have a more accurate means for analyzing the density of the *Hs*TPPII spindle, an alignment of various TPPII sequences and the atomic coordinates of *Dm*TPPII dimers were used to create a comparative model of *Hs*TPPII dimers (see Figure 13B).

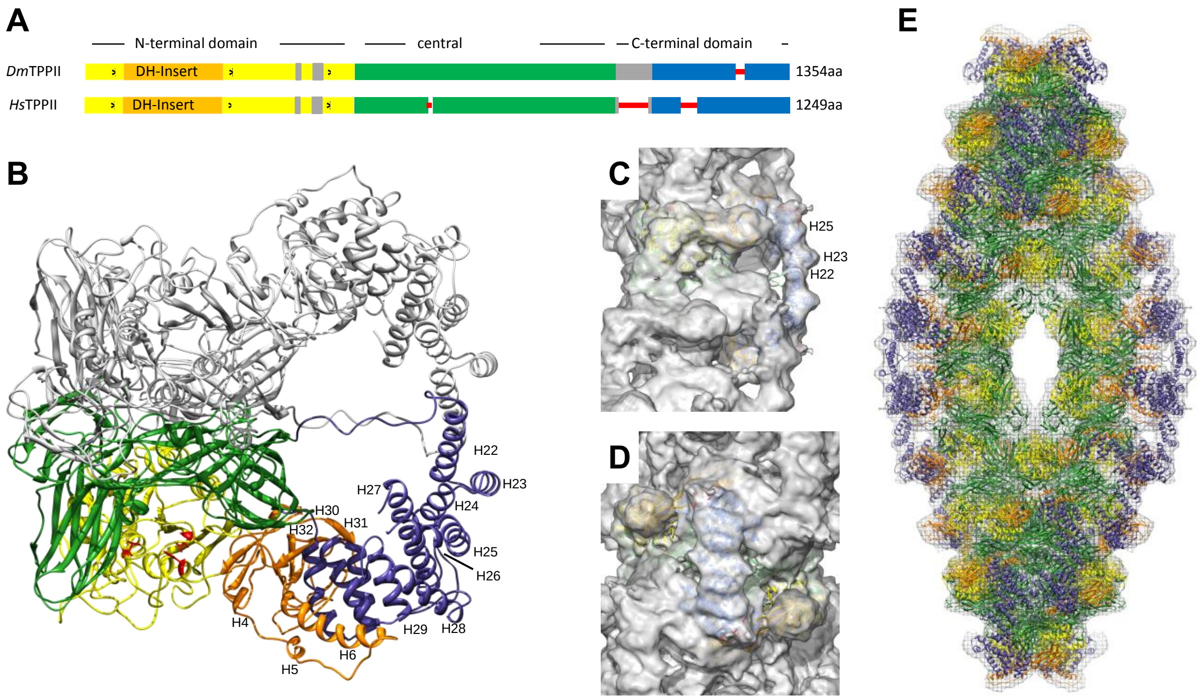

Figure 13: Hybrid structure of *Hs*TPPII

(A) Schematic sequence alignment of DmTPPII and HsTPPII; the N-terminal domain is colored in yellow, the DH-insert in orange, the central domain in green, the C-terminal domain in blue, missing sequence stretches in red. **(B)** Ribbon diagram of a dimer of the comparative model of HsTPPII. The domains of one monomer are colored as in A and the active-site residues are shown in red. The helices of one C-terminal domain and of one DH-insert are numbered. **(C-D)** Comparative model flexibly fitted into the 3D-map in side (C) and front view (D; ccc= 0.92); the 3D-map is shown as transparent surface model in grey; the comparative models are in ribbon representation and domain color coded. **(E)** Hybrid model of HsTPPII; the dimers are colored as in A (adapted from Schönegge et al., 2012).

The quality of the rigid body fit of this comparative model into the EM-map of *Hs*TPPII spindles was lower than the fit of the coordinates of the *Dm*TPPII dimer (ccc = 0.70), mainly because of differences in the conformation of the handle region in the *Hs*TPPII model. This deviation is probably due to the extended morphology of the handle region, which results in relatively few restraints from the template for the homology-modeling process. The rigid body fit resulted in steric conflicts at the dimer-dimer interfaces (1,147 to 1,531 clashes between atoms). Additionally, the dimer-dimer interfaces are only quasi-identical and, as a consequence, the conformation of a TPPII dimer depends on its position in the spindle. To observe these conformational differences in detail, ‘molecular dynamics flexible fitting’ (MDFF) was used to morph the structure of the dimers to conform with the EM-density, while maintaining the stereochemistry of the protein model. The resulting hybrid structure of *Hs*TPPII features a superior fit of the atomic models (ccc = 0.9 – 0.92; see Figure 13C-E).

In the comparative model of *Hs*TPPII three sequence stretches were removed: i) aa M1-P17, ii) aa E83-K109 and iii) aa V1095-P1105. The N-terminal amino acids were excluded from the comparative model because they are missing in the crystal structure of *Dm*TPPII and cannot be modeled reliably. The loop regions E83-K109 and V1095-P1105 were modeled. However, after rigid body fitting of the dimers into the EM-map they were entangled. Since this problem could not be solved by MDFF these regions were deleted from the model.

At subnanometer resolution an EM-map should allow the recognition of α-helical regions. The most extended α-helical region in TPPII is the handle, which, in the comparative model of *Hs*TPPII, includes helices H4 – H6 of the DH-insert and helices H22 – H32 of the C-terminal domain. Indeed helices H22, H23 and H25 of the handle are clearly discernible in the EM-map at the outer, convex region (see Figure 13C-D and Figure 14).

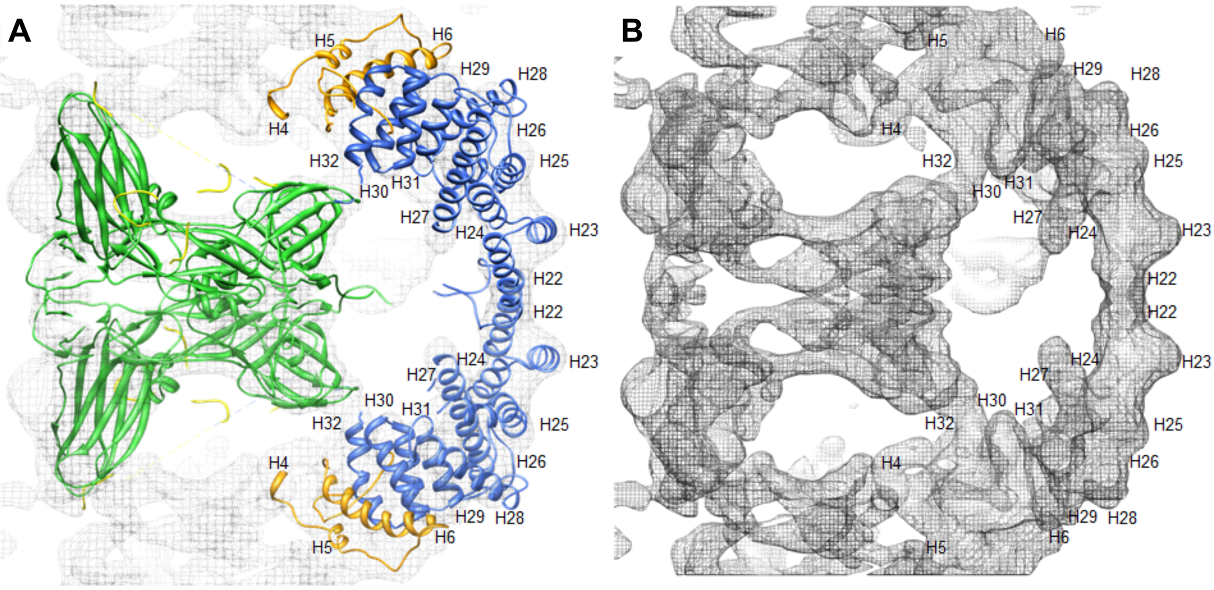

Figure 14: Discerning α-helices in the hybrid model

(A) Section of the hybrid structure of HsTPPII showing one dimer (the N-terminal domain is colored in yellow, the DH-insert in orange, the central domain in green, the C-terminal domain in blue) and the EM-map in mesh. Helices are numbered. **(B)** Same section of the hybrid structure as in A) but only the EM-map is shown.

2.1.4 The DH-Insert at the Dimer-Dimer Interface

The elongated structured protrusion within the DH-insert is termed ‘domain C’ (Rockel et al., 2012) and participates in the formation of the handle (see Figure 14A). In the comparative model of *Hs*TPPII, domain C consists of a long α-helix (H6) and an extended loop region into which another, short α-helix (H5) is embedded (see Figure 13B, Figure 14A). In the spindle complex, domain C and especially its extended loop region is in close proximity to helix H27 of the same dimer and to domain G and loop L3 of the neighboring dimer. The regions of domain C, helix H27 and loop L3 that contact each other are charged and conserved in mammals (see Figure 15). The interaction of loop L3 and the DH-insert might be needed to keep loop L3 in its position across the entrance to the cavity system.

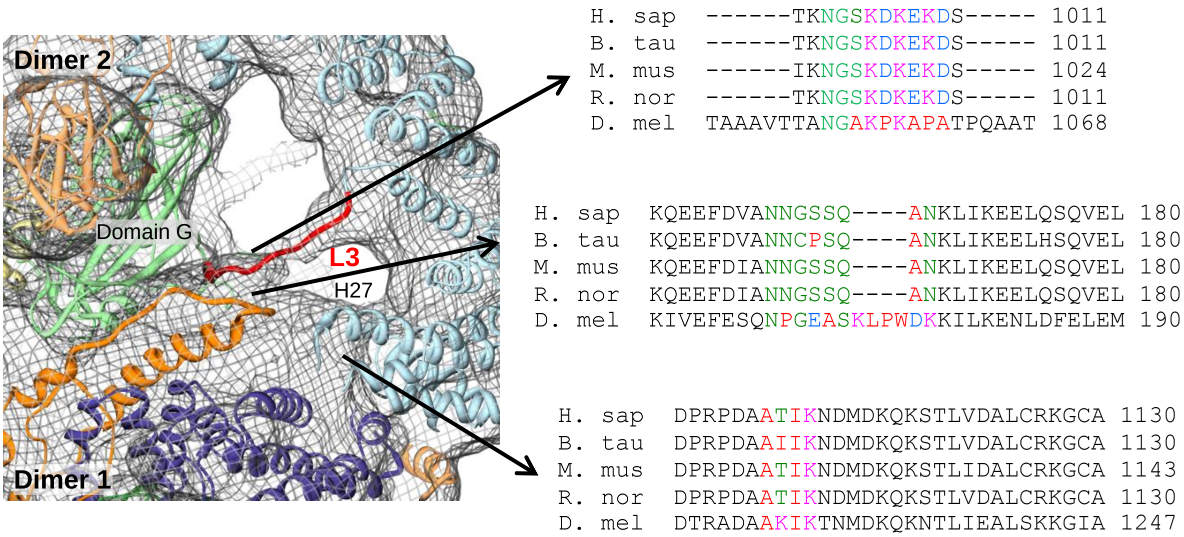

```
H. sap  ------TKNGSKDKEKDS----- 1011
B. tau  ------TKNGSKDKEKDS----- 1011
M. mus  ------IKNGSKDKEKDS----- 1024
R. nor  ------TKNGSKDKEKDS----- 1011
D. mel  TAAAVTTANGAKPKAPATPQAAT 1068

H. sap  KQEEFDVANNGSSQ----ANKLIKEELQSQVEL 180
B. tau  KQEEFDVANNCPSQ----ANKLIKEELHSQVEL 180
M. mus  KQEEFDIANNGSSQ----ANKLIKEELQSQVEL 180
R. nor  KQEEFDIANNGSSQ----ANKLIKEELQSQVEL 180
D. mel  KIVEFESQNPGEASKLPWDKKILKENLDFELEM 190

H. sap  DPRPDAATIKNDMDKQKSTLVDALCRKGCA 1130
B. tau  DPRPDAAIIKNDMDKQKSTLVDALCRKGCA 1130
M. mus  DPRPDAATIKNDMDKQKSTLIDALCRKGCA 1143
R. nor  DPRPDAATIKNDMDKQKSTLVDALCRKGCA 1130
D. mel  DTRADAAKIKTNMDKQKNTLIEALSKKGIA 1247
```

Figure 15: Sequence alignment of regions proximal to the DH-insert

Two docked dimers at the dimer-dimer interface; the DH-insert is colored in orange, the central domain in green, the C-terminal domain in blue, loop L3 in red. The sequence alignments of TPPII sequences from human (*H. sap*), cattle (*B. tau*), mouse (*M. mus*), rat (*R. nor*) and fly (*D. mel*) corresponding to the interaction areas are shown on the right (adapted from Schönegge et al., 2012).

At higher threshold levels, the shape of the EM-density corresponding to domain C resembles that of an α-helical region (see Figure 16A-D). These α-helical characteristics are visible in all in-strand dimers and suggest a helix-turn-helix conformation for domain C. The corresponding density of the terminal monomer, which does not interact with a neighboring dimer, is too ambiguous to allow an assignment. The low resolution of the density corresponding to domain C might reflect the conformational variability in domain C in terminal monomers.

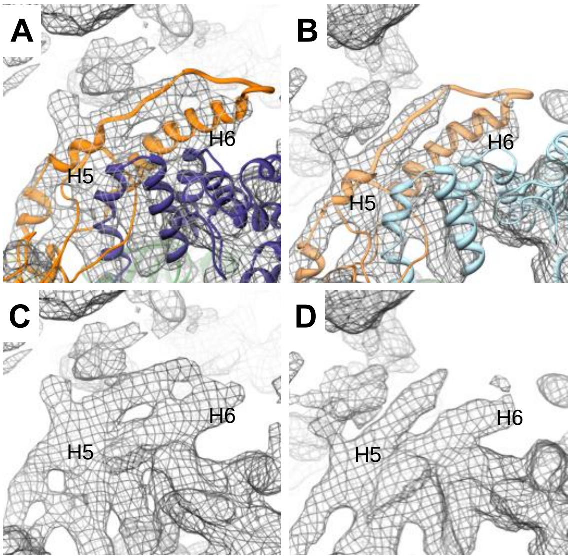

Figure 16: Domain topology of the dimer-dimer interface

(A-B) Close-up of domain C in dimer 1 (A) and in dimer 2 (B). **(C-D)** Same close-up as in A,B but only the EM-density of dimer 1 (C) or dimer 2 (D) is displayed. DH-insert is colored in orange, C-terminal domain in blue (adapted from Schönegge et al., 2012).

2.1.5 Conformations of In-strand vs. End-of-strand Dimers

Activation of TPPII is proportional to the number of dimer-dimer interfaces (Seyit et al., 2006) and the activation model implies the existence of different conformations of active and inactive TPPII dimers. In-strand and end-of-strand dimers have different molecular environments: in-strand dimers are covered from both sides by neighboring dimers, (see Figure 17A); whereas end-of-strand dimers have only one neighbor (see Figure 17B). Hence, end-of-strand dimers are supposed to be not fully activated and their conformation probably differs from the conformation of in-strand dimers.

The conformations of flexibly fitted dimers were analyzed with respect to their position within the spindle, which is either in-strand or end-of-strand. Due to the D2 symmetry used for 3D-reconstruction and during MDFF, only four unique in-strand dimer conformations and only one unique end-of-strand dimer conformation can be analyzed. To determine differences between the four in-strand conformations, we calculated the root-mean-square fluctuation (RMSF) of each C_α-atom. The major part of in-strand dimers was invariable with RMSF-values < 2 Å; nevertheless, a few regions appeared to differ in conformation with RMSF-values between 2 Å and 3.8 Å (see Figure 17C). These regions mainly consist of loops, notably including loop L2 and loop L3 (see Figure 17E/F/I/K) and their fluctuations, although potentially meaningful, cannot be interpreted reliably.

As the conformation of in-strand dimers appears to be uniform, the average positions of their atoms were calculated and compared to the conformation of end-of-strand dimers. The majority of C_α-atoms are invariable with RMSF-values < 2 Å. Differences between the two conformations (RMSF: -2 Å - 4.8 Å) could be observed for similar loop regions as in in-strand dimers (see Figure 17D/G/H) and, additionally, for the following three α-helices in the handle region: i) N-terminal region of helix H6, ii) N-terminal region of helix H27 and, iii) C-terminal region of helix H26 (see Figure 17D/J/L). Interestingly, these helices are located within or close to the dimer-dimer interface. Consequently, it is likely that the conformation of these regions is influenced by dimer-dimer interactions.

In summary, only the positions of some α-helices in the handle region differ between in-strand and end-of-strand dimers. The structural flexibility of these α-helices suggests a functional relevance, which could be the fine-tuning of the entrance region and the translation of the assembly status into activation.

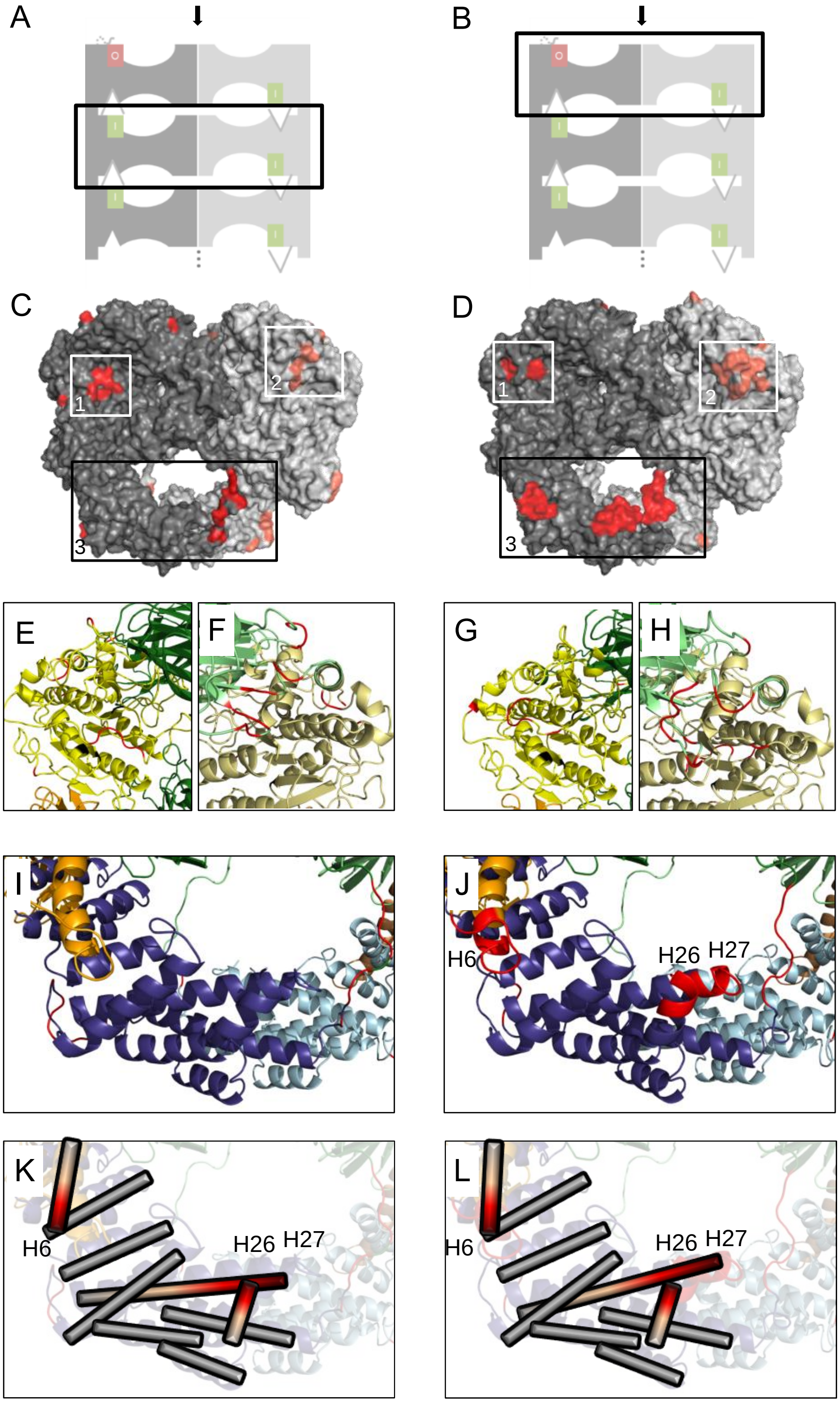

Figure 17: Conformations of in-strand and end-of-strand dimers
(A-B) Schematic representation of in-strand dimers (A) and end-of-strand dimers (B; dimers in black box). **(C-D)** Molecular surface representation of in-strand dimers (C) and end-of-strand dimers (D); monomers are colored in dark and light grey; variable regions in red. **(E,G)** Enlarged ribbon representation of boxed region 1 in C (E) or D (G). **(F,H)** Enlarged ribbon representation of boxed region 2 in C (F) or D (H). **(I,J)** Enlarged ribbon representation of boxed region 3 in C (I) or D (J); the N-terminal domain is colored in yellow, the DH-insert in orange, the central domain in green, the C-terminal domain in blue; one monomer of the dimer is colored in darker, the other in lighter shades; residues with 2<RMSF<3.8 Å (in-strand dimers) or 2<RMSF<4.8 Å (end-of-strand dimers) are highlighted in red. **(K,L)** same as I/J but helixes are represented by grey bars. The terminal regions of Helix H6, H26 and H27 that differ in position are colored in red (adapted from Schönegge et al., 2012 (A-J)).

2.2 Length Variations of TPPII spindles

2.2.1 Polymorphism of *Hs*TPPII spindles

Preparations of native *Hs*TPPII from human erythrocytes were not of sufficient quality to allow cryo-EM and 3D-reconstructions, therefore, no high resolution structure of native *Hs*TPPII could be obtained (see section 1.3.4). Still, electron micrographs of negatively stained particles could be recorded. The 2D-analysis of 12,950 particle images of native *Hs*TPPII revealed two classes of navette views – a longer and a shorter version (Schönegge et al., 2012); both class averages are shorter than the respective class average of *Dm*TPPII spindles (see Figure 18). As recombinant expression of oligomeric proteins can lead to polymorphism in homo-oligomeric proteins (Nitsch et al., 1997), a 2D-analysis of the 96,611 particle images of ice-embedded, recombinant *Hs*TPPII was performed. For both, native and recombinant *Hs*TPPII ~ 10% of the navette views fall into the class of the shorter spindles. Only a 3D-analysis can clarify whether this class represents a different projection of TPPII molecules rotated about their transverse axis or whether this class indicates the presence of two assembly states of *Hs*TPPII.

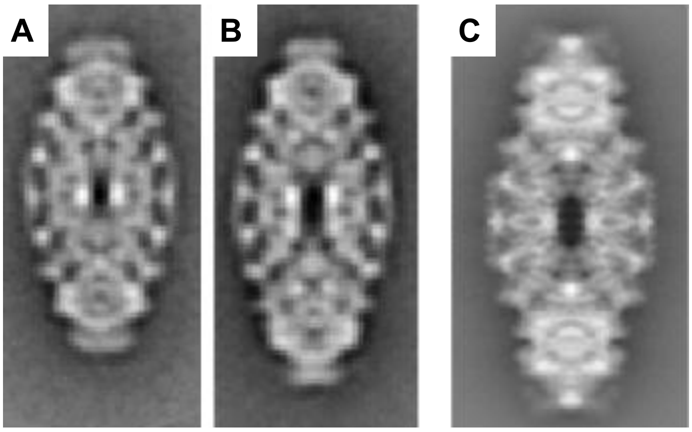

Figure 18: Polymorphism of TPPII spindles

(A-B) Class average of recombinant *Hs*TPPII in 'navette' orientation. **(C)** Projection of *Dm*TPPII in 'navette' orientation (adapted from Schönegge et al., 2012).

A 3D-variance analysis of the data set showed that the variance is restricted to the spindle poles (see Figure 19A/B), which indicates the existence of two spindle complexes differing in length. In order to separate the two assembly states, a 'maximum likelihood' approach (ML3D) was chosen. This procedure resembles the template matching procedure, but instead of one start reference several references are used. In addition, the discrete assignment of orientation and class (conventionally based on maximum cross-correlation) is replaced by probability-weighted integrals over all possible assignments. The iterative nature of the procedure leads to an increasing accuracy in assignments of both orientation and class (Scheres et al., 2007). For HsTPPII, three initial models were used (see Figure 19C) and the data set split into two classes with 9 segments per strand (HsTPPII$_9$) and one class with 8 segments per strands (HsTPPII$_8$; see Figure 19D). Each class contained about 1/3 of the particles and HsTPPII$_8$ and HsTPPII$_9$ were reconstructed separately (see Figure 19E/F). The resolution of both 3D-reconstructions was lower than the reconstruction including all particles (see Figure 19G).

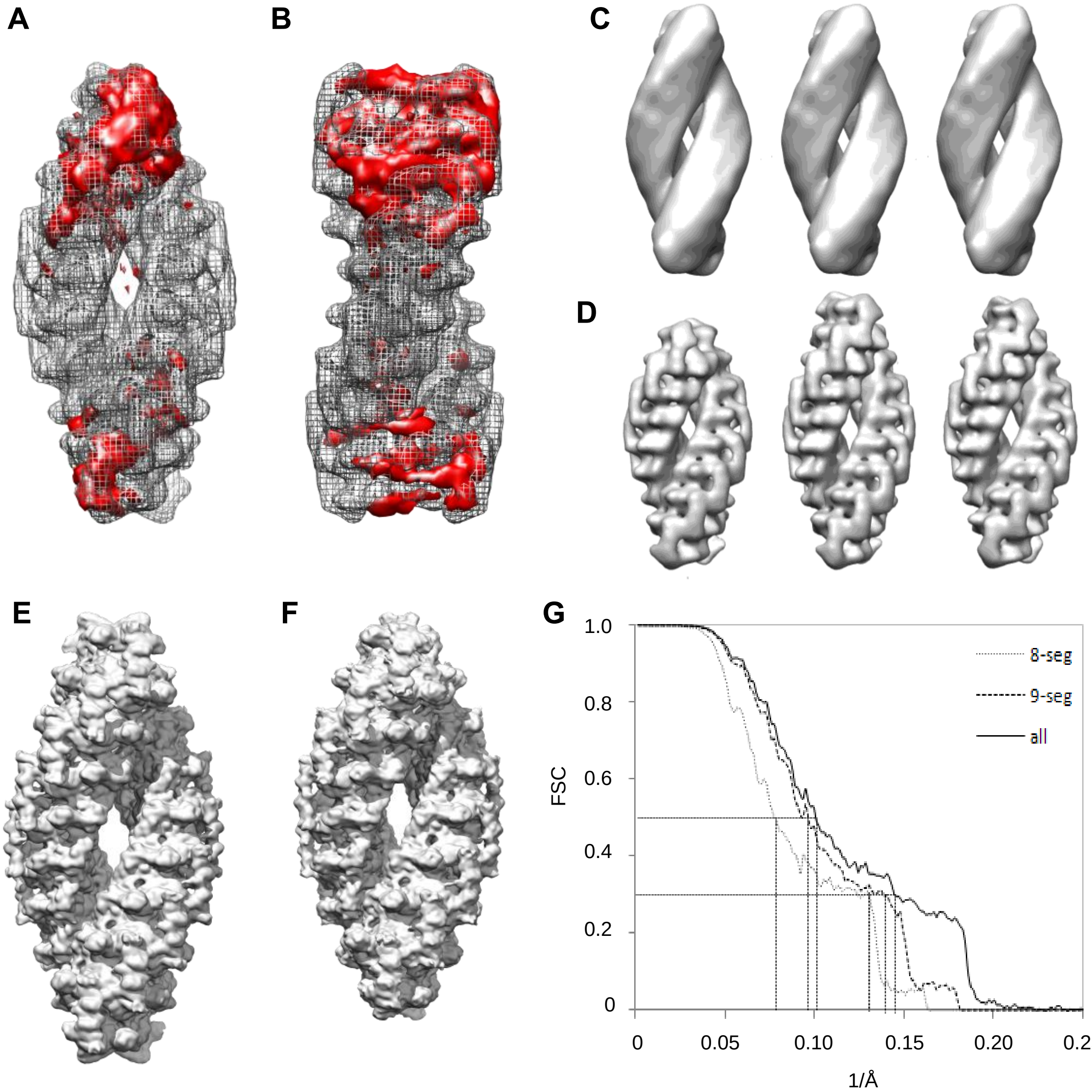

Figure 19: Separation and reconstruction of *Hs*TPPII spindles

(A-B) Variance map of the data set in navette (A) and dumbbell (B) view. Variance is shown in red. **(C)** Three initial models used for the ML3D analysis **(D)** Three classes after 21 iterations of ML3D. **(E)** Surface representation of *Hs*TPPII$_9$ (FSC$_{0.5}$ = 10.7 Å; FSC$_{0.3}$ = 8.0 Å). **(F)** Surface representation of *Hs*TPPII$_8$ (FSC$_{0.5}$ = 12.7 Å; FSC$_{0.3}$ = 8.1 Å). **(G)** Fourier shell correlation (FSC) of the 3D-reconstruction of all particles (solid line), *Hs*TPPII$_9$ (dashed line) and of *Hs*TPPII$_8$ (dotted line; adapted from Schönegge et al., 2012(A,B,E-G)).

2.2.2 Helix Parameters of TPPII Spindles

The existence of TPPII complexes differing in length indicates some variability in the dimer arrangement within TPPII spindles. In order to detect differences between *Hs*TPPII$_8$, *Hs*TPPII$_9$, and *Dm*TPPII, template matching with a low-pass filtered model of *Dm*TPPII was performed. The resulting positions and orientations of the dimers revealed – at good approximation – a helical arrangement of the dimers in each strand. A helix is characterized by a constant rise d and a constant screw angle β. When d and β were compared for the three spindle types, no significant differences could be detected (see Table 1). In all cases the helical rise d is ~52 Å and the helical screw angle β is ~25.6°. However, TPPII strands are no ideal helices, which become obvious when ideal and real positions of the dimers are compared (see Figure 20). While d is approximately constant in all cases, β is not (see Table 1). For *Dm*TPPII, β is smaller than the ideal β in the middle of the strand; whereas it is larger at the end of the strand (see Figure 20F). This effect is much less pronounced for both *Hs*TPPII spindles, where the real position of the dimers resembles their position in an ideal helix more closely (see Figure 20B/D).

	*Hs*TPPII$_8$	*Hs*TPPII$_9$	*Dm*TPPII
d	51.7±0.7Å	52.0±0.7Å	51.9±0.7Å
β	25.6±0.8°	25.4±0.9°	25.3±1.0°
α	16.0°	14.9°	11.1°
rot$_{total}$	179.2°	203.5°	228.1°

Table 1: Helix parameters of dimers in TPPII spindles

Helical parameters of the three different spindle types as analyzed by template matching of a low-pass filtered model of *Dm*TPPII in the different spindle types. d: helical rise; β: helical screw angle; α: tilt between two strands; rot$_{total}$: rotation from the first to the last dimer of a strand (adapted from Schönegge et al., 2012).

The total rotation between the first and the last dimer of the different spindles is 179.2° in *Hs*TPPII$_8$, 203.5° in *Hs*TPPII$_9$, and 236° in *Dm*TPPII (see Table 1). This stepwise increase of the total rotation reflects the elongation of the helix by one dimer. Irrespective of the number of dimers per strand the rotation between the minimum strand-strand distances at each spindle pole is always ~180° (Figure 20A/C/E). In order to form the spindle and to establish the stabilizing interactions at the spindle poles, the dimers of two strands need to be in close proximity and, therefore, the strands must be tilted against each other. Hence, their axes differ from the spindle axis by ±α/2 and intersect at the center of the spindle. The angle α between the two strands of a spindle is largest for *Hs*TPPII$_8$ and smallest for *Dm*TPPII (see Table 1; Figure 20A/C/E).

The helical model can be used to explain why TPPII spindles are composed of strands built of 8 to 10 dimers. A minimum of 8 dimers per strand is needed to establish a stable strand-strand interface. However, increasing length of the strands necessitates an increasing distance between the strands at the spindle poles, due to the tilt α between the helix axes. For simple geometrical reasons interactions between dimers of paired strands become impossible for strands longer than 10 dimers.

In conclusion, the arrangement of the dimers within a TPPII strand is approximately helical. The dimer-dimer interfaces are evidently only quasi-identical and allow a certain flexibility of the strands, which leads to the observed variations in strand lengths.

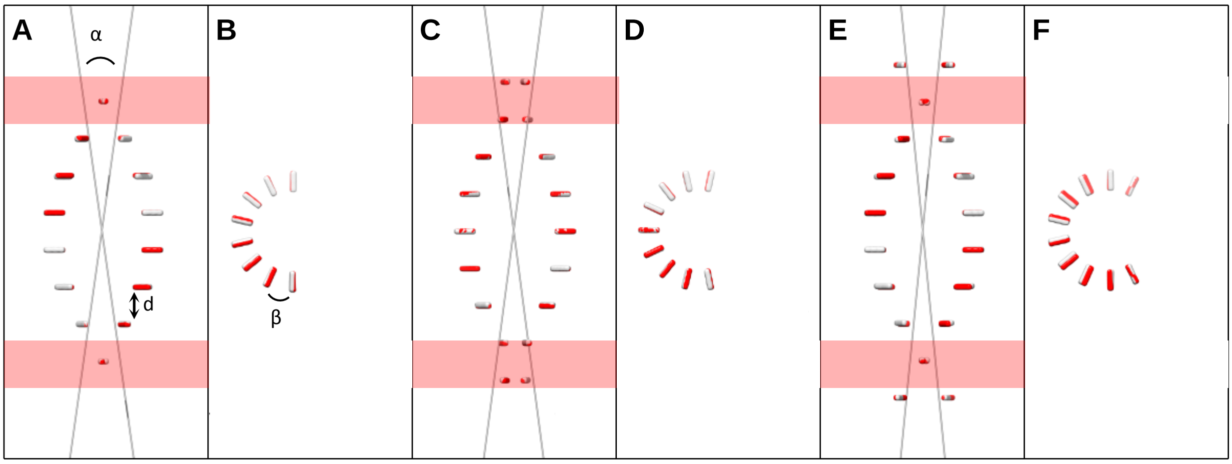

Figure 20: Positions of dimers in TPPII spindles

Positions of dimers in the three different spindle types analyzed by template matching of a low-pass filtered model of *Dm*TPPII in the different spindle types. Dimers are condensed to bars. The positions of dimers in the real spindle (gray) and in an ideal helix (red) are shown. **A/C/E)** Navette view of *Hs*TPPII$_8$ (A), *Hs*TPPII$_9$ (C) and *Dm*TPPII (E); red bars indicate the closest point between the strands. **B/D/F)** Single strand top view of *Hs*TPPII$_8$ (B), *Hs*TPPII$_9$ (D) and *Dm*TPPII (F) viewed along the helix axis. d: helical rise; β: helical screw angle; α: tilt between two strands (adapted from Schönegge et al., 2012).

2.2.3 Strand-Strand and Dimer-Dimer Interfaces

As shown above, the stacking parameters of the different spindle types are very similar. Still, the existence of different assembly states suggests differences in their strand-strand and dimer-dimer interfaces.

In order to analyze these interfaces atomic models are needed. Hybrid models for *Hs*TPPII$_8$ and *Hs*TPPII$_9$ were built by using the 3D-reconstructions, the comparative model of *Hs*TPPII and MDFF. Since the hybrid structure of *Dm*TPPII published recently was created by rigid body fitting and still contained clashes at the dimer-dimer interfaces (674 to 799 clashes between atoms; (Chuang et al., 2010), it was recalculated with MDFF. In this new model of *Dm*TPPII all steric clashes were resolved, the model conforms better to the EM-density of the holocomplex, and the dimer-dimer interfaces are more realistic.

Previously, the strand-strand interactions were described as spindle-stabilizing ‘double clamp’ established between the terminal two dimers of each strand (Rockel et al., 2005). The present analysis revealed that in fact only six of the eight monomers, which form the pair of terminal tetramers, participate in the strand-strand interactions. The two monomers with the largest distance to the spindle pole – monomer C and monomer G – do not contribute to the interactions (see Figure 21A/E). Most of the strand-strand interactions are established by contacts between monomer A and H, D and E, and B and F (see Table 2, Figure 21A/E). In *Dm*TPPII spindles and in *Hs*TPPII$_8$ spindles additional contacts between the monomer D and H, A and F, and B and E are observed. Due to the small sizes of their interaction areas, these additional contacts contribute only weakly to the strand-strand interface (see Table 2). All in all, the sizes of the strand-strand interaction areas in *Hs*TPPII$_8$ and *Hs*TPPII$_9$ spindles are very similar (see Table 2, Figure 21B-C). The small differences observed in the interaction areas might be caused by differences in fit-accuracy. The size of the strand-strand interaction area in the *Dm*TPPII spindle is more than three times as large as in both *Hs*TPPII spindles (see Table 2, Figure 21B-D).

	*Hs*TPPII$_8$	*Hs*TPPII$_9$	*Dm*TPPII
A-H	680 Å	421 Å	2091Å
D-E	737 Å	590 Å	1931 Å
B-F	86 Å	124 Å	1206 Å
D-H	X	x	195 Å
A-F	39 Å	x	11 Å
B-E	30 Å	x	9 Å
area$_{total}$	1571 Å	1134 Å	5444 Å

Table 2: Strand-strand interaction areas

Size of the monomer interactions involved in the strand-strand interface in the spindles of *Hs*TPPII$_8$, *Hs*TPPII$_9$ and *Dm*TPPII (adapted from Schönegge et al., 2012).

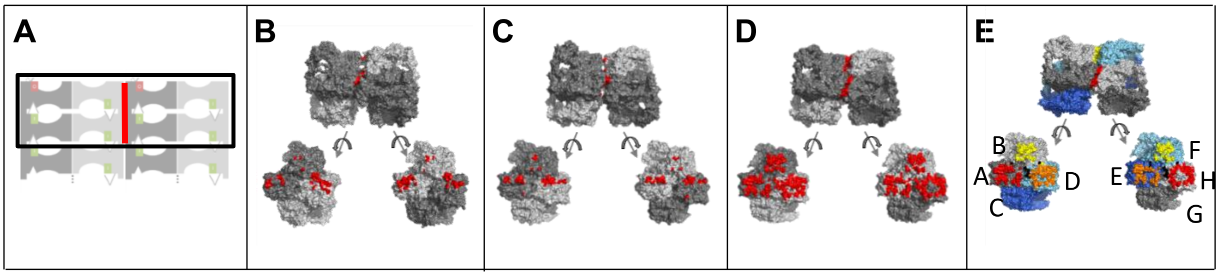

Figure 21: Strand-strand interaction areas

(A) Schematic representation of the spindle pole; the strand-strand interface is depicted as red line. **(B-D)** Terminal tetramers of *Hs*TPPII$_8$(B), *Hs*TPPII$_9$ (C) and *Dm*TPPII (D) as in the complex (middle) or rotated by +90°or -90° around the y-axis, respectively. **(E)** same as D; monomers are colored in dark and light blue or grey; monomers are labeled; monomer interactions are colored in red (A-H), orange (D-E) , yellow (B-F) or black (D-H,A-F,B-E).

In addition to the strand-strand interactions, the dimer-dimer interactions within one strand are important for complex formation. Within the strands of each spindle type the sizes of the dimer-dimer interaction areas differ only slightly (see Table 3). In all spindle types, the dimer-dimer interface is triangularly shaped and formed by contacts between monomer A and D, B and D, and A and C (see Figure 22A-E). The dimer-dimer interaction area for both *Hs*TPPII spindles is very similar (see Table 3). The overall dimer-dimer interaction area in *Dm*TPPII spindles is 1.5-times as large as in both *Hs*TPPII spindles (see Table 3, Figure 22B-D). In contrast to the strand-strand interface, where all monomer interaction areas are approximately three to ten times as large as in both *Hs*TPPII spindle types (see Table 2), in the dimer-dimer interface only the interaction area between monomer A and monomer D is approximately two-fold larger in *Dm*TPPII spindles than in both *Hs*TPPII spindles (see Table 3). This interaction area mainly involves the C-terminal domain, where most sequence differences between *Dm*TPPII and *Hs*TPPII are located.

	*Hs*TPPII$_8$	*Hs*TPPII$_9$	*Dm*TPPII
A-D	1168±78 Å	1691±105 Å	3267±115Å
B-D	1547±199 Å	1526±87 Å	1764±178 Å
A-C	1561±164 Å	1169±126 Å	1633±45 Å
area$_{total}$	4276±287 Å	4385±125 Å	6664±247 Å

Table 3: Dimer-dimer interaction areas

Size of the monomer interaction areas involved in the dimer-dimer interface in the spindle of *Hs*TPPII$_8$, *Hs*TPPII$_9$ and *Dm*TPPII (adapted from Schönegge et al., 2012).

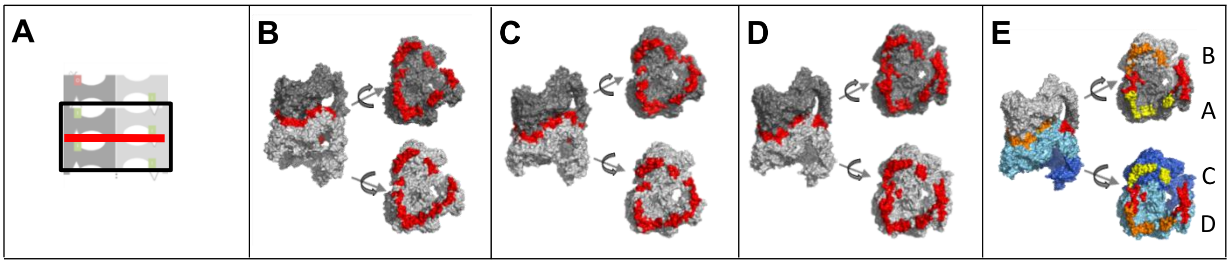

Figure 22: Dimer-dimer interaction areas

(A) Schematic representation of a TPPII strand, the dimer-dimer interaction is depicted as red line. **(B-D)** Dimers of *Hs*TPPII$_8$ (B), *Hs*TPPII$_9$ (C) and *Dm*TPPII (D) as in the complex (left) or rotated by +90°or -90° around the x-axis, respectively. The dimers are colored in dark and light grey; interacting areas are highlighted in red. **(E)** Same as D; monomers are colored on dark and light blue or grey; monomers are labeled; monomer interactions are colored in red (A-D), orange (B-D) or yellow (A-C).

The sizes of the strand-strand and dimer-dimer interaction area appear to vary from species to species and not to depend on the number of dimers per strand. For *Hs*TPPII hybrid structures of two spindles with different lengths are available. They only differ in number of dimers per strand and not in amino acid sequence. To detect possible differences between *Hs*TPPII$_8$ and *Hs*TPPII$_9$, the amino acids involved in dimer-dimer interactions in these spindles were highlighted in the *Hs*TPPII sequence. Only slight differences in the number and position of the amino acids involved in the interactions could be visualized (see Figure 23).

```
Hs9  MATAATEEPFPFHGLLPKKETGAASFLCRYPEYDGRGVLIAVLDTGVDPGAPGMQVTTDG  60
Hs8  MATAATEEPFPFHGLLPKKETGAASFLCRYPEYDGRGVLIAVLDTGVDPGAPGMQVTTDG  60

Hs9  KPKIVDIIDTTGSGDVNTATEVEPKDGEIVGLSGRVLKIPASWTNPSGKYHIGIKNGYDF  120
Hs8  KPKIVDIIDTTGSGDVNTATEVEPKDGEIVGLSGRVLKIPASWTNPSGKYHIGIKNGYDF  120

Hs9  YPKALKERIQKERKEKIWDPVHRVALAEACRKQEEFDVANNGSSQANKLIKEELQSQVEL  180
Hs8  YPKALKERIQKERKEKIWDPVHRVALAEACRKQEEFDVANNGSSQANKLIKEELQSQVEL  180

Hs9  LNSFEKKYSDPGPVYDCLVWHDGEVWRACIDSNEDGDLSKSTVLRNYKEAQEYGSFGTAE  240
Hs8  LNSFEKKYSDPGPVYDCLVWHDGEVWRACIDSNEDGDLSKSTVLRNYKEAQEYGSFGTAE  240

Hs9  MLNYSVNIYDDGNLLSIVTSGGAHGTHVASIAAGHFPEEPERNGVAPGAQILSIKIGDTR  300
Hs8  MLNYSVNIYDDGNLLSIVTSGGAHGTHVASIAAGHFPEEPERNGVAPGAQILSIKIGDTR  300

Hs9  LSTMETGTGLIRAMIEVINHKCDLVNYSYGEATHWPNSGRICEVINEAVWKHNIIYVSSA  360
Hs8  LSTMETGTGLIRAMIEVINHKCDLVNYSYGEATHWPNSGRICEVINEAVWKHNIIYVSSA  360

Hs9  GNNGPCLSTVGCPGGTTSSVIGVGAYVSPDMMVAEYSLREKLPANQYTWSSRGPSADGAL  420
Hs8  GNNGPCLSTVGCPGGTTSSVIGVGAYVSPDMMVAEYSLREKLPANQYTWSSRGPSADGAL  420

Hs9  GVSISAPGGAIASVPNWTLRGTQLMNGTSMSSPNACGGIALILSGLKANNIDYTVHSVRR  480
Hs8  GVSISAPGGAIASVPNWTLRGTQLMNGTSMSSPNACGGIALILSGLKANNIDYTVHSVRR  480

Hs9  ALENTAVKADNIEVFAQGHGIIQVDKAYDYLVQNTSFANKLGFTVTVGNNRGIYLRDPVQ  540
Hs8  ALENTAVKADNIEVFAQGHGIIQVDKAYDYLVQNTSFANKLGFTVTVGNNRGIYLRDPVQ  540

Hs9  VAAPSDHGVGIEPVFPENTENSEKISLQLHLALTSNSSWVQCPSHLELMNQCRHINIRVD  600
Hs8  VAAPSDHGVGIEPVFPENTENSEKISLQLHLALTSNSSWVQCPSHLELMNQCRHINIRVD  600

Hs9  PRGLREGLHYTEVCGYDIASPNAGPLFRVPITAVIAAKVNESSHYDLAFTDVHFKPGQIR  660
Hs8  PRGLREGLHYTEVCGYDIASPNAGPLFRVPITAVIAAKVNESSHYDLAFTDVHFKPGQIR  660

Hs9  RHFIEVPEGATWAEVTVCSCSSEVSAKFVLHAVQLVKQRAYRSHEFYKFCSLPEKGTLTE  720
Hs8  RHFIEVPEGATWAEVTVCSCSSEVSAKFVLHAVQLVKQRAYRSHEFYKFCSLPEKGTLTE  720

Hs9  AFPVLGGKAIEFCIARWWASLSDVNIDYTISFHGIVCTAPQLNIHASEGINRFDVQSSLK  780
Hs8  AFPVLGGKAIEFCIARWWASLSDVNIDYTISFHGIVCTAPQLNIHASEGINRFDVQSSLK  780

Hs9  YEDLAPCITLKNWVQTLRPVSAKTKPLGSRDVLPNNRQLYEMVLTYNFHQPKSGEVTPSC  840
Hs8  YEDLAPCITLKNWVQTLRPVSAKTKPLGSRDVLPNNRQLYEMVLTYNFHQPKSGEVTPSC  840

Hs9  PLLCELLYESEFDSQLWIIFDQNKRQMGSGDAYPHQYSLKLEKGDYTIRLQIRHEQISDL  900
Hs8  PLLCELLYESEFDSQLWIIFDQNKRQMGSGDAYPHQYSLKLEKGDYTIRLQIRHEQISDL  900

Hs9  ERLKDLPFIVSHRLSNTLSLDIHENHSFALLGKKKSSNLTLPPKYNQPFFVTSLPDDKIP  960
Hs8  ERLKDLPFIVSHRLSNTLSLDIHENHSFALLGKKKSSNLTLPPKYNQPFFVTSLPDDKIP  960

Hs9  KGAGPGCYLAGSLTLSKTELGKKADVIPVHYYLIPPPTKTKNGSKDKEKDSEKEKDLKEE  1020
Hs8  KGAGPGCYLAGSLTLSKTELGKKADVIPVHYYLIPPPTKTKNGSKDKEKDSEKEKDLKEE  1020

Hs9  FTEALRDLKIQWMTKLDSSDIYNELKETYPNYLPLYVARLHQLDAEKERMKRLNEIVDAA  1080
Hs8  FTEALRDLKIQWMTKLDSSDIYNELKETYPNYLPLYVARLHQLDAEKERMKRLNEIVDAA  1080

Hs9  NAVISHIDQTALAVYIAMKTDPRPDAATIKNDMDKQKSTLVDALCRKGCALADHLLHTQA  1140
Hs8  NAVISHIDQTALAVYIAMKTDPRPDAATIKNDMDKQKSTLVDALCRKGCALADHLLHTQA  1140

Hs9  QDGAISTDAEGKEEEGESPLDSLAETFWETTKWTDLFDNKVLTFAYKHALVNKMYGRGLK  1200
Hs8  QDGAISTDAEGKEEEGESPLDSLAETFWETTKWTDLFDNKVLTFAYKHALVNKMYGRGLK  1200

Hs9  FATKLVEEKPTKENWKNCIQLMKLLGWTHCASFTENWLPIMYPPDYCVF  1249
Hs8  FATKLVEEKPTKENWKNCIQLMKLLGWTHCASFTENWLPIMYPPDYCVF  1249
```

Figure 23: Residues at the dimer-dimer interface of short and long *Hs*TPPII spindles

Residues located at the dimer-dimer interface were highlighted in the sequence of *Hs*TPPII and compared between *Hs*TPPII$_9$ and *Hs*TPPII$_8$; the N-terminal domain is colored in yellow, the DH-insert in orange, the central domain in green, the C-terminal domain in blue. Grey: interacting aa; red font: flexible aa; underlined: H5, H6, H26 and H27; underlined in bold: loop L2 and loop L1 (adapted from Schönegge et al., 2012).

2.3 Structural Elements in TPPII Activation

Based on the hybrid structure of *Dm*TPPII an activation model for TPPII was proposed (Chuang et al., 2010). According to this model, the activation process consists of two main steps that are interlinked: i) the positioning of the active-site serine in a catalytically active conformation and ii) the removal of loop L2 from the active-site cleft. In order to get a deeper insight into TPPII-activation, some structural elements, which are supposed to participate in the activation process, were inspected in respect to their conformation and position in the hybrid structure.

2.3.1 *Dm*TPPII-Subtilisin Chimeras

The activation model of TPPII postulates that during the activation process the active-site region (loop L2 and helix H9) of *Dm*TPPII adopts a conformation and hydrogen bond network similar to that in subtilisin (Chuang et al., 2010). To test whether these rearrangements of loop L2 are sufficient to activate TPPII dimers, loop L2 of *Dm*TPPII was adapted to loop 'L' of subtilisin by mutation. For this purpose, two residues (P448, QY449) were deleted and V447 was changed to Thr and T451 to Pro (see Figure 24A). However, both mutants had no detectable activity in the *E. coli* lysate (see Figure 24B). Electron micrographs of the high molecular weight (HMW) Superpose 6 fraction (8.1 ml, elution volume corresponding to the spindle complex) indicated that these mutations interfered with the assembly of TPPII: no spindle complexes but only single strands were observed (see Figure 24C). Apparently, the mutations designed to render loop L2 of *Dm*TPPII subtilisin-like were not sufficient to establish a subtilisin-like conformation of loop L2. Next, loop L2 and helix H9 were replaced by the corresponding regions of subtilisin both separately and in combination (loop L2 vs. loop 'L', helix H9 vs. helix hF, and loop L2 + helix H9 vs. loop 'L' + helix hF). All three mutations, however, abolished the activity of TPPII (see Figure 24B). The inspection of the HMW complex in the respective Superpose 6 fraction by EM showed that none of the mutants assembled into spindles but all of them formed single strands (see Figure 24C).

In conclusion, the introduction of the structural elements loop 'L' and helix hF from subtilisin into *Dm*TPPII is not sufficient to generate active TPPII dimers. Possibly, helix hF and loop 'L' cannot adopt their native conformation within TPPII or TPPII undergoes a complex activation process involving more than these two structural elements. Both scenarios would impede the activation of TPPII dimers.

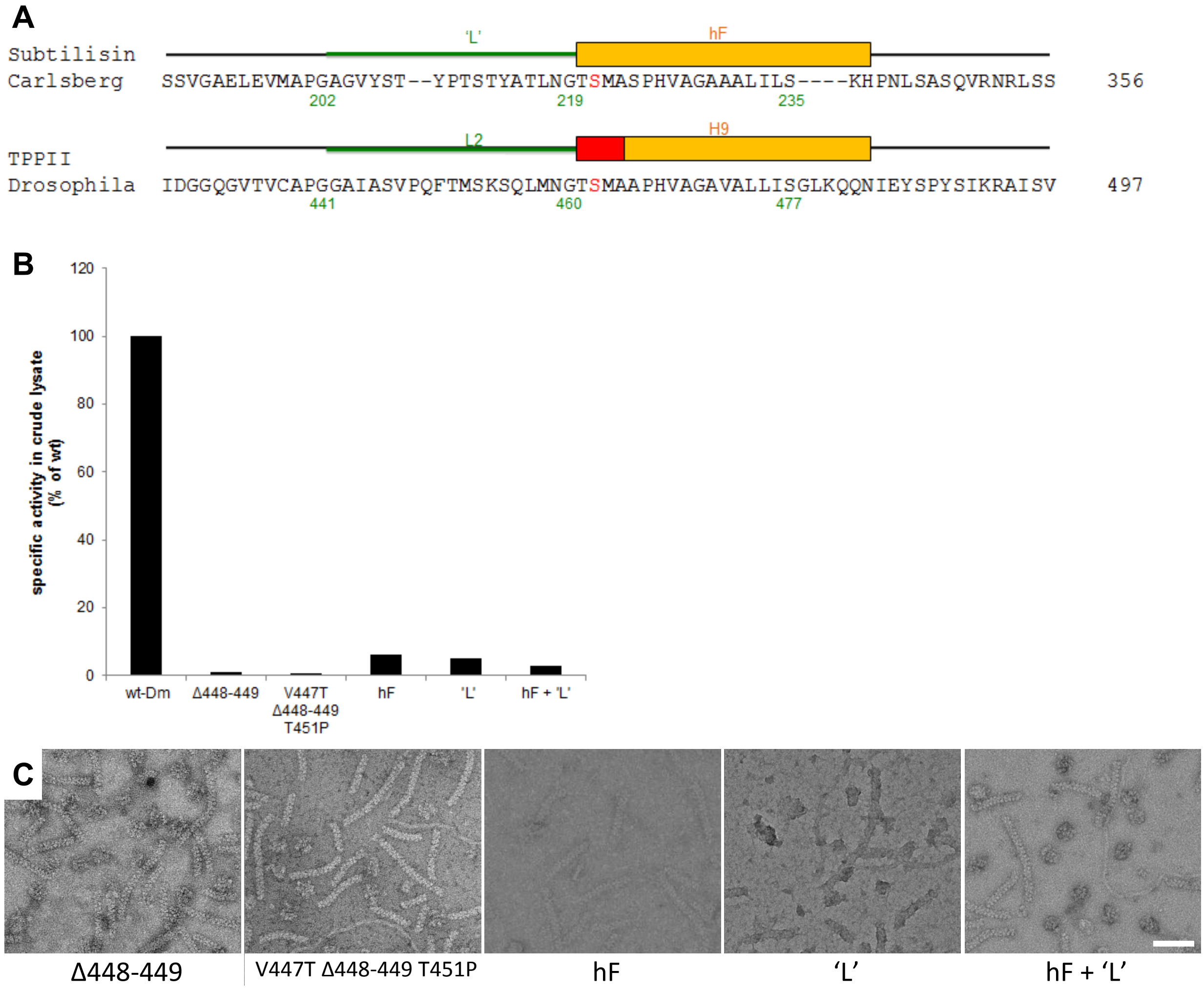

Figure 24: *Dm*TPPII-subtilisin chimeras

(A) Partial sequences of subtilisin Carlsberg and *Dm*TPPII, the orange box indicates the location of the α–helix connected to the active-site serine. The red box on the left side of the rectangle marks the unwound N–terminal region of helix H9 in the *Dm*TPPII dimer structure. Active-site serine residues of subtilisin and *Dm*TPPII are shown in red. Loop L2 and the equivalent loop 'L' are represented by a green line. Numbers below the sequence denote amino acid positions in the sequence. **(B)** Diagram of the specific activity of the *Dm*TPPII-subtilisin chimeras in crude lysate. The specific activity relates to the total amount of protein in the lysate. **(C)** Electron micrographs of the HMW fraction of *Dm*TPPII-subtilisin chimeras. Scale bar: 100 nm.

2.3.2 Helix H13

In subtilisin, the active-site serine is located within the N-terminal last turn of an α-helix (hF). In *Dm*TPPII, the corresponding α-helix (H9) is shorter by one turn, since the sequence stretch T461 - A464 is not part of the helix. In the 'short' conformation of helix H9 the active-site serine (S462) is not part of the α-helix and displaced by 5 Å. Since the amino acids in the 'unwound' region (T461 - A464 in *Dm*TPPII) are conserved between the TPPII and subtilisin families (see Figure 26), it was postulates that during activation the unwound region assumes α-helical conformation.

In the comparative model of *Hs*TPPII the position of the active-site serine resembles that of *Dm*TPPII, which was used as template: the active-site serine is displaced and the helix (H13) is in the 'short' conformation. The active conformation of *Hs*TPPII was modeled during MDFF by simulating the orientations and positions of the active-site residues according to those in subtilisin. The application of such distance restraints to the active-site residues elongated the helix H13 by one turn.

In the 3D-map of *Hs*TPPII spindles, a density for helix H13 is visible in some but not in all dimers, which might be due to the limited resolution of 3D-map (see Figure 25A-C). Where visible, this density encloses both helix H13 plus T448 to S451 (corresponding to T461 to A464 in *Dm*TPPII). To interpret this region independently of the flexibly fitted models, the crystal structures of *Dm*TPPII and subtilisin were aligned to the respective position. Both helix hF of subtilisin and helix H9 plus T461-A464 of *Dm*TPPII can be fully accommodated by the density corresponding to helix H13 (see Figure 25D/E).

However, a density corresponding to the elongated helix H13 is not visible in all dimers in the EM-map, either because the quality of the 3D-map does not allow a clear assignment for each dimer or because not all dimers in the spindle are activated.

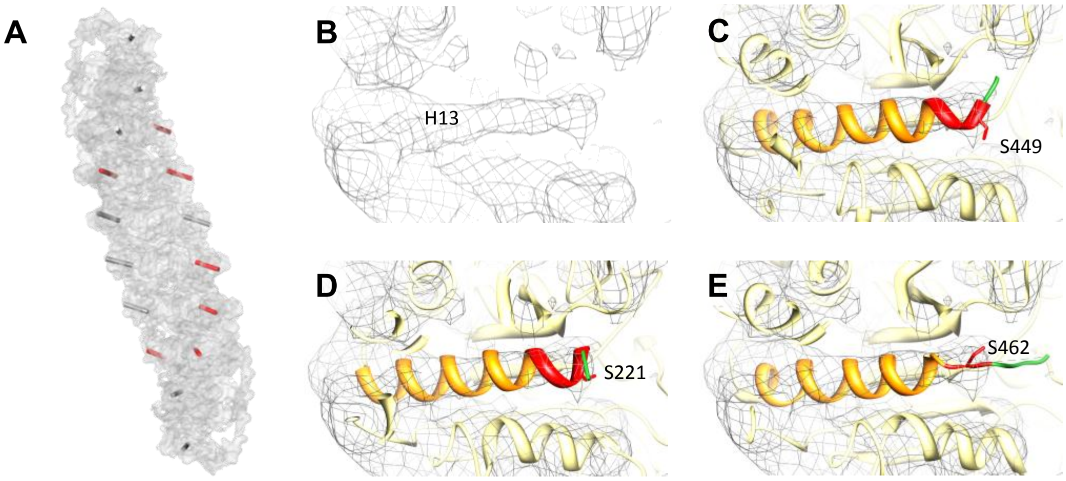

Figure 25: Conformation of helix H13

(A) 3D-density of one strand of *Hs*TPPII; the position of H13 in each dimer is indicated by tubes; in dimers with an elongated density for H13 the tube is colored red. **(B)** Density corresponding to helix H13 in the 3D-map of HsTPPII. **(C)** B with docked comparative model. **(D)** B with docked subtilisin (PDB ID: 1CSE). **(E)** B with docked DmTPPII (PDB ID: 3LXU). L2/'L' is colored green; H13/hF in orange; T448-S451 (and corresponding residues) in red (adapted from Schönegge et al., 2012 (B-E)).

2.3.3 Loop L2

In the amino acid sequence of TPPII loop L2 precedes the active-site serine (see Figure 26). Due to the proposed high flexibility only three C-terminal amino acids of loop L2 are visible in the crystal structure of TPPII dimers. These residues are bound to the active-site cleft from where they need to be removed during the activation of TPPII. In subtilisin, the loop ‘L’ is directly linked to the active-site serine and it makes a tight turn onto itself, forming many anti-parallel β-sheet hydrogen bonds. The sequences of the loop L2 and the loop ‘L’ are quite different but are conserved in their respective families (see Figure 26). It was postulated that in the activated state of TPPII a hydrogen bond network similar to the one in subtilisin is established in loop L2 (Chuang et al., 2010).

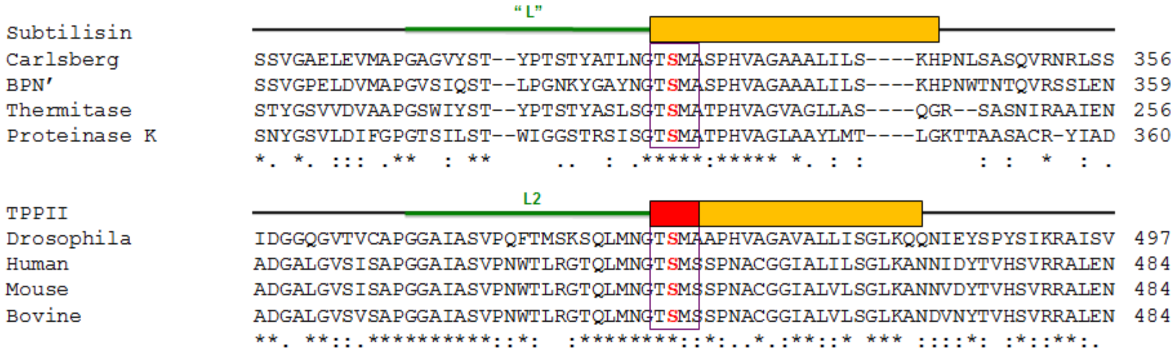

```
Subtilisin
Carlsberg       SSVGAELEVMAPGAGVYST--YPTSTYATLNGTSMASPHVAGAAALILS----KHPNLSASQVRNRLSS  356
BPN’            SSVGPELDVMAPGVSIQST--LPGNKYGAYNGTSMASPHVAGAAALILS----KHPNWTNTQVRSSLEN  359
Thermitase      STYGSVVDVAAPGSWIYST--YPTSTYASLSGTSMATPHVAGVAGLLAS----QGR--SASNIRAAIEN  256
Proteinase K    SNYGSVLDIFGPGTSILST--WIGGSTRSISGTSMATPHVAGLAAYLMT----LGKTTAASACR-YIAD  360
                *. *. ::: .**  : **     ..  : .*****:***** *. : :         : :  *  : .

TPPII
Drosophila      IDGGQGVTVCAPGGAIASVPQFTMSKSQLMNGTSMAAPHVAGAVALLISGLKQQNIEYSPYSIKRAISV  497
Human           ADGALGVSISAPGGAIASVPNWTLRGTQLMNGTSMSSPNACGGIALILSGLKANNIDYTVHSVRRALEN  484
Mouse           ADGALGVSISAPGGAIASVPNWTLRGTQLMNGTSMSSPNACGGIALVLSGLKANNVDYTVHSVRRALEN  484
Bovine          ADGALGVSVSAPGGAIASVPNWTLRGTQLMNGTSMSSPNACGGIALVLSGLKANDVNYTVHSVRRALEN  484
                **. **::.**********::*:  :********::*:..*.:**::* *** ::::*: :*::**:.
```

Figure 26: Sequence alignment in the region of loop L2

Aligned subtilisin and TPPII sequences; the orange box indicates the location of the α–helix connected to the active-site serine. The red box marks the unwound N–terminal region of helix H9 in the *Dm*TPPII dimer structure. The amino acid sequence of this region (boxed in purple) is highly conserved in both subtilisin and TPP II families. Active–site serine residues of subtilisin and TPP II family members are shown in red letters. Loop L2 and the equivalent loop ‘L’ are represented by a green line.

The sequence alignment of several TPPII family members (see Figure 26) shows that the sequence of loop L2 is highly conserved between *Dm*TPPII and its mammalian relatives. Thus, it is likely that loop L2 has a similar conformation in all TPPII variants and its position in *Hs*TPPII spindles is the same as in *Dm*TPPII spindles (similar to loop ‘L’ in subtilisin).

Superimposition of helix hF and loop ‘L’ of subtilisin with the corresponding region in the EM-map of *Hs*TPPII spindles revealed a density at the dimer-dimer interface that can accommodate loop ‘L’ (see Figure 27A/B). In contrast to the crystal structure of *Dm*TPPII, the comparative model of *Hs*TPPII contains loop L2 and it is suggestive that in the hybrid structure the N-terminal part of loop L2 resides in the same density as loop ‘L’ (see Figure

27A/C). However, the conformations of the loops L2 and ‘L’ differ significantly (see Figure 27B/C).

For *Dm*TPPII, the acceptor region of loop L2 is supposed to be at the roof of the catalytic chamber and includes residues L603 to R610 of the neighboring dimer (Chuang et al., 2010). The corresponding region in *Hs*TPPII comprises the residues L586 to R593. Since the analysis of the close proximity around residues provides an indication about potential interactions partners, residues in a distance of max. 5 Å of loop L2 were identified. Two regions of the neighboring dimer supposedly interact with loop L2: M589 to R593 and E563 to S566.

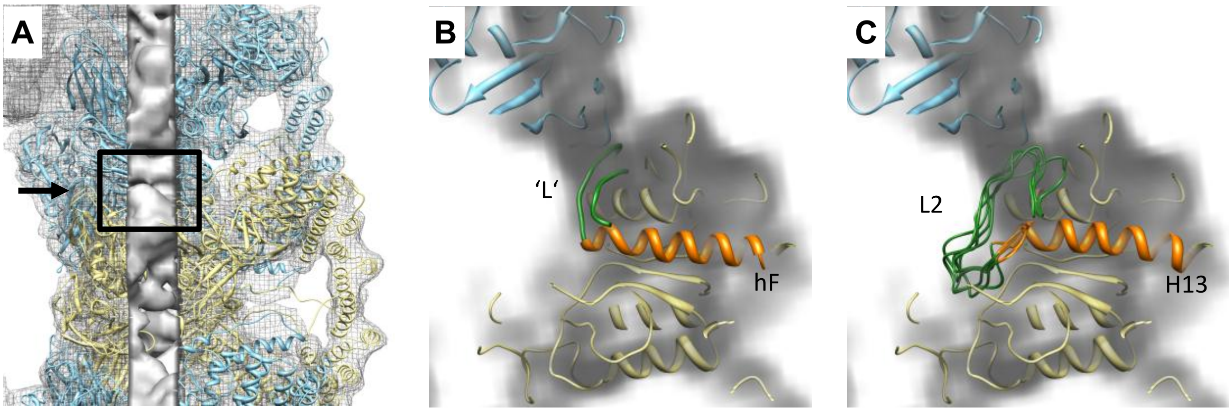

Figure 27: Loop L2 at the dimer-dimer interface

(A) Flexibly fitted TPPII dimers shown in light blue and light yellow; a portion of the 3D-map of *Hs*TPPII spindles is shown in mesh. The slice of the 3D-map in surface representation contains L2. **(B)** Orthogonal view of the box in A; The dimer-dimer interface with two flexibly fitted dimers of *Hs*TPPII with helix hF and loop ‘L’ of subtilisin replacing helix H13 and loop L2. **(C)** Same as B only helix H13 and an ensemble of five superimposed loop L2 conformations are shown. Dimers are colored in light blue or yellow; L2/’L’ in green; H13/hF in orange (adapted from Schönegge et al., 2012 (B,C)).

2.3.4 Loop L1

Loop L1 is located on the N-terminal side of loop L2 in the TPPII sequence and like loop L2 it is situated close to the active-site and is not resolved in the crystal structure of *Dm*TPPII (Chuang et al., 2010). It is not present in the subtilisin family and it is unique and conserved in the TPPII family (see Figure 28). The analysis of the dimer-dimer interaction area revealed that both loop L1 and loop L2 interact with the neighboring dimer (see Figure 23; section 2.2.3). Based on its location and its uniqueness for TPPII, it is hypothesized that loop L1 also participates in the activation mechanism of TPPII.

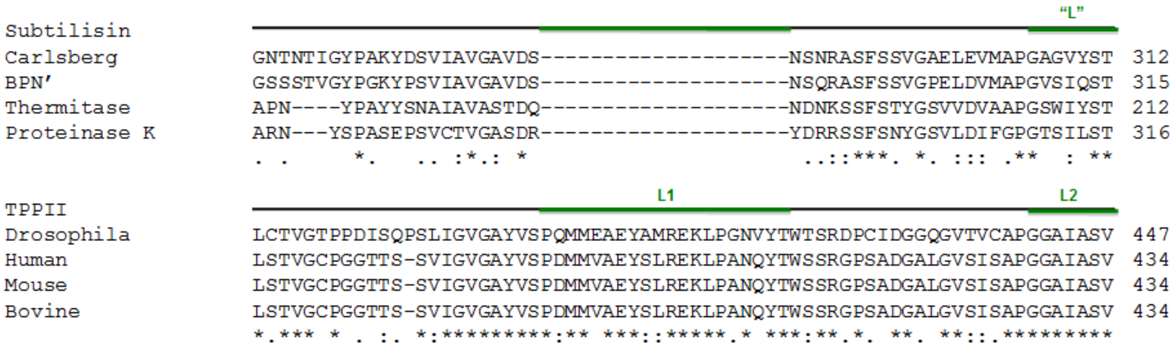

```
Subtilisin
Carlsberg       GNTNTIGYPAKYDSVIAVGAVDS--------------------NSNRASFSSVGAELEVMAPGAGVYST 312
BPN'            GSSSTVGYPGKYPSVIAVGAVDS--------------------NSQRASFSSVGPELDVMAPGVSIQST 315
Thermitase      APN----YPAYYSNAIAVASTDQ--------------------NDNKSSFSTYGSVVDVAAPGSWIYST 212
Proteinase K    ARN---YSPASEPSVCTVGASDR--------------------YDRRSSFSNYGSVLDIFGPGTSILST 316
                . .     *.   .. :*.: *                      ..::***. *. ::: .**  : **

TPPII
Drosophila      LCTVGTPPDISQPSLIGVGAYVSPQMMEAEYAMREKLPGNVYTWTSRDPCIDGGQGVTVCAPGGAIASV 447
Human           LSTVGCPGGTTS-SVIGVGAYVSPDMMVAEYSLREKLPANQYTWSSRGPSADGALGVSISAPGGAIASV 434
Mouse           LSTVGCPGGTTS-SVIGVGAYVSPDMMVAEYSLREKLPANQYTWSSRGPSADGALGVSISAPGGAIASV 434
Bovine          LSTVGCPGGTTS-SVIGVGAYVSPDMMVAEYSLREKLPANQYTWSSRGPSADGALGVSISAPGGAIASV 434
                *.*** * . :. *:*********:** ***::*****.* ***:**.*. **. **::.*********
```

Figure 28: Sequence alignment in the region of loop L1

Aligned subtilisin and TPPII sequences; loop L1 and the N-terminal parts of loop L2 and loop 'L' are represented by green lines.

To get a hint at the location of loop L1 in the TPPII spindle, we inspected the dimer-dimer interface of the hybrid structure of *Hs*TPPII (see Figure 29A/B). Loop L1 was found to be located within a strong density in the 3D-map at the dimer-dimer interface (see Figure 29A/C). In order to examine whether this density could correspond to loop L1, subtilisin, which lacks this loop, was superimposed to the corresponding region in the EM-map of *Hs*TPPII. Indeed, the density that harbored loop L1 is not accounted for by the atomic model of subtilisin (see Figure 29A/B). This observation supports the proposed position of loop L1 at the dimer-dimer interface.

As the analysis of the dimer-dimer interface showed that loop L1 might interact with the neighboring dimer, residues with a maximum distance of 5 Å were identified. Residues Q581 to R598 of the neighboring dimer are in close proximity to loop L1 and, therefore, might interact with loop L1. Interestingly, this region partially overlaps with the proposed interaction regions of loop L2. According to this analysis, also the C- and N-terminal ends of loop L1 (S388 - M392 and N405, Q406) and loop L2 (G428, A430, I431 and N435 to T438) are in immediate vicinity, which suggests that the two loops also interact.

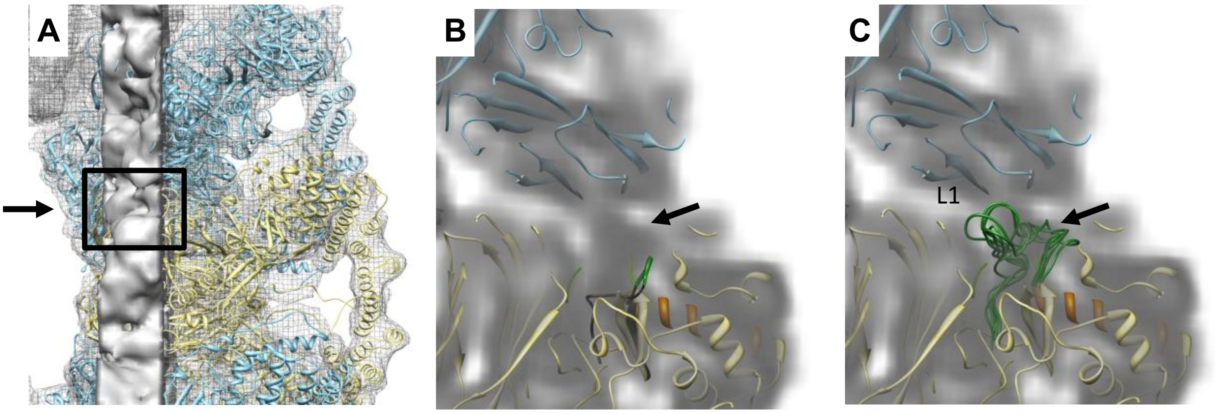

Figure 29: Loop L1 at the dimer-dimer interface

(A) Flexibly fitted dimers shown in light blue and light orange; the 3D-map is shown in mesh. The slice of the 3D-map in surface representation contains loop L1. **(B)** Orthogonal view of the box in A; the dimer-dimer interface with two flexibly fitted dimers of *Hs*TPPII with the corresponding region of loop L1 of subtilisin (black arrow). **(C)** Same as B only the superimposed loops L1 are shown (black arrow). Dimers are colored in light blue or yellow; L1 in green; H13/hF in orange.

2.4 Mutational Analysis of the Dimer-Dimer Interactions

As shown in the present and in other studies, the native conformation of the dimer-dimer interface is important for both assembly and activity of TPPII (Chuang et al., 2010; Seyit et al., 2006; Tomkinson, 2000). So far no information about the nature of the dimer-dimer interactions is available. The activation model proposes interactions between loop L2 and its acceptor region that are functionally relevant (Chuang et al., 2010). The data presented above (see section 2.3.3 and 2.3.4) supports the idea of the localization and participation of loop L2 at dimer-dimer interactions in the spindle complex and indicates that loop L1 also takes part in these interactions. In order to get a clue about the exact roles of loop L2 and loop L1 in the activation process, a mutational analysis of sequence stretches putatively involved in dimer-dimer interactions and in the activation process was performed. All mutations introduced were designed to abolish specific interactions: i) deletion of the whole loop regions to exam their importance, and ii) systematic exchange of single amino acids for alanine (Ala-screen) to identify single interaction pairs.

2.4.1 Loop L2

The deletion of loop L2 (ΔG442-N459) in *Dm*TPPII strongly decreased the specific activity in crude lysate of *E. coli* cells expressing the mutated TPPII (see Figure 30A-C). In order to examine whether the mutation also affected the morphology of the TPPII complex, the protein was purified by SEC as final step and the high molecular weight (HMW) fraction (8.1 ml; elution volume corresponding to the spindle complex) was scrutinized by EM. In the HMW fraction of ΔL2*Dm*TPPII only single strands but no spindle complex was observed (see Figure 31).

In order to investigate which residue of loop L2 is critical for TPPII activation, an Ala-screen was performed. The exchange of each amino acid to alanine had various effects on activity (see Figure 30A-C) and assembly (see Figure 31) of TPPII and, according to these effects, the mutants were classified in four groups: i) mutants that form spindles and show more than 50% specific activity (in figures: **A**), ii) mutants that form spindles and show less than 50% specific activity (in figures: **A**), iii) mutants that form single strands only and show more than 50% specific activity (in figures: **N**), and iv) mutants that form single strands only and show less than 50% specific activity (in figures: **N**).

Of the thirteen mutants of the Ala-screen three fell into goup i, two into group ii, two into group iii, and seven into group iv (see Figure 30A-D and Figure 31).

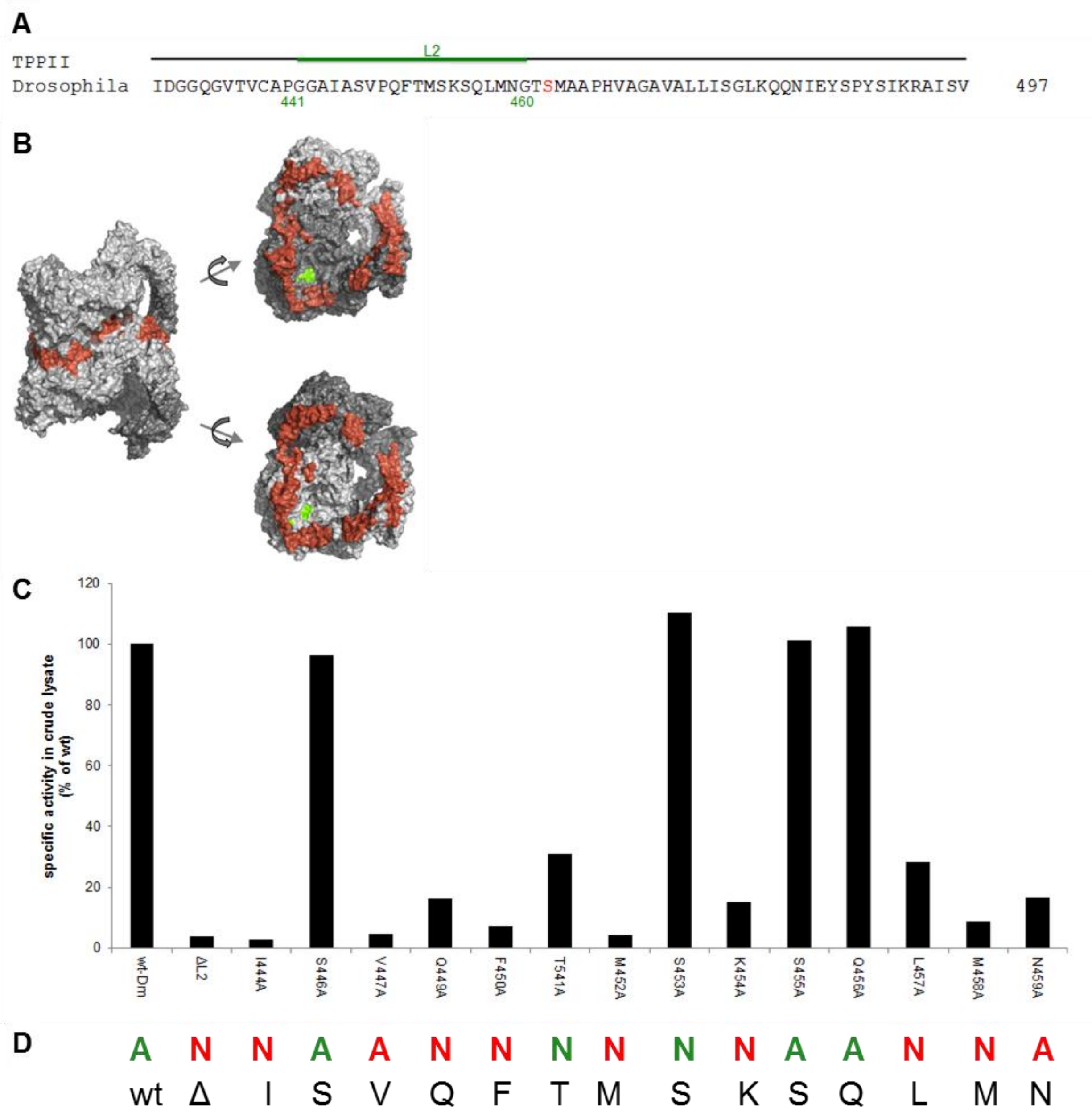

Figure 30: L2-*Dm*TPPII mutants

(A) Partial sequence of the *Dm*TPPII; the active-site serine residue is shown in red. Loop L2 is represented by a green line. Numbers below the sequence denote amino acid positions in the TPPII sequence. **(B)** Surface model of *Dm*TPPII dimers as in the complex (left) or rotated by +90°or -90° around the x-axis, respectively. The monomers are colored in dark and light grey; interacting areas are highlighted in red. Residues G441 to G460 are colored in green. Note: residues G442 to Q456 are missing in the surface model. **(C)** Specific activity of the L2-*Dm*TPPII mutants in crude lysate. The specific activity relates to the total amount of protein in the lysate. **(D)** Effects of the mutations in loop L2 of *Dm*TPPII; A: assembly into spindles; N: no assembly into spindles, but into single strands only; red font: specific activity in crude lysate <50% of wild-type protein; green font: specific activity in crude lysate >50% of wild-type protein.

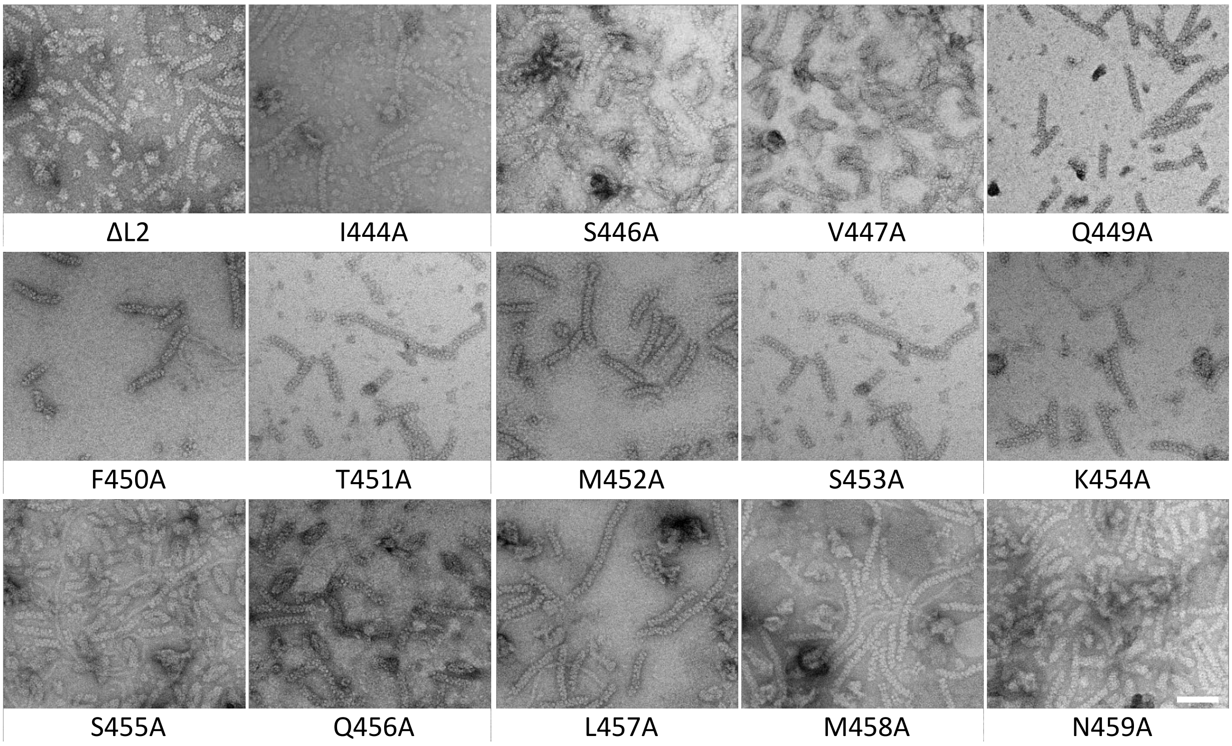

Figure 31: Electron micrographs of L2-*Dm*TPPII mutants

Electron micrographs of negatively stained particles in the HMW fraction of purified L2-*Dm*TPPII mutants. Scale bar: 100 nm.

The deletion of loop L2 (ΔG429-N446) in *Hs*TPPII had the same effects as its deletion in *Dm*TPPII: the specific activity in the lysate was strongly reduced (see Figure 32A-C) and the mutant assembled into single strands only (see Figure 33).

Similar to the Ala-screen in *Dm*TPPII, the effects of the Ala-screen in *Hs*TPPII were diverse and the mutants were classified into the same groups. Of the thirteen mutants, three mutants fell into group i, one into group ii, three into group iii, and seven mutants into group iv (see Figure 32A-D and Figure 33).

In SEC of the mutant *Hs*TPPII proteins not only a peak at high apparent molecular mass but also a peak at low apparent molecular weight was observed (data not shown). The specific activity of the HMW fraction (8.1 ml; elution volume corresponding to the spindle complex) and low molecular weight (LMW) fraction (14.9 ml; elution volume corresponding to the dimer/tetramer) was determined, to examine whether the mutations affected the specific activity of these complex. In all mutations, the specific activity in the crude lysate, the HMW fraction and the LMW fraction is reduced to approximately the same extend (see Figure 32A-C).

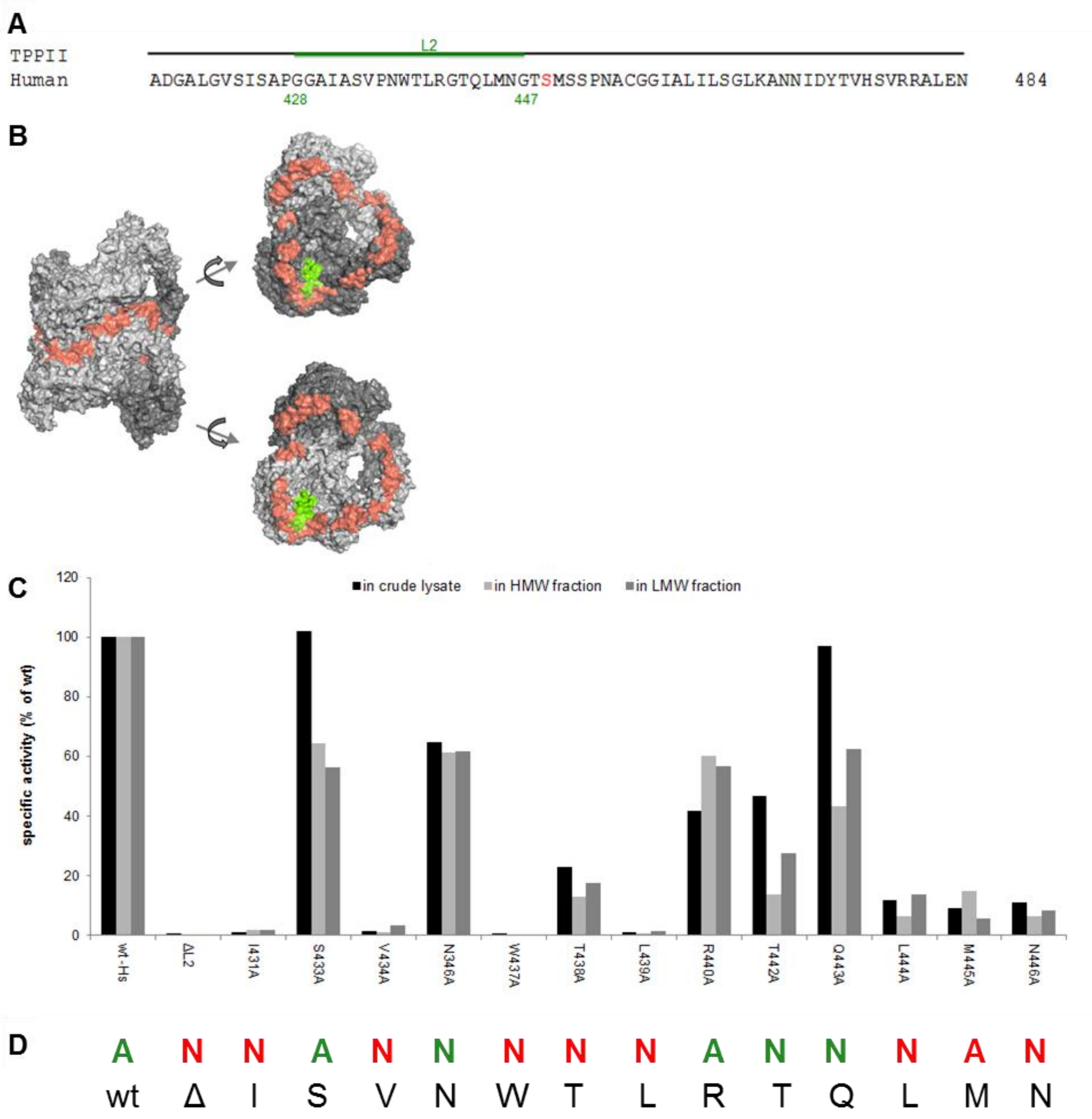

Figure 32: L2-*Hs*TPPII mutants

(A) Partial sequence of *Hs*TPPII; active-site serine residue of *Hs*TPPII is shown in red. Loop L2 is represented by a green line. Numbers below the sequence denote amino acid positions in the TPPII sequence. **(B)** Surface model of *Hs*TPPII dimers as in the complex (left) or rotated by +90°or -90° around the x-axis, respectively. The monomers are colored in dark and light grey; interacting areas are highlighted in red. Residues G428 to G447 are colored in green. **(C)** Specific activities of the L2-*Hs*TPPII mutants. The specific activity in the crude lysate relates to the total amount of protein in the lysate. The specific activity of the HMW and LMW fractions relates to the amount of TPPII in the fractions. Note: in absolute terms the specific activity of the wild-type LMW fraction is ~ 10% of the wild-type HMW fraction. **(D)** Effects of the mutations in loop L2 of *Hs*TPPII; A: assembly into spindles; N: no assembly into spindles, but into single strands only; red font: specific activity in crude lysate <50% of wild-type protein; green font: specific activity in crude lysate >50% of wild-type protein.

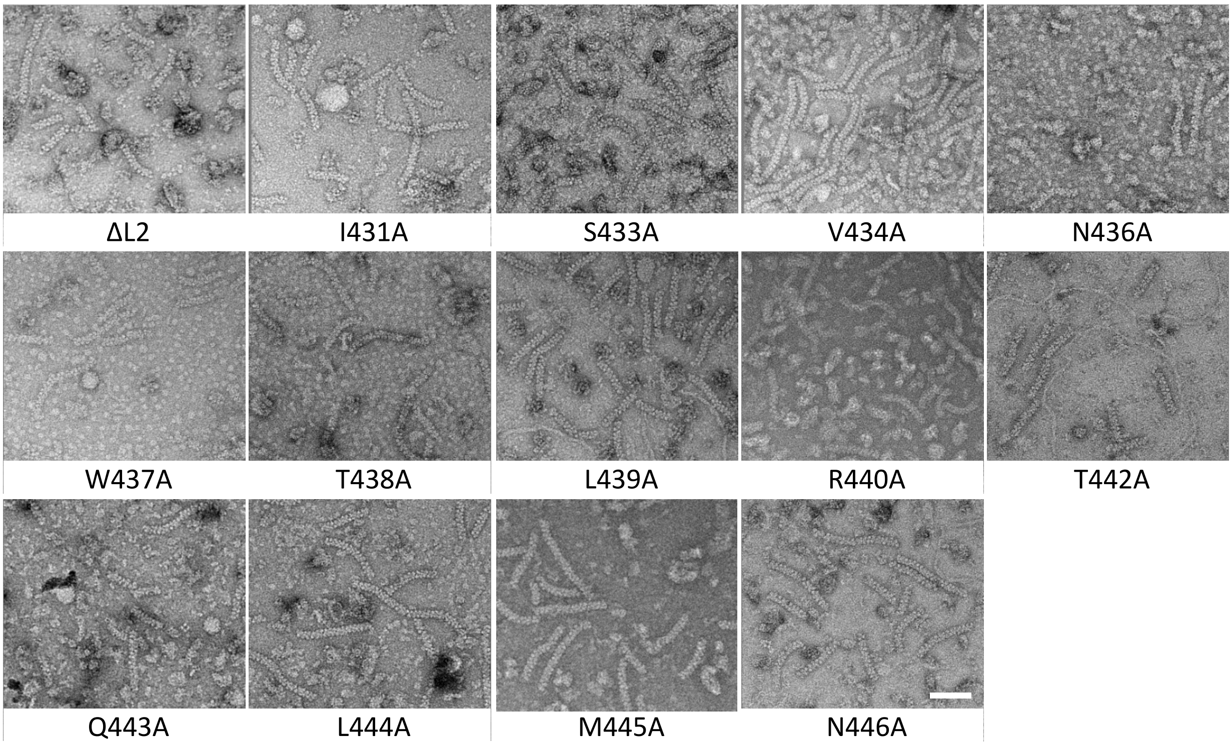

Figure 33: Electron micrographs of L2-*Hs*TPPII mutants

Electron micrographs of negatively stained particles in the HMW fraction of purified L2-*Hs*TPPII mutants. Scale bar: 100 nm.

In summary, the results of the mutational analysis of loop L2 indicate that the native interactions of loop L2 with its acceptor region is crucial for the assembly and activity of TPPII. It seems that assembly and activation of the TPPII complex are affected by single amino acid changes in loop L2. This observation suggests that the conformation of loop L2 is sensitive to these changes and that, in turn, assembly and activation of the TPPII are sensitive to the conformation of loop L2.

2.4.2 Loop L1

The deletion of loop L1 (ΔP402-P416) in *Dm*TPPII reduced the specific activity in *E. coli* crude lysate significantly (see Figure 34A-C). To analyze the assembly of this deletion mutant, the protein was partly purified and the complex in the HMW fraction was inspected by EM. In the HMW fraction of ΔL1*Dm*TPPII only single strands were observed (see Figure 34E).

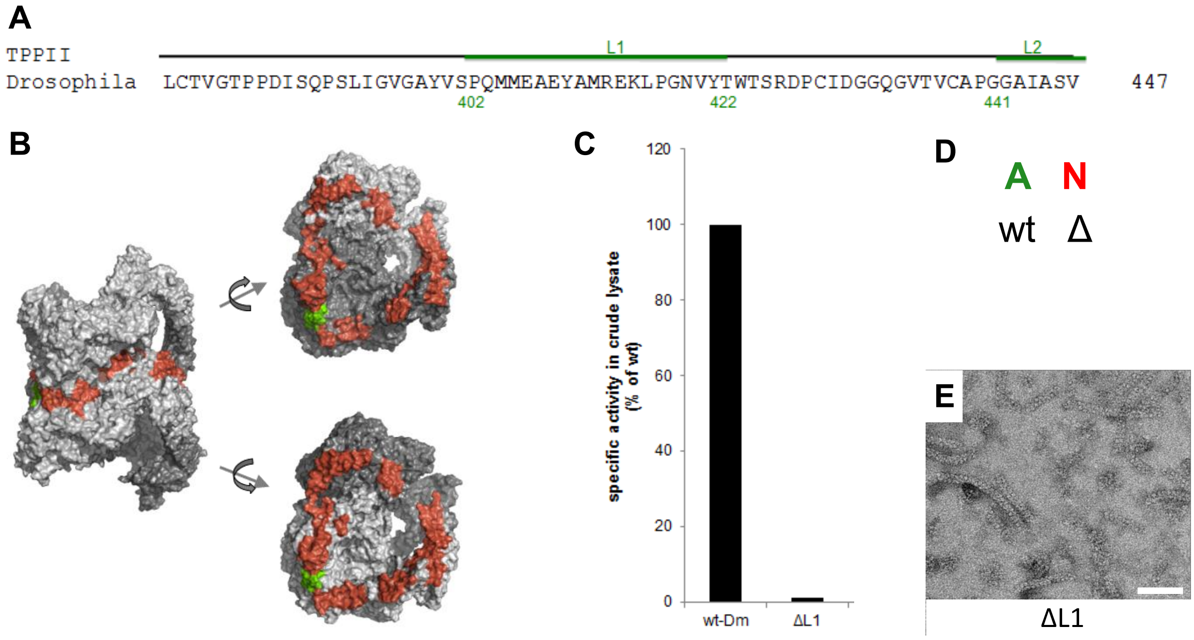

Figure 34: ΔL1-*Dm*TPPII mutant

(A) Partial sequence of *Dm*TPPII; Loop L1 and the N-terminal part of loop L2 are represented by green lines. Numbers below the sequence denote amino acid positions in the TPPII sequence. **(B)** Surface model of *Dm*TPPII dimers as in the complex (left) or rotated by +90°or -90° around the x-axis, respectively. The monomers are colored in dark and light grey; interacting areas are highlighted in red. Residues P402 to Y421 are colored in green. Note: residues E408 to G417 are missing in the surface model. **(C)** Specific activity of the L2-*Dm*TPPII mutants in crude lysate. The specific activity relates to the total amount of protein in the lysate. **(D)** Effects of the deletion of loop L1 in *Dm*TPPII; A: assembly into spindles; N: no assembly into spindles, but into single strands only; red font: specific activity in crude lysate <50% of wild-type protein; green font: specific activity in crude lysate >50% of wild-type protein. **(E)** Electron micrographs of negatively stained particles in the HMW fraction of ΔL1-*Dm*TPPII mutant. Scale bar: 100 nm.

In the case of *Hs*TPPII, the deletion of loop L1 (ΔG389-N403) also strongly decreased the specific activity in crude lysate (see Figure 35A-C) and, additionally, resulted in the formation of single strands only (see Figure 36). The ΔL1 mutation in *Hs*TPPII had similar effects than the same mutation in *Dm*TPPII.

Similar to the Ala-screens in loop L2, the mutations introduced into loop L1 of *Hs*TPPII during the alanine-screen affected TPPII's activity and assembly in various ways. Therefore, the mutants were classified into the same groups as the loop L2-mutants (see 2.4.1). None of the mutants fell into group i or group ii. Six mutations were classified into group iii and five mutations into group iv (see Figure 35A-D and Figure 36).

The LMW peak of the mutants was more prominent for loop L1- than for loop L2-mutants (data not shown). The specific activity of the HMW fraction and the LMW fraction was determined to investigate, whether they were affected in different ways. In all cases where activity of TPPII was detectable in the crude lysate, the specific activity of the HMW fraction was decreased to a larger extent than that of the LMW fraction. The specific activity of the

LMW fraction was either decreased to approximately the same extent as in the crude lysate or even increased above the specific activity of wild-type TPPII dimers (see Figure 35A-C).

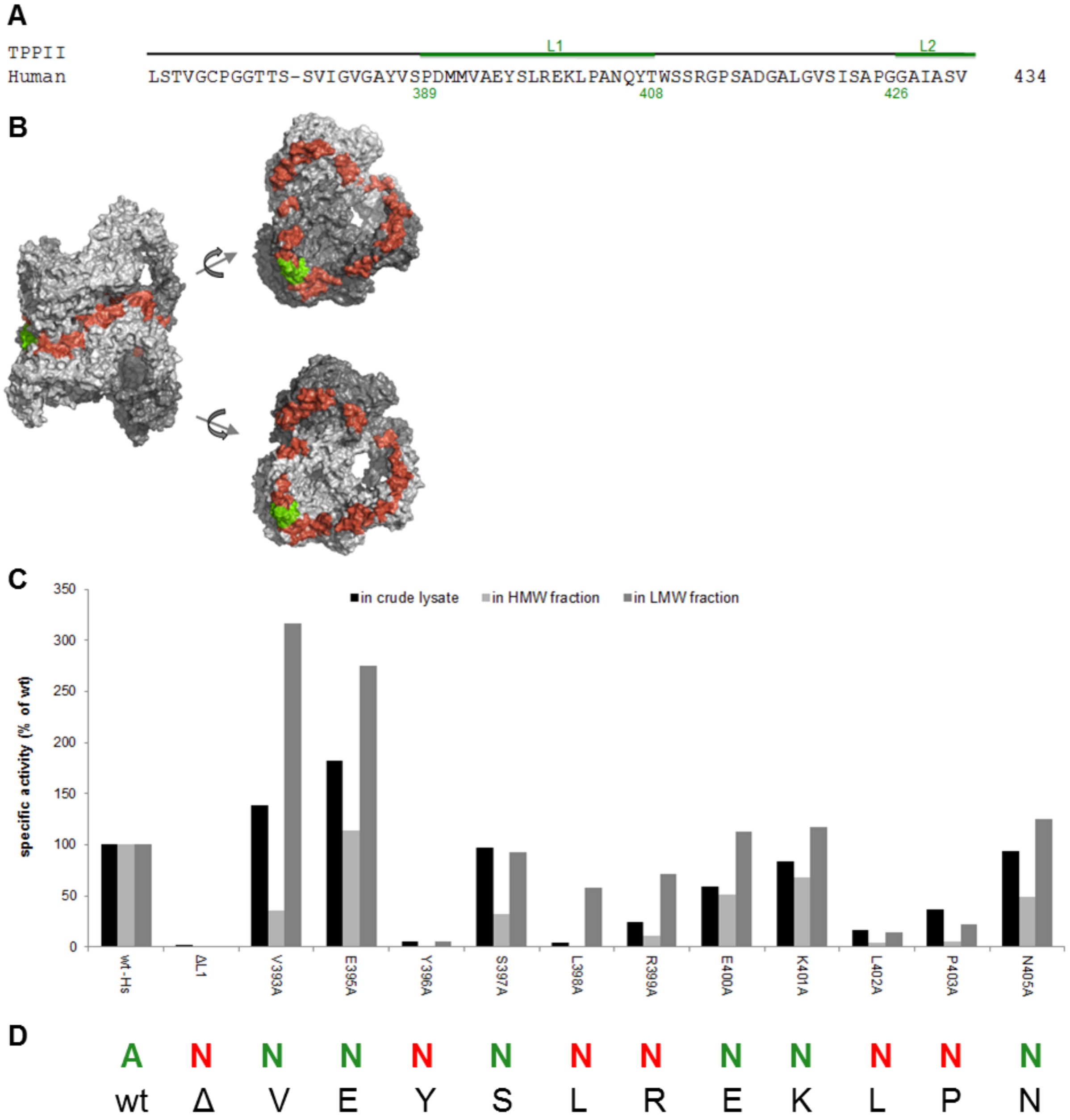

Figure 35: L1-*Hs*TPPII mutants

(A) Part of the sequences of *Hs*TPPII, Loop L1 and the N-terminal part of loop L2 are represented by green lines. Numbers below the sequence denote amino acid positions in the TPPII sequence. **(B)** Surface model of *Hs*TPPII dimers as in the complex (left) or rotated by +90°or -90° around the x-axis, respectively. The monomers are colored in dark and light grey; interacting areas are highlighted in red. Residues P389 to S410 are colored in green. **(C)** Specific activity of the L1-*Hs*TPPII mutants. The specific activity in the crude lysate relates to the total amount of protein in the lysate. The specific activity of the HMW and LMW fraction relates to the amount of TPPII in the fractions. Note: in absolute terms the specific activity of the wild-type LMW fraction is ~ 10% of the wild-type HMW fraction. **(D)** Effects of the mutations in loop L1 of *Hs*TPPII; A: assembly into spindles; N: no assembly into spindles, but into single strands only; red font: specific activity in crude lysate <50% of wild-type protein; green font: specific activity in crude lysate >50% of wild-type protein.

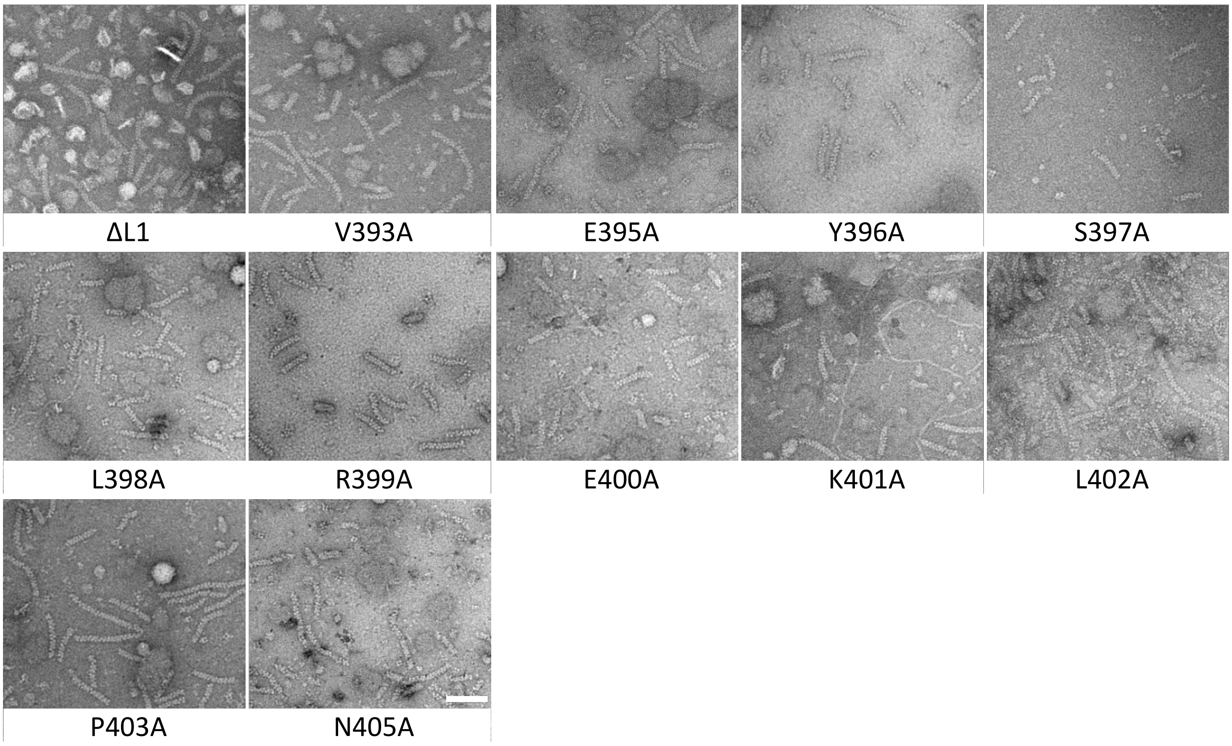

Figure 36: Electron micrographs of L1-*Hs*TPPII mutants

Electron micrographs of negatively stained particles in the HMW fraction of L1-*Hs*TPPII mutants. Scale bar: 100 nm.

In summary, the mutations of loop L1 had an effect on both assembly and activity of the TPPII complex, but they affected assembly much more than activity. This observation implies that loop L1 has a larger effect on assembly than on activation of TPPII. This is in contrast to the situation with loop L2, which plays a stronger role in activation than in assembly.

2.4.3 Putative Interaction Regions of loop L2 and loop L1

In *Dm*TPPII, the acceptor region of loop L2 in the neighboring dimer is supposed to include residues L603 to R610 (Chuang et al., 2010). The pseudo-atomic model of *Hs*TPPII presented here indicates that in *Hs*TPPII actually two regions of the neighboring dimer might interact with loop L2 and/or loop L1: i) M589 to R593 (corresponding to the region proposed for *Dm*TPPII) and ii) E563 to S566 (see section 2.3.3 and 2.3.4). In order to investigate these potential interaction regions, the physico-chemical properties of amino acids in the first interaction region of *Dm*TPPII and *Hs*TPPII (i) were changed and amino acids were exchanged for alanine in the second interaction region of *Hs*TPPII (ii).

The double mutation L603E/L605E and the mutation R610E in *Dm*TPPII reduced the specific activity in the *E. coli* crude lysate to below 50% of wild-type and resulted in single strand formation only (see Figure 37A-E), whereas the mutation D604K decreased the specific activity only gently, but also led to the formation of single strands only (see Figure 37A-E).

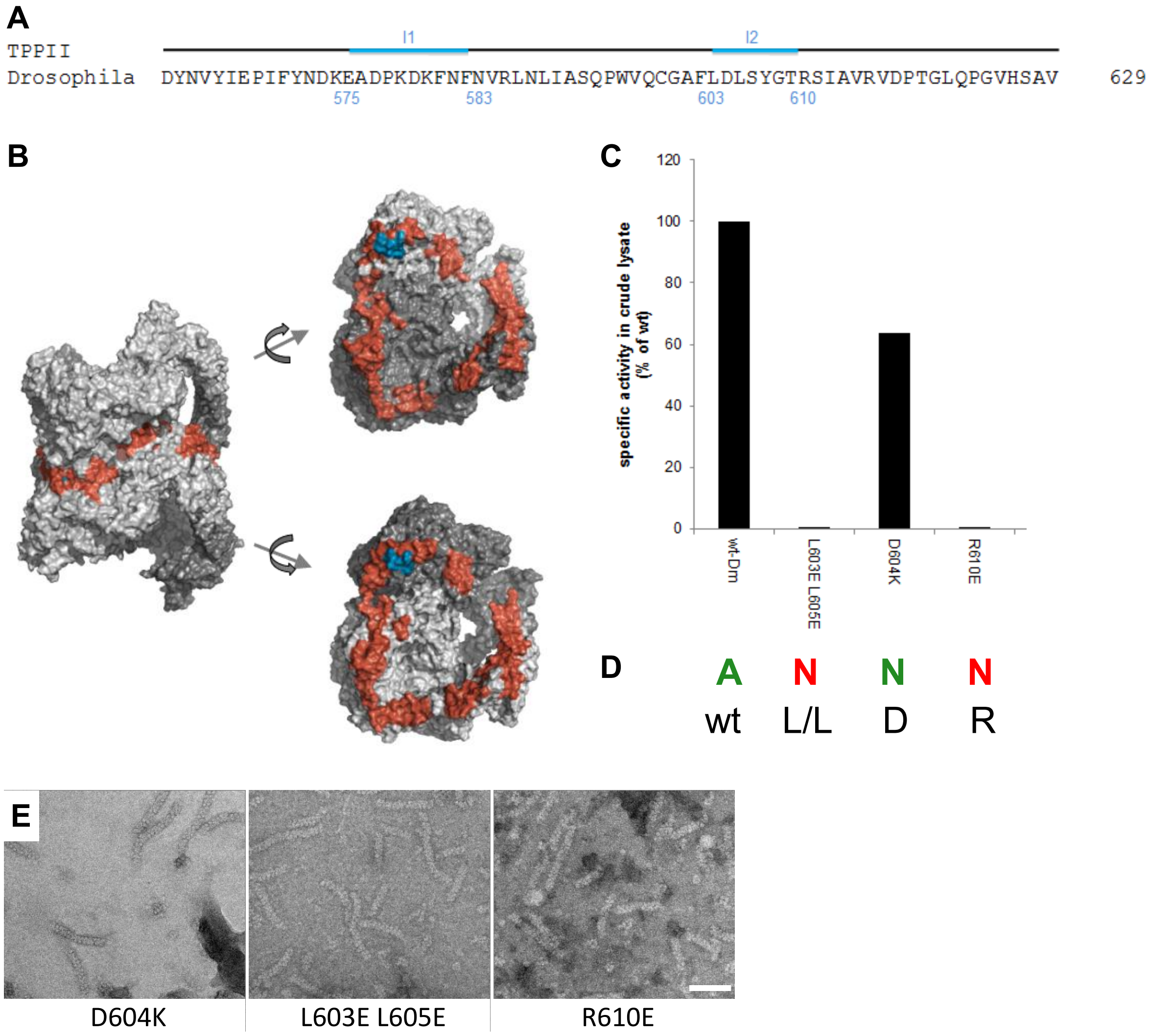

Figure 37: Mutations in the potential loop interaction region of *Dm*TPPII

(A) Partial sequence of *Dm*TPPII, The potential interaction regions are represented by blue lines. Numbers below the sequence denote amino acid positions in the TPPII sequence. **(B)** Surface model of *Dm*TPPII dimers as in the complex (left) or rotated by +90°or -90° around the x-axis, respectively. The monomers are colored in dark and light grey; interacting areas are highlighted in red. Residues D573 to F580 and L603 to R610 are colored in blue. **(C)** Specific activity of mutations in the interaction region of *Dm*TPPII in crude lysate. The specific activity relates to the total amount of protein in the lysate. **(D)** Effects of mutations in the potential interaction region in *Dm*TPPII; N: no assembly into spindles but into single strands; red letter: specific activity in crude lysate <50% of wild-type protein; green letter: specific activity in crude lysate >50% of wild-type protein. **(E)** Electron micrographs of negatively stained particles in the HMW fraction of mutations in the interaction regions of*Dm*TPPII. Scale bar: 100 nm.

In *Hs*TPPII, all mutations in the putative interaction region (M589 to R593) decreased the specific activity in the crude *E. coli* lysate drastically and also altered the morphology of the HMW complex (see Figure 38A-E). Mutations in the stretch E563 to S568 had a minor effect on the specific activity. However, all of them resulted in the formation of single strands only (see Figure 38A-E).

In conclusion, in *Dm*TPPII as well as in *Hs*TPPII mutations of the putative interaction regions affected both assembly and activity of TPPII. The phenotypes of the mutations in the putative acceptor regions resemble the phenotypes of mutations in loop L2 and loop L1, suggesting that these regions are the acceptor regions for these loops, indeed.

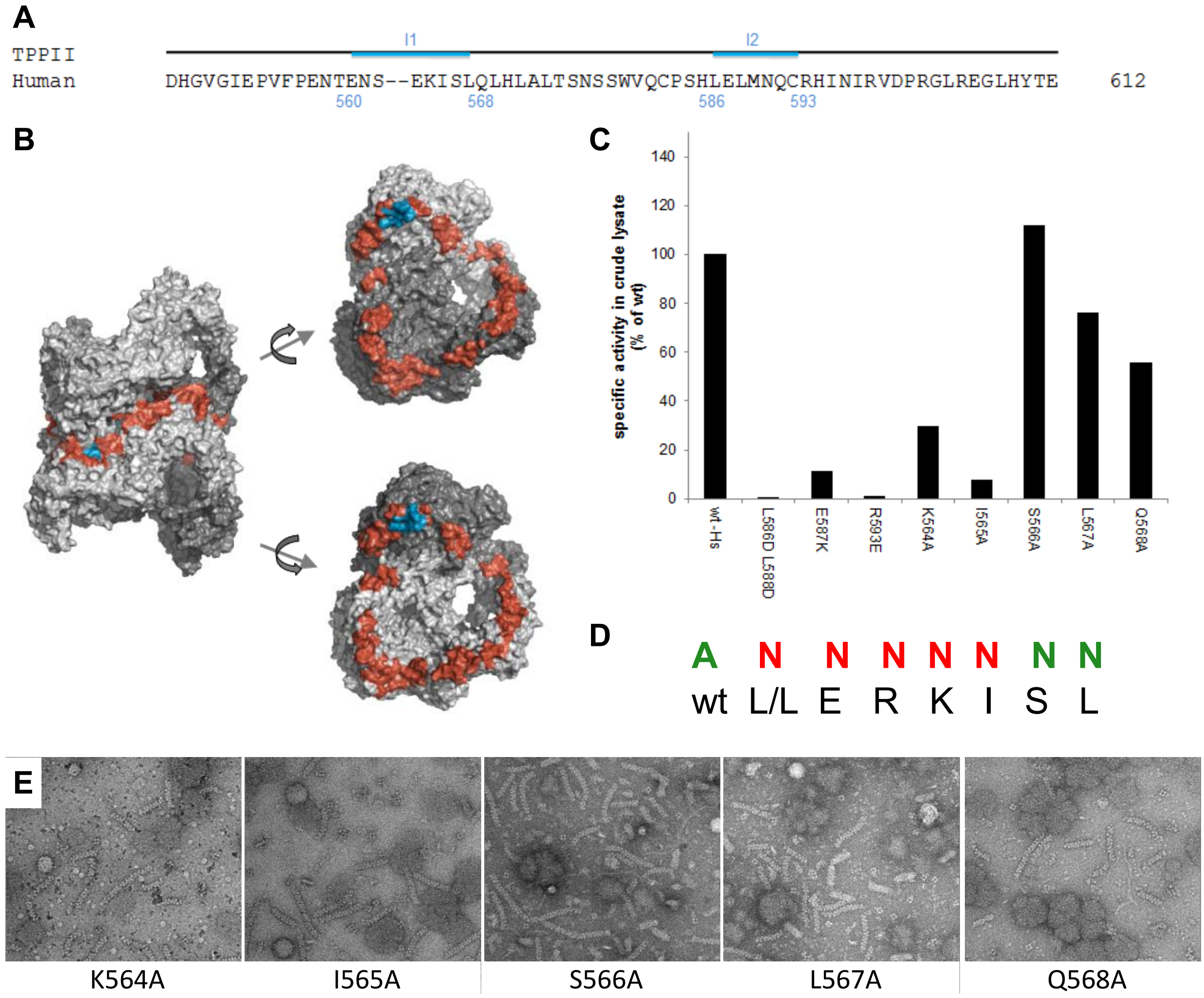

K564A I565A S566A L567A Q568A

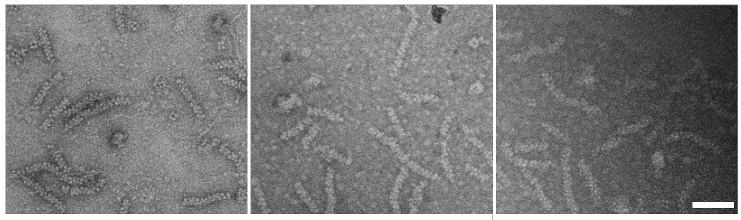

E587K L586D L588D R593E

Figure 38: Mutations in the potential loop interaction regions of *Hs*TPPII

(A) Partial sequence of *Hs*TPPII; the potential interaction regions are represented by blue lines. Numbers below the sequence denote amino acid positions in the TPPII sequence. **(B)** Surface model of *Hs*TPPII dimers as in the complex (left) or rotated by +90°or -90° around the x-axis, respectively. The monomers are colored in dark and light grey; interacting areas are highlighted in red. Residues D573 to F580 and L603 to R610 are colored in blue. **(C)** Specific activity of mutations in the interaction regions of *Hs*TPPII in crude lysate. The specific activity relates to the total amount of protein in the lysate. **(D)** Effects of the mutations in the potential interaction region in *Hs*TPPII; N: no assembly into spindles but into single strands; red letter: specific activity in crude lysate <50% of wild-type protein; green letter: specific activity in crude lysate >50% of wild-type protein. **(E)** Electron micrograph negatively stained particles in the HMW fraction of mutations in the interaction regions of *Hs*TPPII. Scale bar: 100 nm.

2.5 Stabilization of Tetramers by Crosslinking

The systematic mutational analysis of the dimer-dimer interactions presented above did not allow the identification of contacts between specific residues. Therefore, detailed high resolution structural data is needed. A crystal structure of a small oligomer of TPPII would be ideal. The smallest oligomer suitable for this purpose is a tetramer, since it contains one dimer-dimer interface. So far, no procedure to disassemble *Hs*TPPII in a controlled manner has been developed. Although the purification of *Dm*TPPII tetramers is possible (Seyit et al., 2006); the crystal structure obtained is one of *Dm*TPPII dimers (Chuang et al., 2010). One approach to generate stable teramers is to crosslink its subunits. As bifunctional crosslinking agents cause microheterogeneity, which is detrimental to crystallization, the elegant approach of the group of Schultz (Chin et al., 2002) was adopted: The photoreactive corsslinker benzo-phenylalanine (Bpa) is incorporated into the growing peptide chain during protein expression in *E. coli* and UV-treatment results in site-specific crosslinking (Chin et al., 2002).

2.5.1 Bpa in Loop L2

In order to obtain information about its exact position at the dimer-dimer interface, the Bpa-crosslinker was initially incorporated into loop L2. A crosslink of loop L2 interacting with its acceptor region would have two advantages: on the one hand the interacting regions could be identified by mass spectrometry and on the other hand the tetramer would be stabilized. Three positions (N-terminal, middle, and C-terminal) for the incorporation of Bpa were selected: i) F450, since it is a conservative exchange, and ii) S446 and S455, since their exchange for alanine affected neither activity nor assembly (see 2.4.1). The incorporation of Bpa at all three positions in loop L2, however, abolished the activity in the crude lysate (see Figure 39A-D) and also led to the formation of single strands only (see Figure 39D-E).

In summary, the incorporation of Bpa into loop L2 affects activity and assembly of the TPPII complex to an even larger extend than the exchange for alanine at the corresponding position. Moreover, in addition to the Ala-screen, the results demonstrate the sensitivity of the TPPII complex to single amino acid exchanges in loop L2.

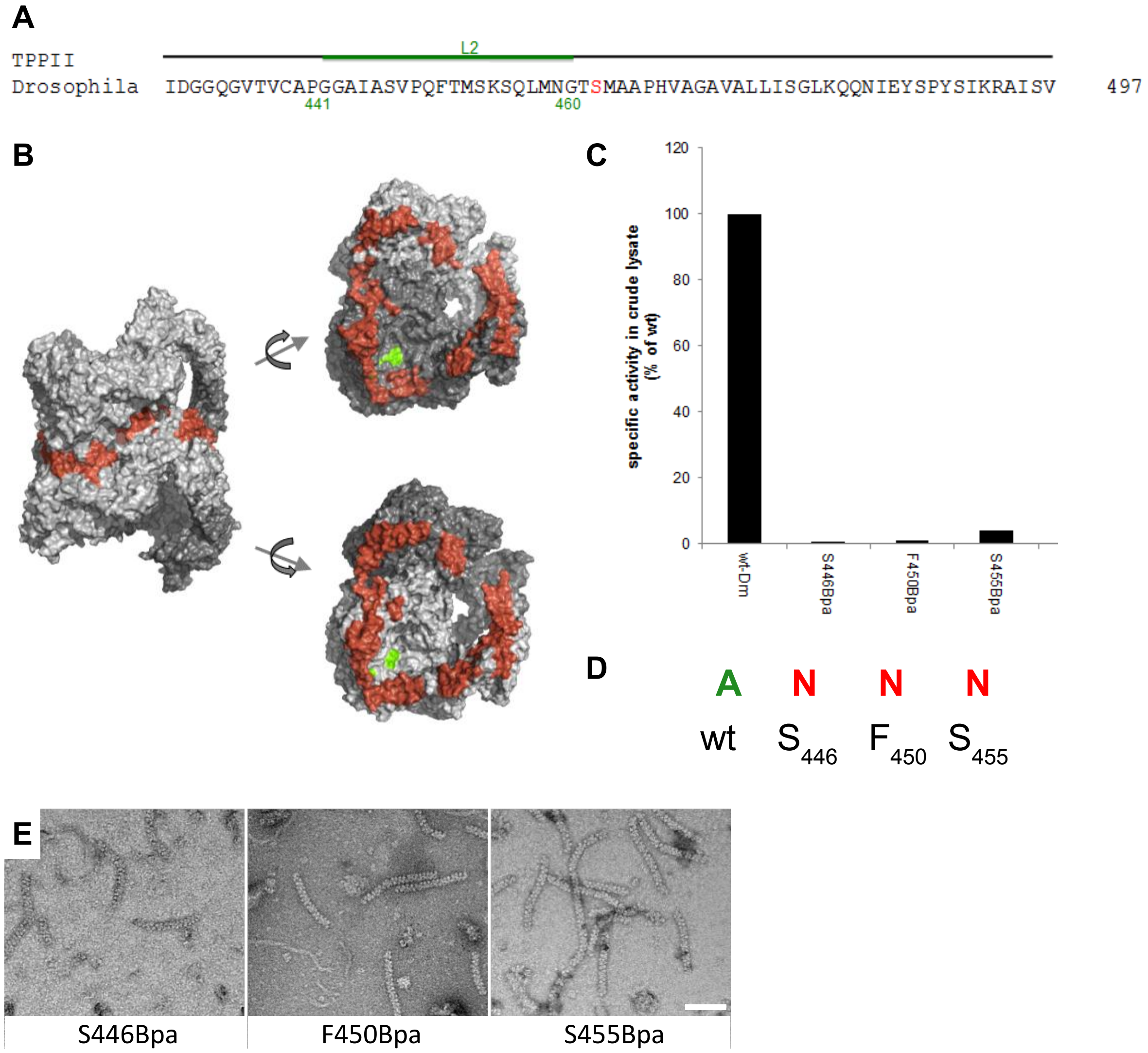

S446Bpa F450Bpa S455Bpa

Figure 39: L2-Bpa *Dm*TPPII Mutants

(A) Partial sequence of the *Dm*TPPII; the active-site serine residue is shown in red. Loop L2 is represented by a green line. Numbers below the sequence denote amino acid positions in the TPPII sequence. **(B)** Surface model of *Dm*TPPII dimers as in the complex (left) or rotated by +90°or -90° around the x-axis, respectively. The monomers are colored in dark and light grey; interacting areas are highlighted in red. Residues F162, F249, F582, F602 and Y607 are colored in yellow. **(C)** Specific activity of L2-Bpa *Dm*TPPII mutants in crude lysate. The specific activity relates to the total amount of protein in the lysate. **(C)** Effects of the incorporation of Bpa into loop L2 of *Dm*TPPII. A: assembly into spindles; N: no assembly into spindles, but into single strands only; red font: specific activity in crude lysate <50% of wild-type protein; green font: specific activity in crude lysate >50% of wild-type protein. **(E)** Electron micrographs of negatively stained particle in the HMW fraction of L2-Bpa *Dm*TPPII mutants. Scale bar: 100 nm.

2.5.2 Bpa at the Dimer-Dimer Interface

All mutations introduced so far are restricted to the regions of loop L2, loop L1 or their potential acceptor regions and almost all of them reduced the activity of TPPII and altered its assembly into the spindle complex. To avoid these effects, the dimer-dimer interface was screened for phenylalanines that are not located in these sensitive regions and four candidates were identified: F162, F249, F582, and F602. In addition, Y607 was chosen to be replaced by Bpa, since though it is located close to the sensitive region it is not part of loop L2, loop L1 or of their potential interaction region. F162 and F249 are located far away from the sensitive region and, indeed, the incorporation of Bpa did affect neither activity nor assembly (see Figure 40A-D). F582, F602 and Y607 are closer to the sensitive regions and, the closer Bpa was incorporated to the sensitive region, the more it reduced the activity of TPPII. However, only the mutation Y607Bpa led to the formation of single strands only (see Figure 40A-D).

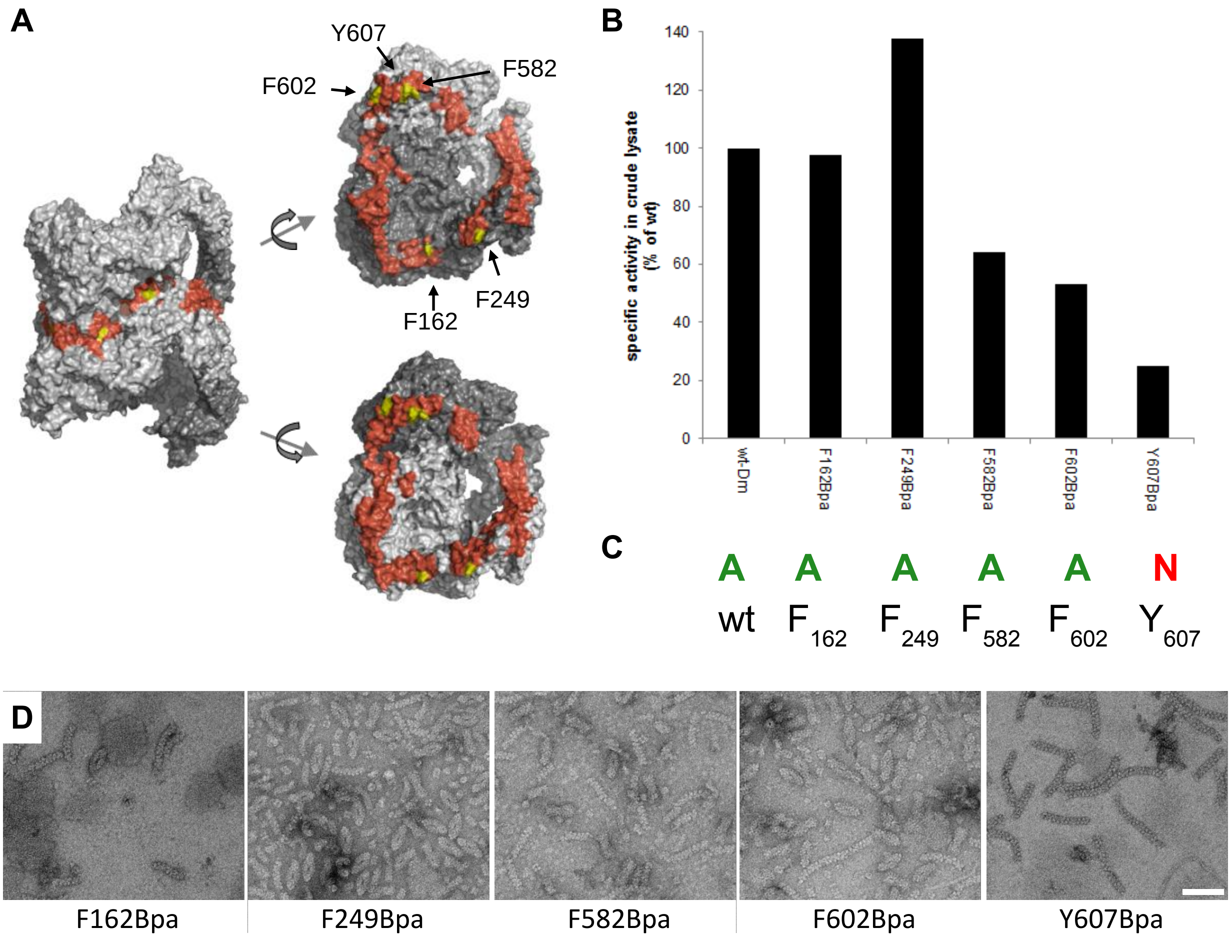

Figure 40: Bpa at the dimer-dimer interface of *Dm*TPPII Mutants

(A) Surface model of *Dm*TPPII dimers as in the complex (left) or rotated by +90°or -90° around the x-axis, respectively. The monomers are colored in dark and light grey; interacting areas are highlighted in red. Residues F162, F249, F582, F602 and Y607 are colored in yellow. **(B)** Specific activity of the dimer-dimer interface *Dm*TPPII mutants in crude lysate. The specific activity relates to the total amount of protein in the lysate. **(C)** Effects of the incorporation of Bpa at the dimer-dimer interface of *Dm*TPPII on in *Hs*TPPII A: assembly into spindles; N: no assembly into spindles, but into single strands only; red font: specific activity in crude lysate <50% of wild-type protein; green font: specific activity in crude lysate >50% of wild-type protein. **(E)** Electron micrographs of negatively stained particle in the HMW fraction of Bpa-interface *Dm*TPPII mutants. Scale bar: 100 nm.

All Bpa-interface mutants were purified and initial photo-crosslinking experiments were performed. In the case of F602Bpa, UV-treatment resulted in additional bands on SDS-PAGE above an apparent molecular mass of 200 kDa, indicating the formation of dimers, and probably also trimers and tetramers (see Figure 41). Preliminary experiments suggest similar photo-crosslinking results for F162Bpa, F249Bpa and Y607Bpa but nor for F582Bpa (data not shown).

In conclusion, the incorporation of Bpa at different positions in the dimer-dimer interface indicates that not the entire interface but distinct regions of this interface are crucial for assembly and activation of TPPII. Furthermore, the purification and the potential crystallization of stable *Dm*TPPII tetramers might be optimized for most Bpa-interface mutants generated in this study.

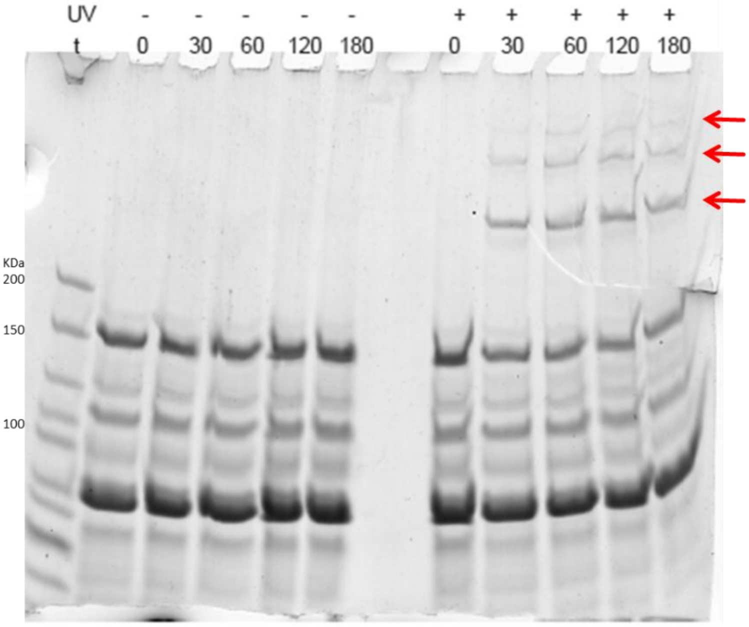

Figure 41: Photo-crosslinking of F602Bpa in *Dm*TPPII

SDS-PAGE of purified F602Bpa *Dm*TPPII incubated at 37°C with and without UV-treatment at different time points. t is given in min.

3 Discussion

This study describes the structure of *Hs*TPPII, a giant cytosolic serine-peptidase. A 3D-map with subnanometer resolution of the *Hs*TPPII spindle complex was obtained by single particle cryo-EM. The 3D-map showed a spindle complex consisting of two strands built of eight or nine stacked dimers. The strands twist around each other and harbor a cavity system. To be able to interpret the 3D-reconstruction of *Hs*TPPII beyond the nominal resolution we combined it with comparative modeling and MDFF. The reliability of the results obtained by this combination depends on the quality of both the initial atomic model and the 3D-map. Ideally, the initial atomic model used in this study should be one obtained by crystallization of small *Hs*TPPII oligomers; however, no method is available for the dissociation of *Hs*TPPII into small oligomers that do not reassemble at high protein concentrations necessary for crystallization. Since the resolution of the 3D-map of *Hs*TPPII is between 6.9 and 9.9 Å, it is certainly not possible to assign or interpret loop regions. However, secondary structure elements like α-helices are discernible and some interpretations such as the determination of interfaces, the existence and positions of α-helices are feasible.

Analysis of the hybrid model allowed the localization of several regions that were considered functionally important: i) helix H13 in the subtilase domain, ii) helix H5, and helix H6 in the DH-insert, and iii) helix H26, helix H27, and loop L3 in th C-terminal region.

3.1 Activation of TPPII

The assembly of TPPII dimers into the spindle complex increases its protease activity. Non-assembled dimers of TPPII exhibit ~10% activity of the fully assembly spindle (Seyit et al., 2006; Tomkinson, 2000). Based the crystal structure of *Dm*TPPII dimers this low activity was attributed to the binding of three residues of loop L2 to the active-site cleft and the resulting displacement of the active-site serine by 5 Å (Chuang et al., 2010). It was postulated that during assembly i) loop L2 is removed from the active-site cleft and interacts with a region at the roof of the catalytic chamber, and ii) a hydrogen bond network similar to the one in subtilisin is established in the active-site region, which leads to the catalytically active conformation of the active-site serine (Chuang et al., 2010).

The 3D-map of *Hs*TPPII suggests that in *Hs*TPPII spindles helix H13 is longer than the corresponding helix in the crystal structure of *Dm*TPPII dimers, since in *Hs*TPPII this helix also includes the actives-site serine S449. Forcing the active-site serine into an active conformation during MDFF, also results in the elongation of helix H13. These observations indicate that the conformation of helix H13 and the catalytically active conformation of the active-site serine are interlinked. In the hybrid model of *Hs*TPPII, loop L2 is located at the dimer-dimer interface in close proximity to the roof of the catalytic chambers. The observations about the positions and/or conformation of helix H13 and loop L2 support the recently proposed activation mechanism (Chuang et al., 2010).

To investigate, whether the establishment of a hydrogen bond network similar to the one in subtilisin is sufficient to render TPPII active, loop L2 and/or helix H13 were replaced by the corresponding elements of subtilisin (loop 'L' and helix hF). All replacements carried out yielded inactive dimers, which assembled into inactive single strands only. These findings suggest that during assembly TPPII undergoes a complex activation process involving more regions than just loop L2 and helix H13. For example, loop L1, which is unique to TPPII and is located close to the active-site, might be involved.

In the hybrid model of *Hs*TPPII, the positions of loop L2 and loop L1 are not very reliable. Therefore potential interaction partners cannot be identified by analysis of the dimer-dimer interface. However, interactions of loop L2 and loop L1 were assessed by (i) deletion, (ii) alanyl-permutation or (iii) site-specific crosslinking with Bpa. Whereas most mutations in loop L2 resulted in inactive single strands, most mutations in loop L1 yielded single strands with reduced activity. Since most mutations did not only affect the activity but also the assembly of the TPPII strands into spindles, no conclusions about the interaction partners of loop L2 and loop L1 could be drawn. However, the results of the mutational studies suggest that even single amino acid exchanges in the dimer-dimer interface can alter the activity and the assembly of the TPPII complex. Mutations at different positions in the dimer-dimer interface showed that activity and assembly of the complex do not depend on the entire dimer-dimer interface, but they depend only on certain regions of the dimer-dimer interface. These functionally relevant regions could be attributed to loop L2, loop L1 and their potential interaction regions, which include M589 to R593 and E563 to I565.

3.2 Assembly as Trigger for Activation

One way to control the spatial and temporal activity of proteases is to express the protease as a zymogen and tightly control its activation. Various mechanisms to achieve this have been described (Lazure, 2002). For some multimeric proteases a relationship between assembly and activation has been reported: Activation of the 20S-proteaseome – the paradigm of self-compartmentalization – occurs after assembly of two half-proteasomes and involves the autocatalytical cleavage of the inhibitory propeptide from the β-subunits (Chen and Hochstrasser, 1996; Witt et al., 2006). Other proteases were shown to be activated through dimerization: For intracellular subtilisin, it was proposed that dimerization opens a metal ion site, which, once occupied, lead to the rearrangement and cleavage of the inhibitory N-terminus (Gamble et al., 2011; Vevodova et al., 2010). In case of the chlamydial protease CPAF, transient dimerization triggers conformational changes that lead to the formation of the active-site and to the autocatalytic processing and removal of an inhibitory segment (Huang et al., 2008; Paschen et al., 2008). All these mechanisms include the cleavage and removal of an inhibitory peptide from the active-site, thereby rendering activation irreversible.

The activation mechanism of the bacterial protease/chaperone HtrA also involves the removal of an inhibitory loop region from the active-site cleft, however, without its cleavage: In the periplasm of gram-negative bacteria HtrA is present as an inactive hexamer. In this complex, a loop from one subunit interacts with a loop of the active-site region in a second, neighboring subunit, thereby distorting the active-site. High temperatures or binding of substrates to PDZ-domains lead to a transition from the hexamer to a 12- or 24-mer. In this 12- or 24-mer the inhibitory loop is removed without cleavage and subsequently, the active conformation of the active-site is restored (Krojer et al., 2010).

Activation mechanisms that involve removal of an inhibitory peptide without its cleavage, such as the ones of HtrA and TPPII, have the advantage of being reversible. In principle, the protease can be turned on and off on demand. However, it appears unlikely that assembly/disassembly of the TPPII complex is the regulator of its activity *in vivo* as these processes occur in minutes to hours *in vitro* (Seyit et al., 2006). It cannot be excluded that assembly/disassembly-accelerating factors exist *in vivo* that facilitate the regulation of TPPII activity by assembly/disassembly.

3.3 The DH-Insert as Sensor of the TPPII Assembly State

The activation model published was based on the hybrid structure of *Dm*TPPII, which was constructed using rigid body fitting (Chuang et al., 2010). Therefore, the conformations of all dimers in the spindle were identical. By using MDFF in the construction of the *Hs*TPPII hybrid model, variations in the dimer conformations were taken into account and this model allowed the detection of potential conformational differences between activated in-strand and non-activated end-of strand dimers. Such conformational differences were found for helix H26 and helix H27 in the C-terminal domain and for helix H6 in domain C of the DH-insert. The new position of these α-helices might stabilize the continuous stretch of TPRs at the convex side of the spindle. In this way, fine-tuning of the potential protein-protein interaction site would be coupled to complex assembly (Rockel et al., 2012). Additionally, the change in position in could initiate the interaction of helix H6 with loop L3, which connects the central and C-terminal domain. These interactions could arrest the loop L3 at its position spanning the entrance to the cavity system and thereby influence the selection of substrates. In the 3D-map of *Hs*TPPII a density corresponding to loop L3 is visible in all dimer, whereas in the

3D-map of *Dm*TPPII it is only visible in terminal dimers (Chuang et al., 2010). Loop L3 in *Dm*TPPII is 57 amino acids shorter than in *Hs*TPPII and is more prone to nicking (J. Peters, personal communication). Presumably, a cleaved loop L3 is more flexible and in turn is invisible in in-strand dimers, implying that in *Dm*TPPII loop L3 is of minor functional importance.

In the comparative model of *Hs*TPPII, which is based on the non-activated *Dm*TPPII dimer, domain C consists of helix H6 and a long loop, into which the short helix H5 is embedded. The shape of the corresponding density in the assembled *Hs*TPPII spindle reveals the presence of two long α-helices. Accordingly, domain C of activated dimers would consist of two long, antiparallel α-helices that are connected by a short loop.

Since the variable helices H6, H26 and H27 are located in or close to the dimer-dimer interface, it is likely that their change in position is directly caused by dimer-dimer interactions. These interactions, plus the movement of helix H6 might also induce the helix-turn-helix conformation in domain C of the DH-insert. The DH-insert is a connector between the C-terminal region and the subtilase domain, which both undergo conformational changes upon assembly and assembly-dependent activation, respectively. It hypothesized that the DH-insert is a sensor for the assembly-state of TPPII and triggers the conformational changes necessary for activation.

3.4 Functional Relevance of the Spindle Complex

Correct stacking of the dimers is essential for the activation of TPPII. Still, small differences between the dimer-dimer interfaces appear to be tolerable. Both the variation in spindle length and the deviation of the strand geometry from an ideal helix show that contacts between dimers within a strand are only quasi-identical. A detailed analysis of the interface would be desirable, but the resolution of the 3D-map does not allow the interpretations of exact locations and orientations of the residues in the flexibly fitted *Hs*TPPII dimers. However, dimer-dimer interfaces within the different spindle complexes were analyzed in terms of the size of their areas, which appear to vary from species to species and which appear not to depend on the number of dimers per strand.

From a functional point of view, it is plausible to assume that the number of dimers per strand is of minor importance as long as the spindle complex is formed. To ensure the formation of the stabilizing double-clamp structure at the spindle poles, a minimum of eight dimers per strand is required. The double clamp stabilizes the spindle complex (Seyit et al., 2006) and thereby also the dimer-dimer contacts.

3.5 Outlook

The hybrid structure of *Hs*TPPII presented in this study provides new insights into the mechanism of maturation and activation of TPPII. However, several open questions remain, such as i) which residues participate in the interactions at the dimer-dimer interface, ii) where is TPPII located in a cell, iii) what are the interaction partners of TPPII in a cellular environment, and iv) is there a single system suitable to perform enzymological, localization, and interaction studies?

3.5.1 Crystal Structure of Tetramers

The establishment of the native dimer-dimer interface is crucial for the functionality and structure of TPPII. However, the structural analysis and the profound mutational analysis of the dimer-dimer interface performed here did not allow drawing any conclusions on the residues and type of interactions that are involved in the dimer-dimer interface. In order to obtain this information, a crystal structure of small oligomers that contain at least one dimer-dimer interface is needed. So far the crystallization of TPPII has been aggravated by the inherent structural heterogeneity attributable to the linear architecture of the complex. However, crystallization of *Dm*TPPII dimers was possible (Chuang et al., 2010). Although a method to purify *Dm*TPPII tetramers is available (Seyit et al., 2006), tetramers need to be stabilized for crystallization to prevent both decay into dimers and assembly at high protein concentrations. In this study a start was made to stabilize tetramers by site-specific crosslinking of subunits with benzo-phenylalanine (Bpa). Whereas the incorporation of Bpa into loop L2 interferes with the correct assembly and activation of the spindle complex, its incorporation at several other positions within the dimer-dimer interface has no such effect. The *Dm*TPPII mutants F162Bpa, F248Bpa, F582, and F602Bpa might be candidates for crystallization of TPPII tetramers.

3.5.2 Cellular Localization

Functional and structural analysis of TPPII *in vitro* can only serve as a starting point for the investigation of its biological role, which is still enigmatic. To understand this biological function, the unambiguous cellular localization of TPPII is necessary. Previous localization studies via immunofluorescence staining had led to confusion about TPPII's potential nuclear translocation upon DNA damage (Firat et al., 2009; Preta et al., 2010a; Preta et al., 2009). Therefore, antibody-independent fluorescence staining would be preferable. TPPII has been labeled with an N-terminal green fluorescence protein (GFP) (Firat et al., 2007; McKay et al., 2007); however, the addition of a large, N-terminal tag prevents spindle formation, as shown for maltose-binding protein (MBP; Rockel et al., 2005) or for GFP (data not shown).

Hence, smaller protein tags, such as the SNAP-tag, or dye-binding peptide sequences, like the FlAsh system, might be a better choice. In either case, it needs to be verified that the addition/insertion of the tag does not interfere with the assembly and/or activity of the spindle complex.

Instead of using a genetically encoded tag, a TPPII-specific activity-based probe (ABP) could be used. ABPs are small molecules that consist of three basic elements: a reactive 'warhead' that reacts selectively with the catalytically active species of the target and remains covalently bound, a tag that facilitates enrichment and/or visualization, and a spacer that both separates the other two elements and influences the selectivity of the 'warhead' (Edgington et al., 2011; Fonovic and Bogyo, 2008; Heal et al., 2011). The tag of this ABP could either be a fluorescence dye or an electron-dense marker. As the ABPs are designed to react with the catalytic active form of an enzyme only, they would only react with assembled, active TPPII. Therefore, if binding, ABPs would probably not interfere with the assembly of the TPPII spindle complex.

3.5.3 Interaction partners

A suitable fluorescence tag could also be used for correlative microscopy of TPPII-containing cells. In correlative microscopy the area of interest is first identified by light- or fluorescence microscopy and subsequently analyzed by (cryo-) EM (Lucic et al., 2007; Lucic et al., 2008). Having an image of TPPII in a cell could provide information on possible interaction partners and/or regulatory proteins of TPPII.

The question of interacting and/or regulatory proteins of TPPII could also be addressed by co-immuno-precipitation in human or *Drosophila* cell lines that heterologously express (tagged) TPPII. However, these expression systems have several drawbacks: i) interference of expressed TPPII protein with the native protein cannot be excluded (e.g. assembly, localization) ii) an antibody having a quality suitable for co-immuno-precipitation is only available for *Dm*TPPII and not for *Hs*TPPII. To prevent any interference with native TPPII, one could rescue TPPII-KO-cells with transient transfections of TPPII. In these rescue-experiments as well as in the heterologous expression TPPII tagged with an epitope tag (c-myc, HA, HSV, or Flag), for which suitable antibodies are commercially available, could be used.

In order to identify interactions that are only transient, weak interaction chromatography with recombinant *Hs*TPPII or *Dm*TPPII and lysate from human or *Drosophila* cells could be performed.

3.5.4 Heterologous Expression in *S. pombe*

To be able to correlate all information obtained, it would be desirable to perform such localization, interaction and enzymological studies of TPPII in a single cellular system. Such a system should offer the possibility of convenient genetic manipulations and, in addition, be suitable for light and electron microscopy. One interesting candidate appears to be *Saccharomyces pombe*. In contrast to *Saccharomyces cervisiae*, *S. pombe* expresses TPPII and its genetic manipulation is routinely performed in several laboratories. Trial purifications have shown that TPPII from *S. pombe* (*Sp*TPPII) also forms a spindle complex, but quality and amount of purified *Sp*TPPII were not suitable for functional or structural studies. An affinity tag to aid the purification of *Sp*TPPII could help to solve this problem. Furthermore, such a tag could be helpful in identifying native interaction partners by co-immuno-precipitation and weak interaction chromatography.

4 Experimental Procedures

4.1 Methods

4.1.1 DNA-Methods

4.1.1.1 Mutagenesis

To introduce position-specific mutations into *Dm*TPPII and *Hs*TPPII, the *QuikChange Site-Directed Mutagenesis Kit* was employed. The primers used are specified in section 4.3 and the vectors produced are listed in section 4.2.4.
A typical PCR reaction composed as following:

3 µl	10x Puffer
1 µl	dNTPs
1 µl (ca. 90 ng)	Template-Plasmid
1 µl	forward bzw. reverse Primer
2 µl	PfuUltra DNA-Polymerase
ad 30 µl	$H_2O_{Milli\text{-}Q}$

Two separate reactions, including either the forward or the reverse primer, were set up. After 6 cycles of amplification, 15 µl of each reaction were pooled and 1 µl PfuUltra DNA-polymerase was added. The amplification was continued for 18 cycles. The amplification was performed in a PCR-Thermocycler *GeneAmp PCR System 2400* from Perkin Elmer with the following program:

30 sec	95°C	
30 sec	95°C	6x bzw. 18x
1 min	55°C	
10 min	68°C	
11 min	68°C	

To remove the template DNA 1µl DpnI was added to the PCR product and the mixture was incubated at 37 °C for 1 h.

4.1.1.2 Heat Shock Transformation of *E. coli*

50 µl of competent cell (XL1-Blue or Top10) were thawed on ice. 5 µl of the DpnI-digested PCR reaction or 0.5 µl to1 µl of purified plasmid was added to chemocompetent XL1-Blue or Top10 bacteria, respectively. The reaction mixture was incubated on ice for 30 min. A heat shock was performed for 45 sec at 42 °C, followed by 2 min incubation on ice. 500 µl of SOC was added to the cells, which were subsequently incubated at 37 °C for 1 h with constant shaking. Afterwards the cells were plated on LB-plates with the corresponding selection marker.

4.1.1.3 Isolation of Plasmid DNA from *E. coli*

One single colony from an agar plate was used to inoculate 4 ml LB-media. The culture was grown over night. Cells were sedimented by centrifugation (13,000xg, 2 min, RT) and their plasmid DNA was isolated employing the QIAPrep Spin Miniprep Kit (QIAGEN).The plasmid DNA was analyzed by agarose gel electrophoresis and sequencing.

4.1.1.4 Agarose Gel Electrophoresis

Plasmid DNA with loading dye was loaded on a 0.8% agarose gel and separated at 100 V. Afterwards the gel was incubated in an ethidium bromide solution for 10 min with gentle shaking and bands were visualized by UV light of 312 nm.

4.1.1.5 Sequencing of Plasmid DNA

For DNA sequencing 300 ng of DNA were mixed with 5 pmol of primer and the volume was adjusted to 7.5 µl. Sequencing was performed by the Microchemistry Core Facility of the Max Planck Institute of Biochemistry.

4.1.2 Proteinbiochemistry

4.1.2.1 Large Scale Recombinant Expression of TPPII

Large scale expression of *Dm*TPPII and *Hs*TPPII in a 1 l continuous feeding fermentation system was performed by the Microchemistry Core Facility of the Max Planck Institute of Biochemistry.

4.1.2.2 Small Scale Recombinant Expression of TPPII

For the recombinant expression of *Dm*TPPII 50 ml TB_{Kan}-medium was inoculated and grown until an OD_{600} 2 – 3 was reached. The expression was induced by the addition of 0.1 mM IPTG and carried out over night at 18 °C for *Dm*TPPII and at 24 °C for *Hs*TPPII.

4.1.2.3 Large Scale Purification of *Hs*TPPII

Cells expressing *Hs*TPPII were harvested by centrifugation (10 min at 4000xg). Resuspended cells were subjected to two passages through a cell disrupter EmulsiFlex-C5 (Avestin) and centrifuged for 20 min at 30000xg. The pellet was suspended in resuspension buffer and passed through the cell disrupter again. After centrifugation for 20 min at 30000xg the His-tagged protein was purified from the supernatant by affinity chromatography using HisTrap™ HP Columns. The column was equilibrated with HisTrap loading buffer. Washing was performed with the HisTrap washing buffer. The proteins were eluted by an imidazol step gradient ranging from 200 mM to 400 mM imidazole using the HisTrap elution buffer. Subsequently, the imidazole was removed using PD10 desalting columns. Further purification was achieved by applying the sample to a HiTrap™ ANX FF Column equilibrated with ANX binding buffer. Elution was carried out by an ammonium sulfate step gradient of 100 mM to 400 mM AS using the ANX elution buffer. The fractions showing TPPII activity were collected and subjected to precipitation at 55% (w/v) saturated AS at pH 7.5–7.7. The precipitate was collected by centrifugation at 30000xg for 20 min, dissolved in resuspension buffer, and loaded on a Superose 6 10/300 size exclusion column with resuspension buffer as eluent.

4.1.2.4 Small Scale Purification of TPPII

Cells expressing wild type TPPII or TPPII mutants were harvested by centrifugation (10 min at 4000xg), resuspended in 3 volumes resuspension buffer and lysed by sonication. The samples were centrifuged at 21000xg for 10 min. DNA was removed by addition of 0.3% PEI and centrifugation at 21000xg for 2 min. Subsequently proteins were precipitated by addition of 1 volume 4 M AS. The solution was incubated on ice for 30 min and then centrifuged at 21000xg for 10 min. The pellet was dissolved in 1 ml resuspension buffer and loaded on a Superose 6 10/300 size exclusion column. Fractions of 0.75 ml were collected and analyzed via SDS-PAGE and activity measurements.

4.1.2.5 Activity Measurement

The activity of TPPII was determined by measuring the fluorescence emission of Amc released by the cleavage of the fluorogenic substrate AAF-Amc in a Kontron Fluorimeter (excitation: 360 nm; emission: 460 nm). As reference the fluorescence of 0.2 mM free Amc was used. To inhibit cleavage of the substrate by other proteases the non-specific aminopeptidase inhibitor bestatin was included in the reaction. The assay was performed at 30 °C for *Dm*TPPII and at 37 °C for *Hs*TPPII.

The assay volume was 50 µl. For the activity measurement of crude lysate 2 µl of a 1/10 dilution were added to the assay and the mixture was incubated for 30 sec before the reaction was stopped by adjusting the volume to 500 µl with Stop buffer.

The activity of Superose 6 fractions was determined after the addition of 1 to 20 µl sample to the assay mix and incubation between 30 sec and 10 min. The reaction was stopped by adjusting the volume to 500 µl with Stop buffer.

The counts of the fluorescence measurements are correlated to the TPPII concentration by the following equation:

$$[TPPII] = \frac{counts \times 10}{specific\ activity\ \times\ V\ \times t}$$

;where ‘counts’ is the measured fluorogenic signal, ‘specific activity’ is 6000 $pmol/\mathrm{min} \times mg$ for *Dm*TPPII and 13000 $pmol/\mathrm{min}\ \times mg$ for *Hs*TPPII; V is the volume added in µl and t is the time incubated in min. TPPII concentration is calculated in mg/ml.

4.1.2.6 SDS-PAGE

For SDS-PAGE the buffer system of Schägger und von Jagow (Schagger and von Jagow, 1987) was used. The acrylamide concentration was 9%. Samples were mixed with 0.2 volumes of sample buffer and solubilized at 70°C for 5 min. Electrophoretic separation was performed at 100 V for ~40 min. Gels were washed in H_2O three times for 2 min. Then the gel incubated in Comassie staining solution for at least 1 h with gentle shaking. Destaining occurred in H_2O overnight.

4.1.2.7 Western Blotting

After SDS-PAGE, the proteins were transferred to a nitrocellulose membrane by wet blotting for 3 h at 90 V. Completion of the transfer was controlled by Ponceau S staining. Western Blot was performed using the ONE-HOUR Western^{TM} Detection Kit. The primary antiserum α-*Hs*TPPII was diluted 1:500 and the antiserum α-*Dm*TPPII was diluted 1:2000. Both antisera were produced in the Animal Facility of the Max Planck Institute of Biochemistry.

4.1.2.8 Determination of Specific Activity

For the determination of the specific activity of the HMW and LMW complexes of TPPII, the activity of the fractions eluted at 8.1 ml and 14.9 ml, respectively, was measured. The amount of TPPII in these fractions was detected densitometrically after separating the proteins via SDS-PAGE.

4.1.2.9 Bpa-Incorporation

For the incorporation of Bpa the system introduced by Prof. Schultz (Scripps Research Institute, La Jolla) , which incorporates Bpa at the position of the *amber* stop codon in the growing amino acid chain, the plasmid pSub-Bpa (Chin et al., 2002) and the plasmid containing TPPII with an *amber* stop codon (TAG) were cotransformed in BL21 (DH3) Gold. The expression was performed as described in section 4.1.2.2.

4.1.2.10 Bpa-Crosslinking

TPPII containing Bpa was purified as described in section 4.1.2.3 or in (Seyit et al., 2006). The purified proteins were UV-treated in a 37 °C-tempered UV-cage for 3 h. Controls were incubated at 37°C without UV-treatment. Crosslinking was examined by SDS-PAGE.

4.1.3 Electron microscopy

4.1.3.1 Negative-stain EM

Copper grids (PLANO W. Plannet GmbH, 100x400 mesh) were carbon coated and glow-discharged for 25 sec with a plasma cleaner (Harrick Scientific Corporation). The grid was put on a drop of 5 µl sample and incubated for 1 min at room temperature. Next, the grid was transferred twice to drops of 20 µl 40 mM AS, pH 7.5. Subsequently, staining was performed with 2% uranylacetat for 45 sec. Electron microscopic images were acquired at a CM200 transmission electron microscope (Philips) operated at 160 kV equipped with a TVIPS CCD camera (camera pixel size 15 µm; 4096x4096 px). The final magnification was 69500x resulting in an object pixel size of 2.2 Å. The nominal focus of the images was -2 to -3 µm.

4.1.3.2 Cryo-EM

5µl of freshly purified protein solution was applied to glow-discharged C-flat 4/1 grids (Protochips, Inc.), which were covered with a thin carbon film. The grids were washed twice with buffer (40 mM ammonium sulfate, pH 7.5), blotted and plunge-frozen in liquid ethane. Using a Tecnai F20 microscope (FEI) operated at 200 kV and equipped with an Eagle CCD camera (camera pixel size 15 µm; 4096x4096 px), 2248 focal pairs were recorded semi-automatically (SerialEM, (Mastronarde, 2005) at a calibrated magnification of 84270x, resulting in an object pixel size of 1.78 Å on specimen level. Focus values of the close-to-focus images ranged from -0.3 to -4.7 µm.

4.1.3.3 Image Processing

Prior to single-particle analysis, all micrographs were visually screened for drift, astigmatism, and visibility of Thon rings in the power spectrum. Subsequently, the contrast transfer function was determined and micrographs were deconvoluted by phase flipping and compensation for the modulation transfer function of the CCD camera using the TOM-software (Nickell et al., 2005). The positions of 96116 particles were determined on the far-to-focus images and particles were extracted in 384 x 384 boxes from the close-to-focus images (EMAN-software; Ludtke et al., 1999). For the reconstruction of all particles a featureless double bow was used as initial reference. The settings for the iterative alignment process are listed in section 4.4.1.

2D-classification of the data was performed using the EM-Package (Hegerl, 1996) and XMIPP (Scheres et al., 2008). The 3D-variance map was calculated according to Penczek et al., 2006. Seeds for a ML3D classification were generated based on a featureless double bow. The ML3D classification was performed with 2x-binned particles and imposing C2 symmetry using XMIPP (Scheres et al., 2008). For the reconstruction of the two classes the 3D-models from the ML3D-runs were centered and used as initial references. The angular assignments from the ML3D-runs were used as starting point for the reconstructions. The settings during the iterative alignment processes for the 3D-reconstructions are summarized in 4.4.2 and 4.4.3. The temperature factor was determined (Rosenthal and Henderson, 2003) and applied to the final reconstructions (all: ~ -100 $Å^2$; *Hs*TPPII$_9$: ~ -330 $Å^2$; *Hs*TPPII$_8$: ~ -610 $Å^2$).

4.1.3.4 Determination of Helix Parameters

Additional image analysis of the 3D-reconstruction was carried out by using the EM software package (Hegerl, 1996). A low-pass filtered model of the atomic model of *Dm*TPPII dimers (smoothed to a resolution similar to that of the 3D-reconstructions) was used to perform template-matching of dimers in the 3D-reconstructions. The resulting positions and Euler angles were converted to equivalent representations, which describe the relative movement of dimer$_n$ to dimer$_{n+1}$ by a simple shift and a rotation around an individual axis. For one strand, these axes have nearly the same orientation and the corresponding rotation angles as well as the shifts are nearly constant. Subsequently, each strand was then approximately represented as a helix using the average of the individual rotation axes as helical axis. This analysis was performed by Dr. Reiner Hegerl (Max Planck Institute of Biochemistry, Martinsried).

4.1.3.5 Comparative Modeling and Flexible Fitting

A comparative model of HsTPPII was built using DmTPPII as structural template (PDB ID 3LXU; 36% sequence identity). The model was built using MODELLER (Sali and Blundell, 1993) with multiple sequence alignments from T-COFFEE (Notredame and Suhre, 2004). This model was produced by Dr. Friedrich Förster (Max Planck Institute of Biochemistry, Martinsried).

An initial atomic model of *Hs*TPPII$_8$ and *Hs*TPP$_9$ was created by rigid body fitting of comparative models of the dimer into the respective EM-maps using situs (Wriggers et al., 1999). Steric clashes were resolved with an in-house interactive version of MDFF implemented in VMD (Humphrey et al., 1996). The spindle models resulted in systems of 605,122 and 680,762 atoms, including hydrogens, for *Hs*TPPII$_8$ and *Hs*TPP$_9$, respectively. MDFF simulations were ran with default parameters and restraints (Trabuco et al., 2008), plus three extra restraints per monomer enforcing the conformation of the active-site residues to mimic their conformation in the crystal structure of subtilisin (Bode et al., 1987). Additionally, implicit-solvent simulations were used, and the D2 symmetry observed in the EM data was imposed into the simulated structures using a custom TclForces implementation. Simulations of each spindle were run for 2 ns. The root-mean-squared fluctuation (RMSF) and dimer-dimer interaction analysis considered the last nanosecond of the trajectory, where the ensemble of structures produced all conformed to the EM data.

Correlation coefficients were determined using the ‘fit in map’ option in Chimera with a simulated map of the dimer at a resolution of 10 Å (Pettersen et al., 2004). RMSF values were calculated using VMD (Humphrey et al., 1996) Fitting of the atomic models to the 3D-reconstructions was performed by Dr. Elizabeth Villa (Max Planck Institute of Biochemistry, Martinsried).

4.1.3.6 Determination of Interaction Areas and Steric Clashes

Interaction areas were calculated using the EBI (European Bioinformatics Institute) online server PISA (Protein Interfaces, Surfaces and Assemblies; Krissinel and Henrick, 2007).

Clashes between dimers were determined using the ‘find clashes’ option in Chimera (Pettersen et al., 2004) with standard settings.

4.2 Materials

4.2.1 Chemicals

7-Amino-4-Methylcoumarin (Amc)	Bachem
Acetic acid	Merck
Acrylamid Protogel 30 % (w/v)	National Diagnostics
Agarose	Sigma
Ala-Ala-Phe-Amc (AAF-Amc)	Bachem
Ammoniumperoxidsulfat (APS)	Merck
Ammoniumsulfat (AS)	Merck
Ammoniumsulfate-16-hydrate	Roth
Bacto Tryptone	Difco
Bacto Agar	Difco
Bacto Yeast Extract	Difco
Bestatin	Sigma
Bromphenol blue	Serva
Chloramphenicol	Serva
Comassie Brilliant Blue G 250 (cbb g259)	Serva
Dimethylsulfoxid (DMSO)	Merck
1,4-Dithiothreitol (DTT)	Merck
Ethylenediaminetetraacetic acid (EDTA)	Merck
Ethanol p.a.	Merck
Ethidiumbromid	Merck
Glycin	Sigma
Glycerol 86-88%	Riedel-de Haen
Guanidinhydrochloride	Merck
Hydrochloric acid	Merck
Imidazol	Merck
Kanamycin	Sigma
3-Hydroxy-4-[2-Sulfo-4-(4-Sulfophenylazo)-Phenylazo]-2,7-Phtalindisulfonic acid (Ponceau S)	Sigma
Isopropyl-β-D-Thiogalactopyranosid (IPTG)	Biomol
NZ Amine	Difco
Phosphoric acid	Merck
Polyethyleneimine (PEI)	Sigma
Potassiumhydroxid	Merck
Potassiumdihydrophosphat (KH_2PO_4)	Merck
Dipotassiumhydrogenphosphat (K_2HPO_4)	Merck
Protein-Assay Reagent	Bio-Rad
Sodiumchloride (NaCl)	Merck
Sodiumdodecylsulfat (SDS)	Bio-Rad
Trizma® Base (Tris)	Sigma
Trichloressigsäure (TCA)	Merck
N,N,N‘,N‘-Tetramethylethylendiamin (TEMED)	Serva

4.2.2 Buffers and Solutions

All buffers and solutions were prepared with deionised water from the Milli-Q Plus Ultrapure Water Purification System (Millipore; $H_2O_{Milli\text{-}Q}$). Buffers used for chromatography were degassed by filtering through an Express™ Plus filter (Millipore) with a pore size of 0.22 µm under vacuum.

Buffers for agarose-, polyacrylamid gelelectrophorese und Western Blot

TAE (Tris-Acetat-EDTA)
40 mM Tris-Acetate, pH 8.0
1 mM EDTA

Sample buffer SDS-PAGE (6x)
50 mM TEA/PO_4, pH 8,5
5 % (w/v) SDS
30 % (v/v) Glycerin
0.12 % (w/v) Bromphenolblue
addition of 50 mM DTT before use

Buffer B for SDS-PAGE
3 M Tris
0.3 % SDS
Ad 250 ml $H_2O_{Milli\text{-}Q}$
adjust pH 8.5 with 6N HCl

Cathode buffer for SDS-PAGE
100 mM Tris
100 mM Tricine
0.1 % (w/v) SDS

Comassie staining solution
5% (w/v) AS-16-hydrate
10% (w/v) Ethanol (96%)
0.02% (w/v) cbb g250
2% (w/v) phosphoric acid (85%)

Transfer buffer
250 mM Tris
1.92 M Glycin

Ponceau S
0.1 % Ponceau S
5 % acetic acid

Buffers for protein purification

Reusupension buffer
80 mM KPO_4, pH 7.5
1mM DTT
5% Glycerol

HisTrap bindhing buffer
80 mM KPO_4, pH 7.5
1mM DTT
5% Glycerol
20 mM Imidazol

HisTrap washing buffer
80 mM KPO_4, pH 7.5
1mM DTT
5% Glycerol
50 mM Imidazol

HisTrap elution buffer
80 mM KPO_4, pH 7.5
1mM DTT
5% Glycerol
200-400 mM Imidazol

ANX binding buffer
80 mM KPO_4, pH 7.5
1mM DTT
5% Glycerol

ANX elution buffer
80 mM KPO_4, pH 7.5
1mM DTT
5% Glycerol
100-400 mM AS

Solutions for biochemical methods

Activity assay
100 mM KPO_4, pH 7.5
0,2 mM AAF-AMC
0,02 mM Bestatin
1 mM DTT

DTT-solution
1M in $H_2O_{Milii\text{-}Q}$

IPTG-solution
0.1M in $H_2O_{Milii\text{-}Q}$

Stop buffer
100 mM Tris/HCl, pH 9.5
1 % SDS

Chloramphenicol
34 g/l in Ethanol

Kanamycin
30 g/l in $H_2O_{Milii\text{-}Q}$

4.2.3 Media

All media were prepared with demineralised H_2O and autoclaved for 20 min at 120 °C.

SOC-Media

20g/l (w/v) Bacto Tryptone
5g/l (w/v) Bacto Yeast Extract
2ml/l of 5M NaCl.
2.5ml/l of 1M KCl.
10ml/l of 1M $MgCl_2$
10ml/l of 1M $MgSO_4$
20ml/l of 1M glucose

.

LB_0-Media

10 g/l (w/v) Bacto Tryptone
5 g/l (w/v) Bacto Yeast Extract
10 g/l (w/v) NaCl
for plates: 15 g/l Bacto Agar

LB_{Chlor}-Media

LB_0-Medium
Addition of 50 mg/l Chlroampehnicol after sterilization

$LB_{Kan/Chlor}$-Media

LB_0-Medium
Addition of 30 mg/l Kanamycin and 34 mg/l Chlroampehnicol after sterilization

LB_{Kan}-Media

LB_0-Medium
Addition of 30 mg/l Kanamycin after sterilization

TB-Media

Part 1 12 g Bacto Tryptone
24 g Yeast Extract
4 ml Glycerol
ad 900 ml H_2O_{MilliQ}
Part 2: 2.3 g K_2HPO_4
16.4 g KH_2PO_4
ad 100 ml H_2O_{MilliQ}

Part 1 and part 2 are autoclaved seperately and pooled afterwards to obtain 1 l of media

TB_{KAN}-Media

TB-Medium
Addition of 30 mg/l Kanamycin after sterilization

$TB_{Kan/Chlor}$-Media

TB-Medium
Addition of 30 mg/l Kanamycin and 34 mg/l Chlroampehnicol after sterilization

TB-$Bpa_{Kan/Chlor}$-Media

TB-Medium containing 1mM Bpa
Addition of 30 mg/l Kanamycin and 34 mg/l Chlroampehnicol after sterilization

4.2.4 Vectors

pSub-Bpa (Chin et al., 2002)

***Hs*TPPII**

The *Hs*TPPII-gene is cloned in the pET28a-Vector. Which contains a N-terminal His_6-tag with a 10aa-linker. The T7-promoter is inducible by IPTG. The vector encodes a kanamycin resistance gene. The following mutations were introduced in this work:

1. ΔL2 (ΔG429-N446)
2. I431A
3. S433A
4. V434A
5. N436A
6. W437A
7. T438A
8. L439A
9. R440A
10. T442A
11. Q443A
12. L444A
13. M445A
14. N446A
15. ΔL1 (ΔP389-N405)
16. V393A
17. E395A
18. Y396A
19. S397A
20. L398A
21. R399A
22. E400A
23. K401A
24. L402A
25. P403A
26. N405A
27. L585D/L587D
28. D586K
29. R593E
30. K564A
31. I565A
32. S566A
33. L567A
34. Q568A

***Dm*TPPII**

The *Dm*TPPII-gene is cloned in the pET30b-Vector. The T7-promoter is inducible by IPTG. The vector encodes a kanamycin resistance gene. The following mutations were introduced in this work:

1. Δ448-449
2. V447T/Δ448-449
3. Δ448-449/T451P
4. V447T/Δ448-449/T451P
5. A465S/V472A/L475I/I476L (Sub hF)
6. G442A/A443G/444V/A445Y/V447T/F450Y/T451P/M452T/K454T/S455V/Q456A/L457T/M458L (Sub loop 'L')
7. 5+6 (Sub hF + loop 'L')
8. ΔL2 (ΔG442-N459)
9. I444A
10. S446A
11. V447A
12. Q449A
13. F450A
14. T451A
15. M452A
16. S453A
17. K454A
18. S455A
19. Q456A
20. L457A
21. M458A
22. N459A
23. ΔL1 (ΔP402-P416)
24. L603E/L605E
25. D604K
26. R610E
27. S446Stop
28. F450Stop
29. S455Stop
30. F162Stop
31. F248Bpa
32. F582Bpa
33. F602Bpa
34. Y607Bpa

4.2.5 Bacteria

XL1-Blue	Agilent Technologies
Top10	Invitrogen
BL21 (DH3) Gold	Invitrogen

4.2.6 Kit-systems

QIAprep Spin Miniprep Kit	QIAGEN
Quickchange II XL Site-Directed Mutagenesis Kit	Agilent Technologies
One-Step$^{\mathrm{TM}}$ Western Blot Kit	GenScript

4.2.7 Enzymes

Pfu Ultra DNA-Polymerase (2,5 U/µl)	Agilent Technologies
DpnI (10 U/µl)	Agilent Technologies
Restriktionsenzyme (NotI, NcoI, NdeI, XhoI)	Fermentas
Lysozyme	Sigma

4.2.8 Standards

GeneRuler™ 1kb DNA Ladder	Fermentas
PageRuler™ Unstained Protein Ladder	Fermentas
PageRuler™ Prestained Protein Ladder	Fermentas

4.2.9 Columns

Affinity chromatography	HisTrap^{TM} HP 5ml (GE Healthcare)
Ion exchange chromatography:	HiTrap ANX FF (high sub) 1 ml (GE Healthcare)
	HiTrap ANX FF (high sub) 5 ml (GE Healthcare)
Size exclusion chromatography:	*Superose™ 6 10/30 GL* (Säulenvolumen 24 ml) (Amersham Biosciences)
Desalting coloums	PD-10 desalting columns (GE Healthcare)

4.3 Primer

Sequencing primers

*Hs*TPPII

H1: 5′ CCAACAACGGCTCTTCTCAAGC 3′

H2: 5′ CTAAGCACAATGGAAACAGG 3′

H3: 5′ GGACGCAGCTGATGAATGG 3′

H4: 5′ CAGTGTCCCAGCCATTTGG 3′

H5: 5′ GCTTTTCCTGTCCTAGGTGG 3′

H6: 5′ GACCAGAACAAAAGACAGATGG 3′

H7: 5′ GAATGGCAGCAAAGATAAGG 3′

H8: 5′ CAAGACGGAGCCATTTCCAC 3′

*Dm*TPPII

TP1: 5′ GACGAGAACGGCAACATTAAGGCC 3′

TP2: 5′ GATTGCATCCTTTTTCCCACGGCC 3′

TP3: 5′ GAACTATGTCGCGATGGCAGACGC 3′

TP4: 5′ TCCGTGCCACAGTTTACTATGAGC 3′

TP5: 5′ ATAGAGCCCATCTTCTACAATGAC 3′

Tp6: 5′ GACTTCATCCTGGTGCCAGAACGT 3′

TP7: 5′ CCGACCGAGGCCAAGATCTCGCCG 3′

TP8: 5′ CTCACCCTTGATTTCTATGAGAAC 3′

TP9: 5′ CCTGTGGACAGCAGTGGGAGTCCC 3′

TP10:5′ GCAGCCAAGATAAAGACCAACATG 3′

Mutational primers

*Hs*TPPII

1. **ΔL2 (ΔG429-N446)**
   `5'-gagtatcagtgcgccaggaggaacatctatgtctt-3'`
   `5'-aagacatagatgttcctcctggcgcactgatactc-3'`

2. **I431A**
   `5'-tgcgccaggaggagccgctgcttctgttcctaac-3'`
   `5'-gttaggaacagaagcagcggctcctcctggcgca-3'`

3. **S433A**
   `5'-aggaggagccattgctgctgttcctaactggac-3'`
   `5'-gtccagttaggaacagcagcaatggctcctcct-3'`

4. **V434A**
   `5'-ggagccattgcttctgctcctaactggacactg-3'`
   `5'-cagtgtccagttaggagcagaagcaatggctcc-3'`

5. **N436A**
   `5'-gccattgcttctgttcctgcctggacactgagagggac-3'`
   `5'-gtccctctcagtgtccaggcaggaacagaagcaatggc-3'`

6. **W437A**
   `5'-ttgcttctgttcctaacgcgacactgagagggacgc-3'`
   `5'-gcgtccctctcagtgtcgcgttaggaacagaagcaa-3'`

7. **T438A**
   `5'-tctgttcctaactgggcactgagagggacgc-3'`
   `5'-gcgtccctctcagtgcccagttaggaacaga-3'`

8. **L439A**
   `5'-tgttcctaactggacagcgagagggacgcagctg-3'`
   `5'-cagctgcgtccctctcgctgtccagttaggaaca-3'`

9. **R440A**
   `5'-tcctaactggacactggcagggacgcagctgatg-3'`
   `5'-catcagctgcgtccctgccagtgtccagttagga-3'`

10. **T442A**
    `5'-tggacactgagaggggcgcagctgatgaatg-3'`
    `5'-cattcatcagctgcgcccctctcagtgtcca-3'`

11. **Q443A**
    `5'-ggacactgagagggacggcgctgatgaatggaacat-3'`
    `5'-atgttccattcatcagcgccgtccctctcagtgtcc-3'`

12. **L444A**
    `5'-gacactgagagggacgcaggcgatgaatggaacatctatg-3'`
    `5'-catagatgttccattcatcgcctgcgtccctctcagtgtc-3'`

13. **M445A**
    `5'-ctgagagggacgcagctggcgaatggaacatctatgtc-3'`
    `5'-gacatagatgttccattcgccagctgcgtccctctcag-3'`

14. **N446A**
    `5'-gagagggacgcagctgatggctggaacatctatgtcttcc-3'`
    `5'-ggaagacatagatgttccagccatcagctgcgtccctctc-3'`

15. ΔL1 (ΔP389-N405)
5'-gtgataggtgttggtgcttatgtttctacttggtcttctag-3'
5'-ctagaagaccaagtagaaacataagcaccaacacctatcac-3'

16. V393A
5'-gtttctcctgatatgatggctgctgagtattcactgaga-3'
5'-tctcagtgaatactcagcagccatcatatcaggagaaac-3'

17. E395A
5'-cctgatatgatggttgctgcgtattcactgagagagaaa-3'
5'-tttctctctcagtgaatacgcagcaaccatcatatcagg-3'
18. Y396A
5'-cctgatatgatggttgctgaggcttcactgagagagaaattacc-3'
5'-ggtaatttctctctcagtgaagcctcagcaaccatcatatcagg-3'

19. S397A
5'-gatatgatggttgctgagtatgcactgagagagaaattacct-3'
5'-aggtaatttctctctcagtgcatactcagcaaccatcatatc-3'

20. L398A
5'-atatgatggttgctgagtattcagcgagagagaaattacctgcaaatc-3'
5'-gatttgcaggtaatttctctctcgctgaatactcagcaaccatcatat-3'

21. R399A
5'-gatggttgctgagtattcactggcagagaaattacctgcaaatcaa-3'
5'-ttgatttgcaggtaatttctctgccagtgaatactcagcaaccatc-3'

22. E400A
5'-gttgctgagtattcactgagagcgaaattacctgcaaatcaatat-3'
5'-atattgatttgcaggtaatttcgctctcagtgaatactcagcaac-3'

23. K401A
5'-gttgctgagtattcactgagagaggcattacctgcaaatcaatatacttg-3'
5'-caagtatattgatttgcaggtaatgcctctctcagtgaatactcagcaac-3'

24. L402A
5'-gatggttgctgagtattcactgagagagaaagcacctgcaaatcaatat-3'
5'-atattgatttgcaggtgctttctctctcagtgaatactcagcaaccatc-3'

25. P403A
5'-gttgctgagtattcactgagagagaaattagctgcaaatcaatatac-3'
5'-gtatattgatttgcagctaatttctctctcagtgaatactcagcaac-3'

26. N405A
5'-gtattcactgagagagaaattacctgcagctcaatatacttggtcttctag-3'
5'-ctagaagaccaagtatattgagctgcaggtaatttctctctcagtgaatac-3'

27. L585D/L587D
5'-catcttgggttcagtgtcccagccatgacgaagacatgaatcaatgtagacacataaaca-3'
5'-tgtttatgtgtctacattgattcatgtcttcgtcatggctgggacactgaacccaagatg-3'

28. D586K
5'-tcagtgtcccagccatttgaaactcatgaatcaatgtag-3'
5'-ctacattgattcatgagtttcaaatggctgggacactga-3'

29. R593E
5'-ccagccatttggaactcatgaatcaatgtgaacacataaacatacgtg-3'
5'-cacgtatgtttatgtgttcacattgattcatgagttccaaatggctgg-3'

30. K564A
5'-cggagaacacagaaaactctgaagcaatatcccttcagcttcatttag-3'
5'-ctaaatgaagctgaagggatattgcttcagagttttctgtgttctccg-3'

31. I565A
5'-ccggagaacacagaaaactctgaaaaagcatcccttcagcttcatttag-3'
5'-ctaaatgaagctgaagggatgctttttcagagttttctgtgttctccgg-3'

32. S566A
5'-cggagaacacagaaaactctgaaaaaatagcccttcagcttcatt-3'
5'-aatgaagctgaagggctattttttcagagttttctgtgttctccg-3'

33. L567A
5'-cacagaaaactctgaaaaaatatccgctcagcttcatttagctctgacttc-3'
5'-gaagtcagagctaaatgaagctgagcggatattttttcagagttttctgtg-3'

34. Q568A
5'-cagaaaactctgaaaaaatatcccttgcgcttcatttagctctgacttcaa-3'
5'-ttgaagtcagagctaaatgaagcgcaagggatattttttcagagttttctg-3’

*Dm*TPPII

1. Δ448-449
5'-gagccattgcgtccgtgtttactatgagcaagtc-3'
5'-gacttgctcatagtaaacacggacgcaatggctc-3'

2. V447T/Δ448-449
5'-ggcggagccattgcgtccacgtttactatgagcaagtc-3'
5'-gacttgctcatagtaaacgtggacgcaatggctccgcc-3'

3. Δ448-449/T451P
5'-ccattgcgtccgtgtttcctatgagcaagtcccag-3'
5'-ctgggacttgctcataggaaacacggacgcaatgg-3'

4. V447T/Δ448-449/T451P
5'-gcggagccattgcgtccacgtttcctatgagcaagtcccag-3'
5'-ctgggacttgctcataggaaacgtggacgcaatggctccgc-3'

5. A465S
5'-taccagcatggcgtcacctcacgtcgc-3'
5'-gcgacgtgaggtgacgccatgctggta-3'

6. V472A, L475I, I476L
5'-gccggcgcagcggcgctgatcctctccggtct-3'
5'-agaccggagaggatcagcgccgctgcgccggc-3'

7. G442A, A443G, I444V, A445Y
5'-cgttaccgtatgcgctccgggcgcaggcgtgtactccgtgtttactatgagcaagtc-3'
5'-gacttgctcatagtaaacacggagtacacgcctgcgcccggagcgcatacggtaacg-3'

8. V447T, F450Y, T451P
5'-gctccgggcgcaggcgtgtactccacttacccaatgagcaagtcccagctgatgaac-3'
5'-gttcatcagctgggacttgctcattgggtaagtggagtacacgcctgcgcccggagc-3'

9. M452T, K454T, S455V
5'-ggcgcaggcgtgtactccacttacccaaccagcacttatcagctgatgaacggt-3'
5'-accgttcatcagctgataagtgctggttgggtaagtggagtacacgcctgcgcc-3'

10. Q456A, L457T, M458L
5'-gtactccacttacccaaccagcacttatgcaacattgaacggtaccagcatggcggcacc-3'
5'-ggtgccgccatgctggtaccgttcaatgttgcataagtgctggttgggtaagtggagtac-3'

11. ΔL2 (ΔG442-N459)
5'-atgcgctccgggcggtaccagcatgg-3'
5'-ccatgctggtaccgcccggagcgcat-3'

12. I444A
5'-ccgggcggagccgctgcgtccgtgcc-3'
5'-ggcacggacgcagcggctccgcccgg-3'

13. S446A
5'-cggagccattgcggccgtgccacagtt-3'
5'-aactgtggcacggccgcaatggctccg-3'

14. V447A
5'-ggagccattgcgtccgcgccacagtttactatg-3'
5'-catagtaaactgtggcgcggacgcaatggctcc-3'

15. Q449A
5'-gccattgcgtccgtgccagcgtttactatgagcaagtc-3'
5'-gacttgctcatagtaaacgctggcacggacgcaatggc-3'

16. F450A
5'-ttgcgtccgtgccacaggctactatgagcaagtccc-3'
5'-gggacttgctcatagtagcctgtggcacggacgcaa-3'

17. T451A
5'-gtccgtgccacagtttgctatgagcaagtccca-3'
5'-tgggacttgctcatagcaaactgtggcacggac-3'

18. M452A
5'-ccgtgccacagtttactgcgagcaagtcccagctga-3'
5'-tcagctgggacttgctcgcagtaaactgtggcacgg-3'

19. S453A
5'-cgtgccacagtttactatggccaagtcccagctgatga-3'
5'-tcatcagctgggacttggccatagtaaactgtggcacg-3'

20. K454A
5'-ccacagtttactatgagcgcgtcccagctgatgaacgg-3'
5'-ccgttcatcagctgggacgcgctcatagtaaactgtgg-3'

21. S455A
5'-agtttactatgagcaaggcccagctgatgaacggt-3'
5'-accgttcatcagctgggccttgctcatagtaaact-3'

22. Q456A
5'-gtttactatgagcaagtccgcgctgatgaacggtaccagc-3'
5'-gctggtaccgttcatcagcgcggacttgctcatagtaaac-3'

23. L457A
5'-ctatgagcaagtcccaggcgatgaacggtaccagca-3'
5'-tgctggtaccgttcatcgcctgggacttgctcatag-3'

24. M458A
5'-gagcaagtcccagctggcgaacggtaccagcatg-3'
5'-catgctggtaccgttcgccagctgggacttgctc-3'

25. N459A
5'-caagtcccagctgatggccggtaccagcatggcg-3'
5'-cgccatgctggtaccggccatcagctgggacttg-3'

26. ΔL1 (ΔP402-P416)
5'-cgtgggcgcgtacgtatcagggaacgtgt-3'
5'-acacgttccctgatacgtacgcgcccacg-3'

27. L603E/L605E
5'-ggtgcagtgtggagctttcgaggatgaaagctatggcacccgctcc-3'
5'-ggagcgggtgccatagctttcatcctcgaaagctccacactgcacc-3'

28. D604K
5'-agtgtggagctttcttgaatctcagctatggcacc-3'
5'-ggtgccatagctgagattcaagaaagctccacact-3

29. R610E
5'-ctcagctatggcaccgactccattgccgtgcg-3'
5'-cgcacggcaatggagtcggtgccatagctgag-3'

30. S446Stop
5'-ggcggagccattgcgtaggtgccacagtttacta-3'
5'-tagtaaactgtggcacctacgcaatggctccgcc-3'

31. F450Stop
5'-agccattgcgtccgtgccacagtagactatgagcaag-3'
5'-cttgctcatagtctactgtggcacggacgcaatggct-3'

32. S455Stop
5'-cagtttactatgagcaagtagcagctgatgaacggtacca-3'
5'-tggtaccgttcatcagctgctacttgctcatagtaaactg-3'

33. F162Stop
5'-ccagtcgcaagattgttgaataggagtcacaaaatccaggaga-3'
5'-tctcctggattttgtgactcctattcaacaatcttgcgactgg-3'

34. F248Bpa
5'-acccgcaatgtggacgactagctttccatatcggtaaacg-3'
5'-cgtttaccgatatggaaagctagtcgtccacattgcgggt-3'

35. F582Bpa
5'-gcggatcccaaggacaagtagaacttcaatgtacggctaa-3'
5'-ttagccgtacattgaagttctacttgtccttgggatccgc-3'

36. F602Bpa
5'-gggtgcagtgtggagcttagttggatctcagctatg-3'
5'-catagctgagatccaactaagctccacactgcaccc-3'

37. Y607Bpa
5'-agctttcttggatctcagctagggcacccgctc-3'
5'-gagcgggtgccctagctgagatccaagaaagct-3'

4.4 Settings for the 3D-reconstructions

4.4.1 All particles

Iteration	Binning	Sampling	Ang. Change	5D search	Sym	additional
1	2	10	1000	10	c2	
2	2	10	1000	10	c2	
3	2	5	20	10	c2	
4	2	5	20	10	c2	
5	2	2	10	5	c2	
6	2	2	10	5	c2	
7	1	10	20	10	c2	
8	1	5	10	5	c2	
9	1	5	10	5	c2	
10	1	2	4	2	c2	
11	1	2	4	2	c2	
12	1	0.5	2	1	c2	
13	0	10	20	5	c2	
14	0	5	10	2	c2	
15	0	5	10	1	c2	
16	0	2	4	1	c2	
17	0	2	4	1	c2	
18	0	0.5	2	1	c2	
19	0	0.5	2	1	d2	
20	0	0.5	2	1	d2	
21	0	5	10	1	d2	
22	0	2	4	1	d2	
23	0	2	4	1	d2	
24	0	2	4	1	d2	
25	0	0.5	2	1	d2	
26	0	0.5	2	1	d2	
27	0	0.5	1	1	d2	
28	0	0.2	1	1	d2	
29	0	0.5	1	1	d2	
30	0	0.5	1	1	d2	
31	0	0.5	1	1	d2	

Iteration	Binning	Sampling	Ang. Change	5D search	Sym	additional
32	0	0.5	1	1	d2	
33	0	0.4	0.8	1	d2	
34	0	0.4	0.8	1	d2	
35	0	0.3	0.6	1	d2	
36	0	0.3	0.6	1	d2	
37	0	0.5	1	1	d2	ctf-groups
38	0	0.5	1	1	d2	ctf-groups
39	0	0.5	1	1	d2	ctf-groups
40	0	0.5	1	1	d2	ctf-groups
41	0	2	4	2	d2	mtf
42	0	1	4	1	d2	mtf
43	0	0.5	2	1	d2	mtf
44	0	0.5	2	1	d2	mtf
45	0	0.5	1	1	d2	mtf
46	0	0.3	1	1	d2	mtf
47	0	0.3	0.6	1	d2	mtf
48	0	0.3	0.6	1	d2	mtf
49	0	0.3	0.6	1	d2	mtf
50	0	0.2	0.4	0	d2	mtf
51	0	0.3	0.6	0	d2	mtf
52	0	0.3	0.6	0	d2	mtf
53	0	1	5	0	d2	mtf
54	0	1	5	0	d2	mtf
55	0	1	5	0	d2	mtf
56	0	0.5	5	0	d2	mtf
57	0	0.5	5	0	d2	mtf
58	0	0.3	3	0	d2	mtf
59	0	0.3	3	0	d2	mtf
60	0	0.2	3	0	d2	mtf
61	0	0.2	3	0	d2	mtf
62	0	0.1	1	0	d2	mtf
63	0	0.1	1	0	d2	mtf

4.4.2 *Hs*TPPII$_9$

Iteration	Binning	Sampling	Ang. Change	5D search	Sym	additional
1	0	10	20	40	c2	
2	0	10	20	40	c2	
3	0	5	10	20	c2	
4	0	5	10	10	c2	
5	0	2	4	10	c2	
6	0	2	4	5	c2	
7	0	0.5	2	5	d2	
8	0	0.5	2	5	d2	
9	0	0.5	1	5	d2	ctf-groups
10	0	0.5	1	1	d2	ctf-groups
11	0	2	4	1	d2	mtf
12	0	1	2	1	d2	mtf
13	0	0.5	1	1	d2	mtf
14	0	0.5	1	1	d2	mtf
15	0	0.2	0.4	1	d2	mtf
16	0	0.2	0.4	1	d2	mtf
17	0	0.1	0.2	1	d2	mtf
18	0	0.1	0.2	1	d2	mtf
19	0	0.1	0.2	0	d2	mtf

4.4.3 *Hs*TPPII$_8$

Iteration	Binning	Sampling	Ang. Change	5D search	Sym	additional
1	0	10	20	40	c2	
2	0	10	20	40	c2	
3	0	5	10	20	c2	
4	0	5	10	20	c2	
5	0	2	4	10	c2	
6	0	2	4	10	c2	
7	0	0.5	2	5	c2	ctf-groups
8	0	0.5	2	5	d2	ctf-groups
9	0	0.5	2	5	d2	mtf
10	0	2	6	2	d2	mtf
11	0	2	6	2	d2	mtf
12	0	1	5	1	d2	mtf
13	0	1	5	1	d2	mtf
14	0	1	4	1	d2	mtf
15	0	1	4	1	d2	mtf
16	0	0.5	2	0	d2	mtf
17	0	0.5	2	0	d2	mtf
18	0	0.3	1	1	d2	mtf
19	0	0.3	1	1	d2	mtf
20	0	0.2	0.4	1	d2	mtf
21	0	0.2	0.4	1	d2	mtf
22	0	0.1	0.2	1	d2	mtf
23	0	0.1	0.2	1	d2	mtf
24	0	0.1	0.2	0	d2	mtf
25	0	0.1	0.2	0	d2	mtf

5 References

Addlagatta, A., Gay, L., and Matthews, B.W. (2006). Structure of aminopeptidase N from Escherichia coli suggests a compartmentalized, gated active site. Proc Natl Acad Sci U S A *103*, 13339-13344.

Balow, R.M., Ragnarsson, U., and Zetterqvist, O. (1983). Tripeptidyl aminopeptidase in the extralysosomal fraction of rat liver. J Biol Chem *258*, 11622-11628.

Balow, R.M., Tomkinson, B., Ragnarsson, U., and Zetterqvist, O. (1986). Purification, substrate specificity, and classification of tripeptidyl peptidase II. J Biol Chem *261*, 2409-2417.

Barrett, A.J., Rawling, N.D., and Woessner, J.F., eds. (2004). Handbook of Proteolytic Enzymes, 2 edn (Elsevier Ltd).

Baumeister, W., Walz, J., Zühl, F., and Seemüller, E. (1998). The proteasome: Paradigm of a self-compartmentalizing protease. Cell *92*, 367-380.

Beninga, J., Rock, K.L., and Goldberg, A.L. (1998). Interferon-gamma can stimulate post-proteasomal trimming of the N terminus of an antigenic peptide by inducing leucine aminopeptidase. J Biol Chem *273*, 18734-18742.

Bermingham, N.A., McKay, T., Hoyle, J., Hernandez, D., Martin, J.E., and Fisher, E.M. (1996). The gene encoding tripeptidyl peptidase II maps to chromosome 1 in the mouse. Mamm Genome *7*, 390.

Bode, W., Papamokos, E., and Musil, D. (1987). The high-resolution X-ray crystal structure of the complex formed between subtilisin Carlsberg and eglin c, an elastase inhibitor from the leech Hirudo medicinalis. Structural analysis, subtilisin structure and interface geometry. Eur J Biochem *166*, 673-692.

Book, A.J., Yang, P.Z., Scalf, M., Smith, L.M., and Vierstra, R.D. (2005). Tripeptidyl peptidase II. An oligomeric protease complex from Arabidopsis. Plant Physiol *138*, 1046-1057.

Borissenko, L., and Groll, M. (2005). Crystal structure of TET protease reveals complementary protein degradation pathways in prokaryotes. J Mol Biol *346*, 1207-1219.

Brandstetter, H., Kim, J.S., Groll, M., Gottig, P., and Huber, R. (2002). Structural basis for the processive protein degradation by tricorn protease. Biol Chem *383*, 1157-1165.

Brandstetter, H., Kim, J.S., Groll, M., and Huber, R. (2001). Crystal structure of the tricorn protease reveals a protein disassembly line. Nature *414*, 466-470.

Burri, L., Servis, C., Chapatte, L., and Levy, F. (2002). A recyclable assay to analyze the NH(2)-terminal trimming of antigenic peptide precursors. Protein Expr Purif *26*, 19-27.

Chen, D., Frezza, M., Schmitt, S., Kanwar, J., and Q, P.D. (2011). Bortezomib as the first proteasome inhibitor anticancer drug: current status and future perspectives. Curr Cancer Drug Targets *11*, 239-253.

Chen, P., and Hochstrasser, M. (1996). Autocatalytic subunit processing couples active site formation in the 20S proteasome to completion of assembly. Cell *86*, 961-972.

Chin, J.W., Martin, A.B., King, D.S., Wang, L., and Schultz, P.G. (2002). Addition of a photocrosslinking amino acid to the genetic code of Escherichiacoli. Proc Natl Acad Sci U S A *99*, 11020-11024.

Chuang, C.K., Rockel, B., Seyit, G., Walian, P.J., Schonegge, A.M., Peters, J., Zwart, P.H., Baumeister, W., and Jap, B.K. (2010). Hybrid molecular structure of the giant protease tripeptidyl peptidase II. Nat Struct Mol Biol *17*, 990-996.

Duensing, S., Darr, S., Cuevas, R., Melquiot, N., Brickner, A.G., Duensing, A., and Munger, K. (2010). Tripeptidyl Peptidase II Is Required for c-MYC-Induced Centriole Overduplication and a Novel Therapeutic Target in c-MYC-Associated Neoplasms. Genes Cancer *1*, 883-892.

Edgington, L.E., Verdoes, M., and Bogyo, M. (2011). Functional imaging of proteases: recent advances in the design and application of substrate-based and activity-based probes. Curr Opin Chem Biol.

Engel, M., Hoffmann, T., Wagner, L., Wermann, M., Heiser, U., Kiefersauer, R., Huber, R., Bode, W., Demuth, H.U., and Brandstetter, H. (2003). The crystal structure of dipeptidyl peptidase IV (CD26) reveals its functional regulation and enzymatic mechanism. Proc Natl Acad Sci U S A *100*, 5063-5068.

Firat, E., Huai, J., Saveanu, L., Gaedicke, S., Aichele, P., Eichmann, K., van Endert, P., and Niedermann, G. (2007). Analysis of direct and cross-presentation of antigens in TPPII knockout mice. J Immunol *179*, 8137-8145.

Firat, E., Tsurumi, C., Gaedicke, S., Huai, J., and Niedermann, G. (2009). Tripeptidyl peptidase II plays a role in the radiation response of selected primary cell types but not based on nuclear translocation and p53 stabilization. Cancer Res *69*, 3325-3331.

Fonovic, M., and Bogyo, M. (2008). Activity-based probes as a tool for functional proteomic analysis of proteases. Expert Rev Proteomics *5*, 721-730.

Gamble, M., Kunze, G., Dodson, E.J., Wilson, K.S., and Jones, D.D. (2011). Regulation of an intracellular subtilisin protease activity by a short propeptide sequence through an original combined dual mechanism. Proc Natl Acad Sci U S A *108*, 3536-3541.

Gao, G., Zhang, J., Si, X., Wong, J., Cheung, C., McManus, B., and Luo, H. (2008). Proteasome inhibition attenuates coxsackievirus-induced myocardial damage in mice. Am J Physiol Heart Circ Physiol *295*, H401-408.

Gavioli, R., Frisan, T., Vertuani, S., Bornkamm, G.W., and Masucci, M.G. (2001). c-myc overexpression activates alternative pathways for intracellular proteolysis in lymphoma cells. Nat Cell Biol *3*, 283-288.

Geier, E., Pfeifer, G., Wilm, M., Lucchiari-Hartz, M., Baumeister, W., Eichmann, K., and Niedermann, G. (1999). A giant protease with potential to substitute for some functions of the proteasome. Science *283*, 978-981.

Glas, R., Bogyo, M., McMaster, J.S., Gaczynska, M., and Ploegh, H.L. (1998). A proteolytic system that compensates for loss of proteasome function. Nature *392*, 618-622.

Glickman, M.H., and Ciechanover, A. (2002). The ubiquitin-proteasome proteolytic pathway: destruction for the sake of construction. Physiol Rev *82*, 373-428.

Glickman, M.H., Rubin, D.M., Coux, O., Wefes, I., Pfeifer, G., Cjeka, Z., Baumeister, W., Fried, V.A., and Finley, D. (1998). A subcomplex of the proteasome regulatory particle required for ubiquitin-conjugate degradation and related to the COP9-signalosome and eIF3. Cell *94*, 615-623.

Goettig, P., Groll, M., Kim, J.S., Huber, R., and Brandstetter, H. (2002). Structures of the tricorn-interacting aminopeptidase F1 with different ligands explain its catalytic mechanism. The EMBO journal *21*, 5343-5352.

Harris, J., and Tomkinson, B. (1990). Electron microscopical and biochemical studies on the oligomeric state of human erythrocyte tripeptidyl peptidase II. Micron Microsc Acta *21*, 77-89.

Hasselgren, P.O., and Fischer, J.E. (2001). Muscle cachexia: current concepts of intracellular mechanisms and molecular regulation. Ann Surg *233*, 9-17.

Heal, W.P., Dang, T.H., and Tate, E.W. (2011). Activity-based probes: discovering new biology and new drug targets. Chem Soc Rev *40*, 246-257.

Hedstrom, L. (2002). Serine protease mechanism and specificity. Chem Rev *102*, 4501-4524.

Hegde, A.N., and Upadhya, S.C. (2011). Role of ubiquitin-proteasome-mediated proteolysis in nervous system disease. Biochim Biophys Acta *1809*, 128-140.

Hegerl, R. (1996). The EM Program Package: A Platform for Image Processing in Biological Electron Microscopy. J Struct Biol *116*, 30-34.

Hilbi, H., Jozsa, E., and Tomkinson, B. (2002). Identification of the catalytic triad in tripeptidyl-peptidase II through site-directed mutagenesis. Biochim Biophys Acta *1601*, 149-154.

Hilbi, H., Moss, J.E., Hersh, D., Chen, Y., Arondel, J., Banerjee, S., Flavell, R.A., Yuan, J., Sansonetti, P.J., and Zychlinsky, A. (1998). Shigella-induced apoptosis is dependent on caspase-1 which binds to IpaB. J Biol Chem *273*, 32895-32900.

Hilbi, H., Puro, R.J., and Zychlinsky, A. (2000). Tripeptidyl peptidase II promotes maturation of caspase-1 in Shigella flexneri-induced macrophage apoptosis. Infection and immunity *68*, 5502-5508.

Hong, X., Lei, L., and Glas, R. (2003). Tumors acquire inhibitor of apoptosis protein (IAP)-mediated apoptosis resistance through altered specificity of cytosolic proteolysis. J Exp Med *197*, 1731-1743.

Huai, J., Firat, E., Nil, A., Million, D., Gaedicke, S., Kanzler, B., Freudenberg, M., van Endert, P., Kohler, G., Pahl, H.L., *et al.* (2008). Activation of cellular death programs associated with immunosenescence-like phenotype in TPPII knockout mice. Proc Natl Acad Sci U S A *105*, 5177-5182.

Huang, Z., Feng, Y., Chen, D., Wu, X., Huang, S., Wang, X., Xiao, X., Li, W., Huang, N., Gu, L., *et al.* (2008). Structural basis for activation and inhibition of the secreted chlamydia protease CPAF. Cell Host Microbe *4*, 529-542.

Kawahara, M., York, I.A., Hearn, A., Farfan, D., and Rock, K.L. (2009). Analysis of the role of tripeptidyl peptidase II in MHC class I antigen presentation in vivo. J Immunol *183*, 6069-6077.

Kessel, M., Maurizi, M.R., Kim, B., Kocsis, E., Trus, B.L., Singh, S.K., and Steven, A.C. (1995). Homology in structural organization between E. coli ClpAP protease and the eukaryotic 26 S proteasome. J Mol Biol *250*, 587-594.

Kisselev, A.F., Akopian, T.N., Woo, K.M., and Goldberg, A.L. (1999). The sizes of peptides generated from protein by mammalian 26 and 20 S proteasomes. Implications for understanding the degradative mechanism and antigen presentation. J Biol Chem *274*, 3363-3371.

Klein, G. (1983). Specific chromosomal translocations and the genesis of B-cell-derived tumors in mice and men. Cell *32*, 311-315.

Krissinel, E., and Henrick, K. (2007). Inference of macromolecular assemblies from crystalline state. J Mol Biol *372*, 774-797.

Krojer, T., Sawa, J., Huber, R., and Clausen, T. (2010). HtrA proteases have a conserved activation mechanism that can be triggered by distinct molecular cues. Nat Struct Mol Biol *17*, 844-852.

Lazure, C. (2002). The peptidase zymogen proregions: nature's way of preventing undesired activation and proteolysis. Curr Pharm Des *8*, 511-531.

Lees, T., Lauffart, B., McDermott, J., Gibson, A., and Mantle, D. (1990). Purification and characterization of tripeptidyl-aminopeptidase from human cerebral cortex. Biochem Soc Trans *18*, 667.

Levy, F., Burri, L., Morel, S., Peitrequin, A.L., Levy, N., Bachi, A., Hellman, U., Van den Eynde, B.J., and Servis, C. (2002). The final N-terminal trimming of a subaminoterminal proline-containing HLA class I-restricted antigenic peptide in the cytosol is mediated by two peptidases. J Immunol *169*, 4161-4171.

Lindas, A.C., Eriksson, S., Jozsa, E., and Tomkinson, B. (2008). Investigation of a role for Glu-331 and Glu-305 in substrate binding of tripeptidyl-peptidase II. Biochim Biophys Acta *1784*, 1899-1907.

Lucic, V., Kossel, A.H., Yang, T., Bonhoeffer, T., Baumeister, W., and Sartori, A. (2007). Multiscale imaging of neurons grown in culture: from light microscopy to cryo-electron tomography. J Struct Biol *160*, 146-156.

Lucic, V., Leis, A., and Baumeister, W. (2008). Cryo-electron tomography of cells: connecting structure and function. Histochem Cell Biol *130*, 185-196.

Ludtke, S.J., Baldwin, P.R., and Chiu, W. (1999). EMAN: semiautomated software for high-resolution single-particle reconstructions. J Struct Biol *128*, 82-97.

Lupas, A., Flanagan, J.M., Tamura, T., and Baumeister, W. (1997). Self-compartmentalizing proteases. Trends Biochem Sci *22*, 399-404.

Macpherson, E., Tomkinson, B., Balow, R.M., Hoglund, S., and Zetterqvist, O. (1987). Supramolecular Structure of Tripeptidyl Peptidase-Ii from Human-Erythrocytes as Studied by Electron-Microscopy, and Its Correlation to Enzyme-Activity. Biochem J *248*, 259-263.

Mastronarde, D.N. (2005). Automated electron microscope tomography using robust prediction of specimen movements. J Struct Biol *152*, 36-51.

Masucci, M.G. (2004). Epstein-Barr virus oncogenesis and the ubiquitin-proteasome system. Oncogene *23*, 2107-2115.

McKay, R.M., McKay, J.P., Suh, J.M., Avery, L., and Graff, J.M. (2007). Tripeptidyl peptidase II promotes fat formation in a conserved fashion. EMBO Rep *8*, 1183-1189.

Meiners, S., Heyken, D., Weller, A., Ludwig, A., Stangl, K., Kloetzel, P.M., and Kruger, E. (2003). Inhibition of proteasome activity induces concerted expression of proteasome genes and de novo formation of Mammalian proteasomes. J Biol Chem *278*, 21517-21525.

Mitsiades, N., Mitsiades, C.S., Poulaki, V., Chauhan, D., Fanourakis, G., Gu, X., Bailey, C., Joseph, M., Libermann, T.A., Treon, S.P., *et al.* (2002). Molecular sequelae of proteasome inhibition in human multiple myeloma cells. Proc Natl Acad Sci U S A *99*, 14374-14379.

Nickell, S., Forster, F., Linaroudis, A., Net, W.D., Beck, F., Hegerl, R., Baumeister, W., and Plitzko, J.M. (2005). TOM software toolbox: acquisition and analysis for electron tomography. J Struct Biol *149*, 227-234.

Nitsch, M., Klumpp, M., Lupas, A., and Baumeister, W. (1997). The thermosome: alternating alpha and beta-subunits within the chaperonin of the archaeon Thermoplasma acidophilum. J Mol Biol *267*, 142-149.

Nussbaum, A.K., Dick, T.P., Keilholz, W., Schirle, M., Stevanovic, S., Dietz, K., Heinemeyer, W., Groll, M., Wolf, D.H., Huber, R.*, et al.* (1998). Cleavage motifs of the yeast 20S proteasome beta subunits deduced from digests of enolase 1. Proc Natl Acad Sci U S A *95*, 12504-12509.

Osmulski, P.A., and Gaczynska, M. (1998). A new large proteolytic complex distinct from the proteasome is present in the cytosol of fission yeast. Curr Biol *8*, 1023-1026.

Paschen, S.A., Christian, J.G., Vier, J., Schmidt, F., Walch, A., Ojcius, D.M., and Hacker, G. (2008). Cytopathicity of Chlamydia is largely reproduced by expression of a single chlamydial protease. J Cell Biol *182*, 117-127.

Penczek, P.A., Yang, C., Frank, J., and Spahn, C.M. (2006). Estimation of variance in single-particle reconstruction using the bootstrap technique. J Struct Biol *154*, 168-183.

Peters, J., Schönegge, A.M., Rockel, B., and Baumeister, W. (2011). Molecular ruler of tripeptidylpeptidase II: Mechanistic principle of exopeptidase selectivity. Biochem Biophys Res Co *414*, 209-214.

Pettersen, E.F., Goddard, T.D., Huang, C.C., Couch, G.S., Greenblatt, D.M., Meng, E.C., and Ferrin, T.E. (2004). UCSF Chimera--a visualization system for exploratory research and analysis. J Comput Chem *25*, 1605-1612.

Pickart, C.M., and Cohen, R.E. (2004). Proteasomes and their kin: Proteases in the machine age. Nat Rev Mol Cell B *5*, 177-187.

Preta, G., de Klark, R., Chakraborti, S., and Glas, R. (2010a). MAP kinase-signaling controls nuclear translocation of tripeptidyl-peptidase II in response to DNA damage and oxidative stress. Biochem Biophys Res Commun *399*, 324-330.

Preta, G., de Klark, R., Gavioli, R., and Glas, R. (2010b). The Enigma of Tripeptidyl-Peptidase II: Dual Roles in Housekeeping and Stress. J Oncol *2010*.

Preta, G., de Klark, R., and Glas, R. (2009). A role for nuclear translocation of tripeptidyl-peptidase II in reactive oxygen species-dependent DNA damage responses. Biochem Biophys Res Commun *389*, 575-579.

Princiotta, M.F., Schubert, U., Chen, W.S., Bennink, J.R., Myung, J., Crews, C.M., and Yewdell, J.W. (2001). Cells adapted to the proteasome inhibitor 4-hydroxy5-iodo-3-nitrophenylacetyl-Leu-Leu-leucinal-vinyl sulfone require enzymatically active proteasomes for continued survival. Proc Natl Acad Sci U S A *98*, 513-518.

Reits, E., Neijssen, J., Herberts, C., Benckhuijsen, W., Janssen, L., Drijfhout, J.W., and Neefjes, J. (2004). A major role for TPPII in trimming proteasomal degradation products for MHC class I antigen presentation. Immunity *20*, 495-506.

Renn, S.C., Tomkinson, B., and Taghert, P.H. (1998). Characterization and cloning of tripeptidyl peptidase II from the fruit fly, Drosophila melanogaster. J Biol Chem *273*, 19173-19182.

Rockel, B., Kopec, K.O., Lupas, A.N., and Baumeister, W. (2012). Structure and function of tripeptidyl peptidase II, a giant cytosolic protease. Biochim Biophys Acta *1824*, 237-245.

Rockel, B., Peters, J., Kühlmorgen, B., Glaeser, R.M., and Baumeister, W. (2002). A giant protease with a twist: the TPP II complex from Drosophila studied by electron microscopy. EMBO J *21*, 5979-5984.

Rockel, B., Peters, J., Müller, S.A., Seyit, G., Ringler, P., Hegerl, R., Glaeser, R.M., and Baumeister, W. (2005). Molecular architecture and assembly mechanism of Drosophila tripeptidyl peptidase II. Proc Natl Acad Sci U S A *102*, 10135-10140.

Rose, C., Vargas, F., Facchinetti, P., Bourgeat, P., Bambal, R.B., Bishop, P.B., Chan, S.M., Moore, A.N., Ganellin, C.R., and Schwartz, J.C. (1996). Characterization and inhibition of a cholecystokinin-inactivating serine peptidase. Nature *380*, 403-409.

Rosenthal, P.B., and Henderson, R. (2003). Optimal determination of particle orientation, absolute hand, and contrast loss in single-particle electron cryomicroscopy. J Mol Biol *333*, 721-745.

Rowe, M., Rowe, D.T., Gregory, C.D., Young, L.S., Farrell, P.J., Rupani, H., and Rickinson, A.B. (1987). Differences in B cell growth phenotype reflect novel patterns of Epstein-Barr virus latent gene expression in Burkitt's lymphoma cells. Embo J *6*, 2743-2751.

Saric, T., Chang, S.C., Hattori, A., York, I.A., Markant, S., Rock, K.L., Tsujimoto, M., and Goldberg, A.L. (2002). An IFN-gamma-induced aminopeptidase in the ER, ERAP1, trims precursors to MHC class I-presented peptides. Nat Immunol *3*, 1169-1176.

Schagger, H., and von Jagow, G. (1987). Tricine-sodium dodecyl sulfate-polyacrylamide gel electrophoresis for the separation of proteins in the range from 1 to 100 kDa. Anal Biochem *166*, 368-379.

Scheres, S.H., Gao, H., Valle, M., Herman, G.T., Eggermont, P.P., Frank, J., and Carazo, J.M. (2007). Disentangling conformational states of macromolecules in 3D-EM through likelihood optimization. Nat Methods *4*, 27-29.

Scheres, S.H., Nunez-Ramirez, R., Sorzano, C.O., Carazo, J.M., and Marabini, R. (2008). Image processing for electron microscopy single-particle analysis using XMIPP. Nat Protoc *3*, 977-990.

Schoehn, G., Vellieux, F.M., Asuncion Dura, M., Receveur-Brechot, V., Fabry, C.M., Ruigrok, R.W., Ebel, C., Roussel, A., and Franzetti, B. (2006). An archaeal peptidase assembles into two different quaternary structures: A tetrahedron and a giant octahedron. J Biol Chem *281*, 36327-36337.

Schönegge, A. (2007). Recombinant Expression and Characterization of the human Tripeptidyl Peptidase II. M. Sc., Technische Universität München

Schönegge, A., Villa, E., Förster, F., Hegerl, R., Peters, J., Baumeister, W., and Rockel, B. (2012). The structure of human Tripeptidyl peptidase II as deteremined by a hybrid approach. submitted.

Seifert, U., Maranon, C., Shmueli, A., Desoutter, J.F., Wesoloski, L., Janek, K., Henklein, P., Diescher, S., Andrieu, M., de la Salle, H.*, et al.* (2003). An essential role for tripeptidyl peptidase in the generation of an MHC class I epitope. Nat Immunol *4*, 375-379.

Seyit, G. (2006). Structural Studies of Tripeptidylpeptidase II: Expression and Crystallization Trials. Dr. rer. nat, Technische Universität München

Seyit, G., Rockel, B., Baumeister, W., and Peters, J. (2006). Size matters for the tripeptidylpeptidase II complex from Drosophila - The 6-MDa spindle form stabilizes the activated state. J Biol Chem *281*, 25723-25733.

Shastri, N., Cardinaud, S., Schwab, S.R., Serwold, T., and Kunisawa, J. (2005). All the peptides that fit: the beginning, the middle, and the end of the MHC class I antigen-processing pathway. Immunol Rev *207*, 31-41.

Siezen, R.J., de Vos, W.M., Leunissen, J.A., and Dijkstra, B.W. (1991). Homology modelling and protein engineering strategy of subtilases, the family of subtilisin-like serine proteinases. Protein Eng *4*, 719-737.

Siezen, R.J., and Leunissen, J.A. (1997). Subtilases: the superfamily of subtilisin-like serine proteases. Protein Sci *6*, 501-523.

Stavropoulou, V., Vasquez, V., Cereser, B., Freda, E., and Masucci, M.G. (2006). TPPII promotes genetic instability by allowing the escape from apoptosis of cells with activated mitotic checkpoints. Biochem Biophys Res Commun *346*, 415-425.

Stavropoulou, V., Xie, J., Henriksson, M., Tomkinson, B., Imreh, S., and Masucci, M.G. (2005). Mitotic infidelity and centrosome duplication errors in cells overexpressing tripeptidyl-peptidase II. Cancer Res *65*, 1361-1368.

Stoltze, L., Schirle, M., Schwarz, G., Schroter, C., Thompson, M.W., Hersh, L.B., Kalbacher, H., Stevanovic, S., Rammensee, H.G., and Schild, H. (2000). Two new proteases in the MHC class I processing pathway. Nat Immunol *1*, 413-418.

Tamura, T., Tamura, N., Cejka, Z., Hegerl, R., Lottspeich, F., and Baumeister, W. (1996). Tricorn protease - the core of a modular proteolytic system. Science *274*, 1385-1389.

Tiao, G., Fagan, J.M., Samuels, N., James, J.H., Hudson, K., Lieberman, M., Fischer, J.E., and Hasselgren, P.O. (1994). Sepsis stimulates nonlysosomal, energy-dependent proteolysis and increases ubiquitin mRNA levels in rat skeletal muscle. J Clin Invest *94*, 2255-2264.

Tomkinson, B. (1991). Nucleotide sequence of cDNA covering the N-terminus of human tripeptidyl peptidase II. Biomed Biochim Acta *50*, 727-729.

Tomkinson, B. (1999). Tripeptidyl peptidases: enzymes that count. Trends Biochem Sci *24*, 355-359.

Tomkinson, B. (2000). Association and dissociation of the tripeptidyl-peptidase II complex as a way of regulating the enzyme activity. Arch Biochem Biophys *376*, 275-280.

Tomkinson, B., ed. (2004). Handbook of Proteolytic Enzymes, 2 edn (Elsevier Ltd).

Tomkinson, B., and Jonsson, A.K. (1991). Characterization of cDNA for human tripeptidyl peptidase II: the N-terminal part of the enzyme is similar to subtilisin. Biochemistry *30*, 168-174.

Tomkinson, B., and Lindas, A.C. (2005). Tripeptidyl-peptidase II: a multi-purpose peptidase. Int J Biochem Cell Biol *37*, 1933-1937.

Tomkinson, B., Wernstedt, C., Hellman, U., and Zetterqvist, O. (1987). Active site of tripeptidyl peptidase II from human erythrocytes is of the subtilisin type. Proc Natl Acad Sci U S A *84*, 7508-7512.

van Endert, P. (2008). Role of tripeptidyl peptidase II in MHC class I antigen processing - the end of controversies? Eur J Immunol *38*, 609-613.

van Endert, P. (2011). Post-proteasomal and proteasome-independent generation of MHC class I ligands. Cell Mol Life Sci *68*, 1553-1567.

Vevodova, J., Gamble, M., Kunze, G., Ariza, A., Dodson, E., Jones, D.D., and Wilson, K.S. (2010). Crystal structure of an intracellular subtilisin reveals novel structural features unique to this subtilisin family. Structure *18*, 744-755.

Villasevil, E.M., Guil, S., Lopez-Ferreras, L., Sanchez, C., Del Val, M., and Anton, L.C. (2010). Accumulation of polyubiquitylated proteins in response to Ala-Ala-Phe-chloromethylketone is independent of the inhibition of Tripeptidyl peptidase II. Biochim Biophys Acta *1803*, 1094-1105.

Walz, J., Erdmann, A., Kania, M., Typke, D., Koster, A.J., and Baumeister, W. (1998). 26S proteasome structure revealed by three-dimensional electron microscopy. J Struct Biol *121*, 19-29.

Walz, J., Tamura, T., Tamura, N., Grimm, R., Baumeister, W., and Koster, A.J. (1997). Tricorn protease exists as an icosahedral supermolecule in vivo. Mol Cell *1*, 59-65.

Wang, E.W., Kessler, B.M., Borodovsky, A., Cravatt, B.F., Bogyo, M., Ploegh, H.L., and Glas, R. (2000). Integration of the ubiquitin-proteasome pathway with a cytosolic oligopeptidase activity. Proc Natl Acad Sci U S A *97*, 9990-9995.

Wang, J., Hartling, J.A., and Flanagan, J.M. (1997). The structure of ClpP at 2.3 A resolution suggests a model for ATP-dependent proteolysis. Cell *91*, 447-456.

Wilson, C., Gibson, A.M., and McDermott, J.R. (1993). Purification and Characterization of Tripeptidylpeptidase-Ii from Postmortem Human Brain. Neurochem Res *18*, 743-749.

Witt, S., Kwon, Y.D., Sharon, M., Felderer, K., Beuttler, M., Robinson, C.V., Baumeister, W., and Jap, B.K. (2006). Proteasome assembly triggers a switch required for active-site maturation. Structure *14*, 1179-1188.

Wray, C.J., Tomkinson, B., Robb, B.W., and Hasselgren, P.O. (2002). Tripeptidyl-peptidase II expression and activity are increased in skeletal muscle during sepsis. Biochem Biophys Res Commun *296*, 41-47.

Xu, Y., Nakajima, Y., Ito, K., Zheng, H., Oyama, H., Heiser, U., Hoffmann, T., Gartner, U.T., Demuth, H.U., and Yoshimoto, T. (2008). Novel inhibitor for prolyl tripeptidyl aminopeptidase from Porphyromonas gingivalis and details of substrate-recognition mechanism. J Mol Biol *375*, 708-719.

Yao, T., and Cohen, R.E. (2002). A cryptic protease couples deubiquitination and degradation by the proteasome. Nature *419*, 403-407.

York, I.A., Bhutani, N., Zendzian, S., Goldberg, A.L., and Rock, K.L. (2006). Tripeptidyl peptidase II is the major peptidase needed to trim long antigenic precursors, but is not required for most MHC class I antigen presentation. J Immunol *177*, 1434-1443.

York, I.A., Chang, S.C., Saric, T., Keys, J.A., Favreau, J.M., Goldberg, A.L., and Rock, K.L. (2002). The ER aminopeptidase ERAP1 enhances or limits antigen presentation by trimming epitopes to 8-9 residues. Nat Immunol *3*, 1177-1184.

York, I.A., Mo, A.X., Lemerise, K., Zeng, W., Shen, Y., Abraham, C.R., Saric, T., Goldberg, A.L., and Rock, K.L. (2003). The cytosolic endopeptidase, thimet oligopeptidase, destroys antigenic peptides and limits the extent of MHC class I antigen presentation. Immunity *18*, 429-440.

Yoshimura, T., Kameyama, K., Takagi, T., Ikai, A., Tokunaga, F., Koide, T., Tanahashi, N., Tamura, T., Cejka, Z., Baumeister, W., *et al.* (1993). Molecular Characterization of the 26S Proteasome Complex from Rat-Liver. J Struct Biol *111*, 200-211.

Yu, Y., Smith, D.M., Kim, H.M., Rodriguez, V., Goldberg, A.L., and Cheng, Y. (2010). Interactions of PAN's C-termini with archaeal 20S proteasome and implications for the eukaryotic proteasome-ATPase interactions. EMBO J *29*, 692-702.

Zhang, J., Wong, J., Gao, G., and Luo, H. (2011). Tripeptidyl peptidase II serves as an alternative to impaired proteasome to maintain viral growth in the host cells. FEBS Lett *585*, 261-265.

Zwickl, P., Baumeister, W., and Steven, A. (2000). Dis-assembly lines: the proteasome and related ATPase-assisted proteases. Curr Opin Struct Biol *10*, 242-250.

6 Abbreviations

2D	two-dimensional
3D	three-dimensional
Å	Ångström
aa	amino acid
ABP	activity-based probes
AAF-Amc	Ala-Ala-Phe-Amc
Amc	7-amino-4methylcoumarin
AS	ammoniumsulfate
BL	Burkitt's Lymphoma
Bpa	benzophenyllalanine
cbb	coomassie brilliant blue
° C	degree Celsius
ccc	cross correlation coefficient
CCD	charges-coupled device
Chlor	chloramphenicol
CPAF	Chlamydial protease-like activity factor
cryo-EM	cryo electron microscopy
ctf	contrast transfer function
DNA	deoxyribonucleic acid
*Dm*TPPII	*Drosophila melanogaster* TPPII
DTT	dithiothreitol
E. coli	*Escherichia coli*
EM	electronmicropscpy
FSC	Fourier shell correlation
g	standard gravity
g	gram
GFP	green fluorescence protein
H	hour
*Hs*TPPII	*Homo sapiens* TPPII
HtrA protease	high temperature requirement A protease
HMW	high molecular weight
IEX	ion exchange Chromatography
IMAC	immobilized metal ion affinity chromatography
IPTG	isopropyl β-D-1- thiolgalactopyranoside
Kan	kanamycin

kDa	kilo dalton
KO	kock-out
kV	kilo volts
LMW	low molecular weight
l	litre
M	molar
mM	millimolar
mg	milligram
ml	millilitre
µl	microlitre
min	minute
MBP	maltose binding protein
MDFF	molecular dynamics flexible fitting
ML3D	maximum likelihood in 3D
Mtf	modulation transfer function
nm	nanometer
ng	nanogram
pmol	picocolar
PCR	polymerase chain reaction
PEI	polyethyleneimine
Pro	proline
RMSF	root-mean-square fluctuation
S. pombe	*Schizosaccharomyces pombe*
sec	second
SDS	sodium dodecyl sulfate
SDS-PAGE	SDS-polyacrylamide gel electrophoresis
SEC	size exclusion chromatography
*Sp*TPPII	*Schizosaccharomyces pombe* TPPII
Thr	threonine
TPPII	tripeptidyl peptidase II
Tris	Tris(hydroxymethyl)-aminomethan
UV	ultraviolet
V	volts

7 Acknowledgements

ICH WIDME DIESE ARBEIT MEINEM VATER († 23.05.2011)

I DEDICATE THIS WORK TO MY FATHER († 23.05.2011)

First and foremost, I would like to thank **Prof. Wolfgang Baumeister** for having given me the opportunity to perform my Ph.D. thesis in his group and for his guidance and support throughout my studies.

My direct supervisors **Dr. Beate Rockel** and **Dr. Jürgen Peters** deserve my deepest gratitude for their constant support, for their help and inspiration as well as for the fruitful discussions and proof reading of the thesis.

Together with **Marietta**, the members of the TPPII group have always contributed to a great work atmosphere full of collegiality, mutual support and help, which I enjoyed very much throughout my graduate studies. I thank everyone for the stimulating conversations, suggestions and support during both the good and the hard times.

I also want to acknowledge all my **co-workers** and **office neighbors** who have created the great work atmosphere in the department by giving helpful ideas and offering a helping hand whenever needed.

Special thanks to **Birgit, Sabina, Inga and Tim** for their help with a lot of little things, which made my life a lot easier.

The collaboration with **Dr. Bing Jap** provided new insights into our work and I am very thankful for his ideas and his help during the various phases of my project.

Furthermore, I thank **Dr. Richard Leduc and his lab** for discussions and help by establishing a photocrosslinking technique in attempts to further study TPPII structure.

I am very grateful for the love, inspiration and support of **my family** that allowed me to start, continue and finish my studies and my thesis. Finally, I express my profound gratitude to Jan, **my partner and his family** have supported and encouraged me throughout my Ph.D. studies. Last but not least I would like to thank **old and new friends** for having great times with me after long lab days. Each of you has greatly enriched my life.

8 Publication List

- Chuang, C. K., Rockel, B., Seyit, G., Walian, P. J., **Schönegge, A. M.**, Peters, J., Zwart, P. H., Baumeister, W. and Jap, B. K. (2010). "Hybrid molecular structure of the giant protease tripeptidyl peptidase II." **Nat Struct Mol Biol** 17(8): 990-996.

- Peters, J., **Schönegge, A. M.**, Rockel, B. and Baumeister, W. (2011). "Molecular ruler of tripeptidylpeptidase II: mechanistic principle of exopeptidase selectivity." **Biochem Biophys Res Co** 414(1): 209-214.

- **Schönegge, A. M.**, Villa, E., Hegerl, R., Peters, J., Förster, F., Baumeister, W. and Rockel, B. (2012). "The structure of human tripeptidyl peptidase II as determined by a hybrid approach." **Structure** 20(4):593-603.

- Peters, J., **Schönegge, A. M.**, Rockel, B. and Baumeister, W. "Cleavage specificity of Tripeptidylpeptidase II." **in preparation**.

- Peters, J., **Schönegge, A. M.**, Rockel, B. and Baumeister, W. "Potential biological role or irrelevant side activity? A critical assessment of the endopeptidase activity of Tripeptidylpeptidase II." **in preparation**.